Arterial Blood Pressure Estimation Using Ultrasound

by

Aaron Michael Zakrzewski

B.S., University of Rochester (2011)
S.M., Massachusetts Institute of Technology (2013)

Submitted to the Department of Mechanical Engineering
in partial fulfillment of the requirements for the degree of

Doctor of Philosophy in Mechanical Engineering

at the

MASSACHUSETTS INSTITUTE OF TECHNOLOGY

June 2017

Author .... Signature redacted ....
Department of Mechanical Engineering
May 5, 2017

Certified by....... Signature redacted ....
Brian W. Anthony
Principal Research Scientist, Department of Mechanical Engineering
Thesis Supervisor

Accepted by .... Signature redacted
Rohan Abeyaratne
Chairman, Department Committee on Graduate Theses

Arterial Blood Pressure Estimation Using Ultrasound

by

Aaron Michael Zakrzewski

Submitted to the Department of Mechanical Engineering
on May 5, 2017, in partial fulfillment of the
requirements for the degree of
Doctor of Philosophy in Mechanical Engineering

Abstract

While blood pressure is commonly used by doctors as an indicator of patient health, the available techniques to measure the quantity suffer from many inconveniences such as cutting off blood flow, being cumbersome to use, being invasive, or being inaccurate. The research addresses many of these inconveniences by developing and evaluating a novel ultrasound-based blood pressure measurement technique that is non-invasive and non-occlusive.

The technique proceeds in three steps: data acquisition, data reduction, and optimization. In the data acquisition step, an ultrasound probe is placed on a patient's artery and a force sweep is conducted such that the contact force gradually increases; both the applied force and B-Mode images are recorded. In the data-reduction step, the Star-Kalman filter is applied in order to find the size of the artery in each image frame captured. The segmentation data and contact force data are inputs into the optimization step which consists of two sequential optimizations; the first makes many modeling assumptions and gives an estimate of pulse pressure while the second makes less assumptions and uses the approximation of pulse pressure to obtain absolute values of systolic and diastolic blood pressure. Central to the optimization algorithm is a computational biomechanical model of the artery and surrounding tissue, which is numerically modeled using finite elements. The impact of major modeling assumptions is corrected with a one time calibration.

The technique is validated on a number of different data sets. Major data sets discussed include data taken on the carotid artery of (1) 24 single-visit nominally healthy volunteers, (2) two multi-visit nominally healthy volunteers, (3) one multi-visit hypertensive volunteer, and (4) one multi-visit hypotensive volunteer; additional miscellaneous data sets are taken and analyzed as part of this dissertation. The algorithm performance is quantified against readings from an automatic oscillometric cuff. Results show that systolic and diastolic blood pressures can be predicted by the algorithm.

The technology discussed in this dissertation represents a proof-of-concept of a blood pressure measurement technique that could occupy a clinical middle ground between the invasive catheter and cuff-based techniques.

Thesis Supervisor: Brian W. Anthony
Title: Principal Research Scientist, Department of Mechanical Engineering

Acknowledgments

I would like to thank my advisor, Dr. Brian Anthony, for giving me the opportunity to work in such a rewarding lab throughout my time at MIT. His expertise and advise were invaluable for the success of this research and for my professional development. I consider myself immensely lucky to have had the experience of working with Brian.

I would like to thank Dr. Luca Daniel and Dr. Roger Kamm for their extremely helpful advice at committee meetings in order to improve this research. Volunteering to be a part of studies presented in this dissertation was also extremely gracious and helpful of them.

I would like to thank my labmates for their invaluable assistance with this research, for the friendly environment maintained in lab, and for being willing volunteers when needed. In particular, Dr. Matthew Gilbertson for his design expertise, for making the force measurement probe, and for his help with data acquisition; Athena Huang for her design expertise and assistance with data acquisition; Rebecca Zubajlo, Shawn Zhang, and Linda Anthony for volunteering to be part of long-term longitudinal studies presented in this dissertation. Additionally, I'd like to thank Dr. Shih-Yu Sun, Dr. Kai Thomenius, Dr. Dean Ljubicic, Dr. Du Xian, Dr. Bill Vannah, Dr. John Lee, Dr. Aaron Dentinger, Dr. Micha Feign, and Dr. Thomas Heldt. I'd also like to thank Lauren Chai, Jenny Wang, Sisir Koppaka, Nigel Kojimoto, Ina Kundu, Javier Gonzalez, Tylor Hess, Kristi Oki, Bryan Ranger, Megan Roberts, Ian Lee, Anne Pigula, Jon Finke, Alex Benjamin, Rishon Benjamin, Moritz Graule, David Kim, David Mercado, Hank Yang, Siddharth Trehan, Carlos Arguedas, Sissy Liu, Robin Singh, Mingxiu Sun, Melinda Chen, and Judith Beaudoin.

I would like to thank Dr. Anthony Samir, Dr. Manish Dhyani, Dr. Luzeng Chen, Dr. Changtian Li, Dr. Feixiang Xiang, Dr. Yu Duan, and Christiana Crooks for their helpful clinical advice and assistance with data acquisition at Massachusetts General Hospital. I would also acknowledge Samantha Young, Carissa Leal, and Kierstin Wesolowski for making research much easier and more efficient. I would like to thank the funding sources that have supported this research: General Electric

Global Research and the National Institute of Biomedical Imaging and Bioengineering of the National Institutes of Health (award U01EB018813).

Finally, I would like to thank my family - Diane Zakrzewski, Richard Zakrzewski, and Dr. Allyson Zakrzewski - for their unwavering support throughout my time at MIT.

Contents

List of Figures

List of Tables

Chapter 1

Introduction

Blood pressure is an important physiological parameter commonly measured both by medical professionals in a clinical environment [4, 5] and by patients themselves in a home environment [5]. Blood pressure is commonly measured because it gives an indication of the health of a patient. Complications of high blood pressure, also known as hypertension, include stroke, renal failure, peripheral vascular disease, and heart disease, among many other diseases [4–6]. Thus, it is important that there is an easy-to-use and accurate blood pressure measurement technique available.

1.1 Blood Pressure Basics

The heart pumps blood through the arteries to the body's periphery and the blood returns to the heart through the veins. Due to the pumping nature of the heart, the blood pressure in arteries cycles between a maximum, termed systolic blood pressure, and a minimum, termed diastolic blood pressure. A typical healthy patient has a systolic pressure of about 120 mmHg and a diastolic pressure of about 80 mmHg (1 mmHg is equivalent to approximately 133.3 Pa). The fluctuation of pressure in the arteries takes a characteristic shape as shown in Figure 1-1. The difference between systolic pressure and diastolic pressure is termed the pulse pressure. The mean arterial pressure can be found by taking an average over a period of the curve in the figure. An approximate, back-of-the-envelope, formula used to calculate mean arterial pressure is

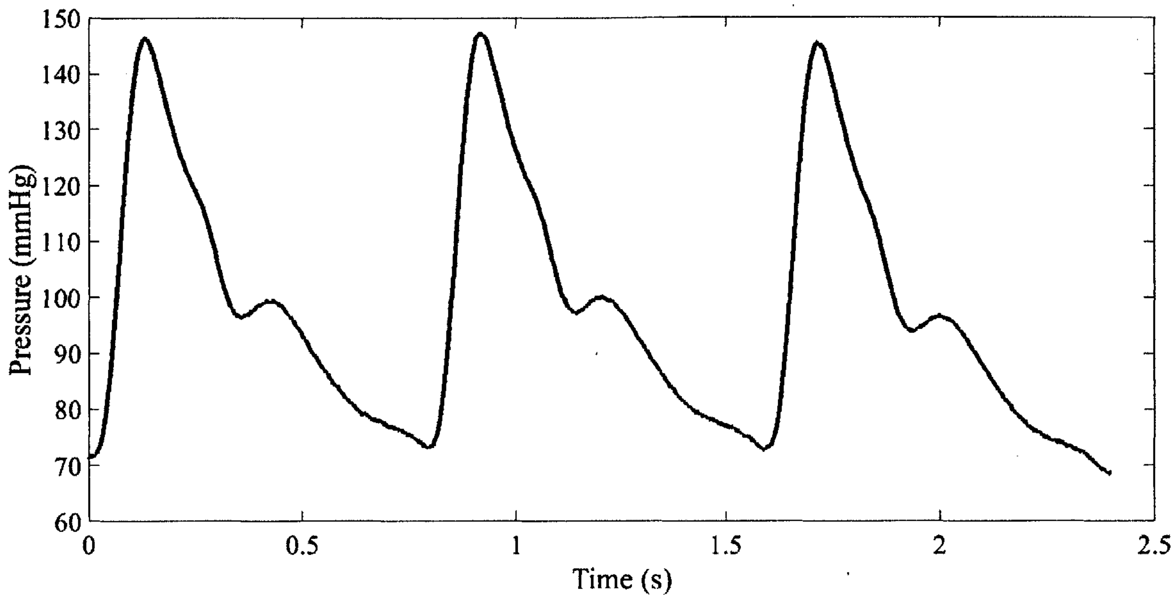

Figure 1-1: Typical blood pressure versus time trace in arteries [1–3]. The maximums are termed systolic pressure and the minimums are termed diastolic pressure.

$$P_{ma} \approx \frac{1}{3}P_s + \frac{2}{3}P_d \qquad (1.1)$$

where P_{ma} is the mean arterial pressure, P_s is the systolic pressure, and P_d is the diastolic pressure. The blood pressure in the aorta is termed 'central blood pressure' [7]. Central blood pressure has been shown to be more closely related to intermediate cardiovascular risks than the blood pressure in the brachial artery [7].

It has been reported that while diastolic and mean arterial pressure are mostly constant throughout the arterial tree, the systolic pressure is often greater in the periphery than in the aorta [8]; this is due to the fact that as the blood moves from the aorta to the periphery, the arteries become stiffer and less elastic [8]. In one study, it was reported that systolic pressure in the radial artery is 112% of the central systolic pressure [9].

Blood pressure can change rapidly, which makes it difficult to validate blood pressure measurement techniques. In one paper, it was reported that blood pressure can change by as much as 20 mmHg over the course of 'a few heart beats' [5, 10].

1.2 Desirable Characteristics of a New Blood Pressure Measurement Device

The desirable characteristics of a new blood pressure measurement device include being usable in a variety of everyday situations, e.g. in-the-home, hospital, and even on-the-go. It would be advantageous if the device would be non-invasive and non-occlusive (i.e. it would not cut off blood flow to any area of the body). Providing accurate and continuous blood pressure readings without any calibration would be beneficial as well.

It would be helpful for the results of the device to be displayed to the user immediately and also recorded for future processing and trend identification. Further, wireless connection to various electronic devices would also be helpful. Finally, it would be great if the data was sharable with an appropriate medical professional whenever needed.

1.3 Blood Pressure Measurement Techniques

There are no existing blood pressure measurement techniques that meet the specifications of the blood pressure measurement device outlined above. Below, the existing blood pressure measurement techniques are described. A summary is included in Table 1.1.

1.3.1 Arterial Catheter

The invasive arterial catheter, inserted most commonly at the radial artery near the wrist, gives a direct blood pressure measurement [11]. While the invasive catheter can be used on most patients, it is not used on patients with Raynaud's phenomenon, thromboangiitis obliterans, infection near the insertion site, or traumatic injury near the insertion site [12]. Since the procedure is invasive, the procedure does have risks, including permanent ischaemic damage (0.09 %), temporary occlusion (19.8%), sepsis (0.13%), local infection (0.72%), pseudoaneurysm (0.09%), haematoma (14.4%), and bleeding (0.53%) [11]. Further risks [11] include abscess, cellulitis, paralysis of the median nerve, suppurative thrombarteritis, air embolism, compartment syndrome, and carpal tunnel syndrome. While the risk percentages of these complications are reported to be very low, the invasive nature of the procedure makes it impractical outside of a hospital. Further, when a catheter is used at the radial artery, it can only measure blood pressure in the periphery, which is different than central blood pressure in the aorta, as discussed in Section 1.1.

1.3.2 Auscultatory Cuff

The blood pressure cuff, also known as a sphygmomanometer, is a common device used for blood pressure estimation [4]. Many different blood pressure measurement methods rely on the cuff. The manual auscultatory method is a cuff-based method used by medical professionals. In the manual auscultatory method, after inflating the cuff and while decreasing cuff pressure, the doctor listens to blood flow sounds using a stethoscope. The doctor makes a judgment on systolic and diastolic pressures using the Korotkoff sounds, defined as the typical sounds blood makes as the cuff decreases in pressure [4]. The first Korotkoff sound occurs when sound is initially audible and corresponds to the systolic pressure; the fifth Korotkoff sound occurs when the blood flow sounds disappear and corresponds approximately to the diastolic pressure [4]. While popular, the blood pressure cuff cuts off blood flow to the arm and thus is not suitable for continuous blood pressure estimation. Further, the auscultatory method requires a trained professional in order to obtain a reading, and thus the method cannot be used in-the-home or on-the-go. Elevated readings are also common due to the white-coat effect [13].

Mercury-based Sphygmomanometer

Mercury-based sphygmomanometers use the auscultatory method described above. However, in this application, a column of mercury is used to indicate the cuff pressure. While this device has, in the past, been labeled the gold standard for non-invasive blood pressure measurement, it has been phased out by the medical community due to the dangers of mercury [4].

The literature has reported that mercury-based auscultatory methods over predict both systolic and diastolic blood pressure compared to invasive catheters [14]. In [14], the systolic pressure correlation was 0.84 and the diastolic pressure correlation was 0.59 compared to invasive catheters. However, in another paper, it was reported that there is no statistically significant difference between mercury auscultatory cuff measurements and invasive arterial line measurements when the patient is at rest [15].

Aneroid Sphygmomanometer

Aneroid sphygmomanometers also use the auscultatory method described above. However, in this application, the cuff pressure is increased by repeatedly squeezing a mechanical 'balloon' and the cuff pressure is displayed on a circular gauge for the doctor to use. Because there are many moving parts, such devices are highly sensitive to poor treatment of the device, e.g. accidentally dropping the device or hitting the device on the side of a table [4].

Devices are reported to vary greatly in accuracy depending on the manufacturer [4]. In one study, it was reported that 44% were inaccurate in a hospital setting [16]. However, in a study of only the Welch Allyn Tycos 767-Series mobile aneroid device (Welch Allyn, Skaneateles Falls, New York, USA), it was reported that there is no statistically significant difference between aneroid and mercury measurements for systolic pressure and only a small statistically significant difference for diastolic pressure [17].

Hybrid Sphygmomanometer

Hybrid sphygomanometers use the auscultatory method and combine the features of the mercury-based devices and the aneroid devices. In particular, the display is often fully digital, allowing for both pressure readings and pulse rate to be displayed.

One study evaluates the validity of the Nissei DM3000 hybrid device (Japan Precision Instruments Inc., Gunma, Japan) and shows that it has the same level of accuracy as the mercury-based sphygmomanometer discussed above [18]. Another study examined the A&D UM-101 device (A&D Company Limited, Tokyo, Japan) and concluded that one version of the device passes the European Society of Hypertension International Protocol for validation of blood pressure measurement devices [19].

1.3.3 Oscillometric Cuff

Automatic blood pressure cuffs are available for use in-the-home or in a hospital setting and use the oscillometric method [4]. In the oscillometric method, the cuff is first placed on the upper arm of the user. After the start button is pressed, the cuff inflates automatically and, as it is deflating, cuff pressure oscillations are sensed [4]. From the envelope of the recorded cuff pressure oscillations, systolic, diastolic, and mean arterial pressure can be approximated using various methods [5]. For example, the maximum amplitude algorithm identifies the cuff pressure at which the envelope reaches a maximum as the mean arterial pressure and identifies systolic and diastolic pressures as the cuff pressure at which the envelope reaches certain fractions of the maximum; many other techniques have been developed, including using derivatives of the envelope or neural networks [5]. Many techniques used in commercial devices to find systolic and diastolic pressures are proprietary [4].

It has been reported that different cuffs give different readings for blood pressure and that mean arterial pressure is typically underestimated by oscillometric blood pressure cuffs [4]. Oscillometric cuffs have been shown to give inaccurate results for children, pregnant women, and patients with atrial fibrillation [20]. Furthermore, the literature recommends that oscillometric measurements are separated by at least one minute and that the average of three readings are taken as the patient's blood pressure [4]. The method occludes the artery and is uncomfortable for patients. Oscillometric cuffs can be obtained at drugstores for between \$15-\$50.

It has been reported that the agreement between oscillometric blood pressure cuffs and invasive pressure measurements is -6.7 ± 9.7 mmHg ($p<.0001$) [21]. In that study, 26.4% of measurements had a discrepancy, compared to the catheter, between 10 mmHg and 20 mmHg while 34.2% had a discrepancy of at least 20 mmHg [21].

Finger Oscillometric Method

The oscillometric method described above for upper arm measurements has been applied to cuffs placed around the finger. However, it has been reported that such devices suffer from significant variability issues and, thus, are not to be used [22].

Wrist Oscillometric Method

The oscilometric method described above has also been extended to apply to the wrist. The advantage of taking blood pressure using a wrist cuff is that wrist size does not vary much in obese patients. One author has reported that wrist cuffs have potential for widespread use [4].

1.3.4 Tonometry

Tonometry, also known as applanation tonometry, is a blood pressure measurement technique originally developed for use at the wrist. In the method, a pressure transducer is placed next to an artery supported by a bone and the transducer readings are assumed to be related to the blood pressure within the artery [4]. Tonometry is a medical term meaning 'to measure pressure' and applanation is a medical term meaning 'to flatten' [23]. Using system models (e.g. transfer functions), tonometry can be used to estimate central blood pressure [24].

The accuracy and precision of tonometry, compared with invasive pressure measurements, has been reported as -5.8 $\pm$ 14.2 mmHg for systolic pressure, 7.2 $\pm$ 8.3 mmHg for diastolic pressure, and 3.9 $\pm$ 8.8 mmHg for mean arterial pressure [25].

One advantage of tonometry is that the entire pressure waveform can be obtained with the technique; however, the method requires calibration with an external device such as a cuff [24]. Tonometry is also very sensitive to placement of the device [26].

1.3.5 Photoplethysmography Methods

A plethysmograph is an instrument used to estimate the volume or volume change of an organ. In photoplethysmography (PPG), the volume of the artery is usually obtained using a device called a pulse oximeter, which is placed on the finger. As blood pulses through the finger, the amount of light transmitted and reflected changes. In pulse oximetry, light transmission or reflection is measured, which is related to the amount of blood in the artery and thus to the volume of the artery. A PPG graph shows the relation between amplitude of the signal in volts versus time. This information has been used in many different ways, with and without calibration, to estimate absolute blood pressure; the literature does not appear to focus significantly on using PPG to measure relative pressure changes. In the following sub-sections, various PPG-based techniques are discussed and the calibration details of each method is described.

Photoplethysmography Alone

A PPG signal alone can be used to estimate relative blood pressure. There are different approaches taken in the literature to obtain blood pressure from only a PPG signal, but all techniques use a calibration step that relates certain features of the PPG reading to blood pressure. The calibration step is needed because the PPG signal itself does not give enough information to find blood pressure; it is not an estimate of blood pressure by itself. The calibration step can be completed using many different approaches. In one approach, the features are extracted directly from a PPG recording taken at the periphery and a regression equation relates the parameters to blood pressure [27, 28]. In another approach, a pulse wave analysis algorithm is used to extract features, then a regression or calibration step is completed to obtain a blood pressure reading [29].

Pulse Transit Time

The pulse transit time has been related to the pressure within an artery. Specifically, the pulse wave velocity, V, is defined for elastic arteries as [30]

$$V = \sqrt{\frac{Et}{2R\rho}} \tag{1.2}$$

where E is the elastic modulus of the artery, t is the artery thickness, R is the inner artery radius, and ρ is the density of the blood.

The literature states that pulse wave velocity can be found as [30]

$$V = \frac{D}{t} \tag{1.3}$$

where D is the distance between the aorta and the location in the periphery where data is collected, and t is the pulse transit time, i.e. the time it takes for a pressure pulse to travel from the aorta to the periphery where data is collected. In order to calculate D, researchers use the height of the patient multiplied by a constant factor. To calculate t, researchers estimate the time between the R-wave of an electrocardiogram (ECG) and the peak of the PPG signal obtained at the periphery [31].

In order to relate pulse wave velocity to the blood pressure, the literature investigates many different models. For example, one author [30] relates the artery elasticity to the pressure using the equation

$$E = E_0 e^{\alpha(P-P_0)} \tag{1.4}$$

where E_0, P_0, and α are parameters to be determined and P is the pressure. Another author [32] derives the equation

$$P = \frac{(0.6h_1)^2\rho}{1.4t^2} + \rho g h_2 \tag{1.5}$$

where g is the acceleration due to gravity, h_1 is the height of the patient, and h_2 is the height difference between acquisition locations.

This method requires access to both an ECG and a time correlated PPG. However, the method has been shown to compare favorably to cuff measurements [32].

Some pulse wave velocity methods require calibration while others are calibration-free [30, 33]. In either case, the unknown parameters in Equation 1.4 need to be considered [33]. In one calibration method, a single oscillometric cuff measurement is used in addition to the known pressure change that occurs when raising the hand (i.e. hydrostatic pressure change) [33]. In a calibration-free method, features of the PPG signal and ECG are used with machine learning of a large database to find the parameters [30].

Finger Cuff

In another PPG-based blood pressure measurement technique, a finger cuff is used to record the PPG signal; this method is alternatively referred to as the vascular unloading technique. As the PPG is recorded, the cuff automatically inflates or deflates in order to keep the blood volume in the finger constant. The pressure required to keep blood volume constant is related to the blood pressure within the vessel [4, 34]. This is called the Penaz method and was first introduced in 1973 [35]; the method was used in the Finapres finger cuff device. While this method has been shown to give accurate estimates of pressure changes, one author suggests that it is not clinically used because of its cost, inconvenience, and high degree of variability when measuring absolute values of pressure [36].

1.3.6 Other Techniques

Other techniques are being developed by research groups to estimate arterial blood pressure non-invasively and potentially continuously using the behavior of ultrasound contrast agents in the blood stream [37–39]. By investigating cavitation frequency, radial oscillations, and general microbubble behavior, blood pressure can be estimated [37]. It has been reported that accuracy might be low with some variations of this technique [37] and it is clear that injection of microbubbles would not be ideal in every circumstance.

In a different technique related to ours, ultrasound and image processing methods are used to measure non-invasively central venous pressure [40]. By tracking the deformation of a superficial vein in the forearm due to an externally applied force, the group estimates the absolute pressure at which the vein will collapse. The collapsing pressure is taken to be the central venous pressure.

Table 1.1: Summary of blood pressure estimation techniques

Method	Description	Advantages	Disadvantages
Auscultatory blood pressure cuff (Hybrid Method)	Doctor listens to Korotkoff sounds [4]	- Comparable to mercury sphygmomanometer [41]	- Terminal digit preference [4] - Inter-observer error [41] - White coat effect if physician takes measurement [4] - Errors occur due to improper rate of deflation [42,43] - Time consuming [41] - Optimal cuff size and placement required [41]
Finger cuffs	Cuff automatically inflates and deflates to keep blood volume constant [34,44]	- Gives accurate estimate of pressure changes [4] - Allows ambulatory measurement over 24 hours [4]	- Under- or over- estimation compared to brachial pressure measurements [4] - Cost, inconvenience, and inaccuracy when measuring absolute pressures [4]
Invasive arterial line	Pressure transducer placed inside artery [11]	- Reliable and accurate; considered gold standard by some [41,45]	- Invasive - Risk of hemorrhage, infection, thrombosis, ischemia, hematoma, accidental injection of intravenous drugs, neuronal or adjacent structure injury [41,45]
Microbubbles	Response of microbubbles to ultrasound [37]	- Non-invasive [46] - Potentially applicable to all chambers of heart [46]	- Requires an injection of microbubbles into blood stream [46] - Requires ultrasound [46] - Some methods reported either low reliability, poor absolute pressure value compared to pressure changes, and low resolution [37]
Oscillometric blood pressure cuff	Automatic cuff processes pressure changes as cuff deflates [47]	- No transducer needed above artery so placement is not critical [4] - Less susceptible to external noise [4] - For ambulatory monitoring, cuff can be removed and replaced by patient [4] - Cheap and ubiquitous [20,41]	- Confounding factors relate to the shape and amplitude of the oscillometric envelope and include artery stiffness [4,20] - Poor accuracy when used on children, pregnant women, and patients with atrial fibrillation [20] - Many algorithms are proprietary [4,20] - Different devices give different readings [4,20] - Do not work well during physical activity [4] - Many devices have not been validated against published standards [20]
Proposed method	Uses finite element analysis to solve the blood pressure inverse problem	- Non-invasive - Non-occlusive - No calibration needed	- Requires ultrasound probe - Requires a 3D printed force measurement attachment
Tonometry	Gauge measures force variation on skin surface [26]	- When used at radial artery, it is a better estimate of central arterial pressure than finger cuffs [41] - Less sensitive than finger cuffs to vasoconstriction and vascular disease [41] - Agreement with arterial line in some (but not all) studies [41]	- Requires calibration for each patient [4] - Not suitable for routine clinical use [4] - Some variations are position dependent [4,41] - Not reliable for elderly patients or for rapid and large changes in blood pressure [41]
Vessel collapse	Computer vision techniques predict point of collapse of superficial vein [48]	- Non-invasive [48] - Easy for non-experts [48] - Automatic readings [48] - Quick, repeatable, and operator-independent [48]	- Technique has only been applied to superficial veins [48] - Requires ultrasound [48]

1.4 Relevant Patents

At least three patents have been awarded which briefly mention the measurement of blood pressure using artery displacements, which are often visualized using ultrasound [49–51]. This is relevant because the method discussed in this dissertation relies on artery deformations to calculate blood pressure. In all of these patents, the absolute blood pressure is obtained using a reference or calibration point provided by the operator, often from a separate device such as a cuff.

In a separate, patented method of non-invasive and potentially continuous blood pressure estimation [52], two blood pressure cuffs are used together; one cuff provides a periodic calibration, and the other cuff provides the change in pressure from the calibration point.

There is also a non-invasive, continuous blood pressure estimation patent that relies on pulse wave velocity methods and that implements an automatic calibration technique [53].

1.5 Accuracy Requirements of New Blood Pressure Measurement Techniques

There are a number of different standards that can be used to validate new blood pressure measurement techniques, with some validation standards specific to sphygmomanometers [4, 54, 55]. It is important to note that, from a regulatory perspective, it is *optional* for manufacturers to meet published validation standards; in fact, there are many oscillometric cuffs on the market that do not meet published standards.

The European Society of Hypertension International Protocol, published in 2010, compares new blood pressure measurement techniques to two mercury auscultatory cuffs [54]. An additional standard, specific to ambulatory monitoring, published by the British Hypertension Society in 1990, also uses the mercury auscultatory cuff as the gold standard [56].

1.6 Clinical Need

Clinically, doctors choose between three non-ideal techniques to measure blood pressure: an invasive arterial catheter, an oscillometric blood pressure cuff, or an auscultatory cuff. Even though the catheter gives continuous and accurate data, inserting the catheter is an invasive procedure. The oscillometric cuff cannot give pressure measurements continuously because it occludes the artery and it has been shown to significantly underestimate mean arterial pressure in patients with atherosclerosis [4]. The auscultatory cuff not only occludes the artery but also requires valuable time from medical professionals. Thus, there is a need for a blood pressure measurement device that serves as an intermediate option between the invasive catheter and cuff techniques. One contribution of the dissertation is a proof-of-concept of a new, intermediate option between catheter and cuff.

1.7 Previous Related Work

In this dissertation, a novel approach using ultrasound is taken to address the clinical arterial blood pressure measurement need described above. Our inspiration to use ultrasound to non-invasively measure arterial blood pressure is quantitative ultrasound elastography, which is a well-known method that uses ultrasound to measure tissue stiffness, i.e. elastic modulus; a review of various elastography methods has been published [57].

The application of elastography methods to blood pressure estimation was first discussed by the author in 2012. Simulated data were used in highly simplified scenarios to estimate pulse pressure [58]. Pulse pressure was included as a variable along with elastic modulus in an elastography inverse problem. The pulse pressure algorithms were confirmed using phantom experiments in [59]. In our paper, we suggested that a new methodology was needed in order to estimate the mean arterial pressure component of the cardiac cycle [60]. This dissertation details a new methodology that accomplishes that goal.

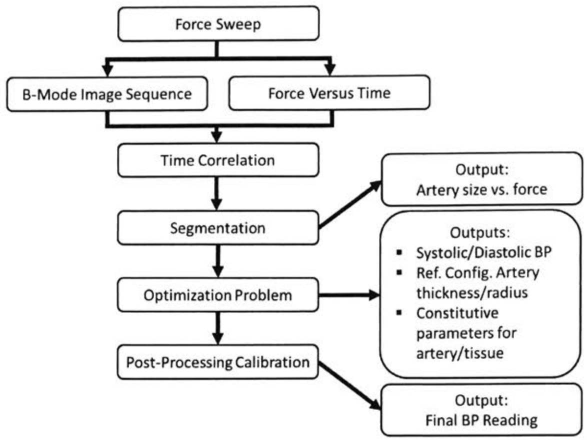

Figure 1-2: The algorithm work flow. After completing the force sweep and the segmentation, the optimization uses both the force data and the segmentation data to solve for pressure.

1.8 Overview of Novel Blood Pressure Measurement Technique

The blood pressure measurement technique developed and tested in this dissertation is summarized in Figure 1-2. The work flow shown in the figure is included here in order to provide context for upcoming chapters. First, the ultrasound probe is placed on tissue above an artery. A force sweep is performed such that the contact force between the probe and tissue gradually increases. During the force sweep, ultrasound images and contact force measurements are recorded. Typical recorded ultrasound images are shown in Figure 1-3 for three different forces. As shown in the figure, increasing the applied force causes a noticeable decrease in artery size. The recorded images and force data are time synchronized and are processed to segment the artery. The segmentation data and force data are used as input into the optimization algorithm, which relies on computational models of the imaged artery and surrounding tissue. After a post-processing calibration step, blood pressure at specific points in the cardiac cycle is output.

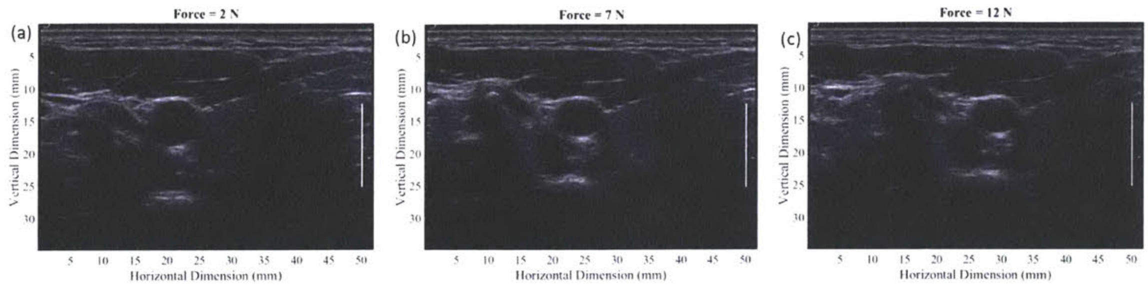

Figure 1-3: Visualization of the compression of the carotid artery during one force sweep in an Internal Review Board (IRB) approved study at Massachusetts General Hospital. It is clear from the images that as the force increases, the artery is compressed, as expected.

1.9 Outline of Thesis

Chapter 2 describes the computational model used in this research, including the geometry and boundary conditions.

Chapter 3 describes the various algorithms that are used throughout the process, including the segmentation algorithm and optimization algorithm.

Chapter 4 describes the general data acquisition procedures. Where applicable, deviations from the general procedure will be discussed in the relevant results chapter.

Chapter 5 describes results on 24 nominally-healthy single-visit volunteers, examines a real-time implementation of the technique, and discusses miscellaneous algorithm metrics, e.g. condition number.

Chapter 6 describes results on nominally-healthy volunteers who have administered the technique on their own artery (termed 'self-scan' in this dissertation). Results include longitudinal studies of two healthy volunteers, the impact of caffeine on blood pressure, and the impact of exercise on blood pressure. The short term (on the order of minutes) variations of the technique's blood pressure readings are also discussed in Chapter 6.

Chapter 7 presents longitudinal results on a medicated hypertensive volunteer, on a hypotensive volunteer, and on older volunteers.

Chapter 8 summarizes the contributions of the thesis and discusses future work to be completed.

1.10 Summary

In this chapter, the existing blood pressure measurement techniques were detailed. The existing literature and patents related to the research were discussed and the accuracy requirements for a new device were outlined. The clinical motivation for this thesis was then presented. Finally, previous related work was summarized, an overview of the method to be discussed was given, and the rest of the thesis was outlined.

Chapter 2

Computational Models

In this chapter, computational numerical models of the carotid artery are developed. The models are used to predict artery deformations due to an applied force, given certain geometric and material parameters. As described in Section 1.8, the model parameters are fit during an iterative optimization algorithm; for details on how the models are applied to the algorithm work flow (Figure 1-2), see Chapter 3.

2.1 Geometry, Loading, and Boundary Conditions

The physical tissue structure and properties are modeled computationally using the finite element method because (1) this method allows for the most flexibility in solving the governing partial differential equations, (2) the commercial availability of fully-featured easy-to-use codes, and (3) it is the standard, accepted solution method for complex solid mechanics problems.

The geometry of the computational model is a semi-infinite slab: it is infinite in the direction out of the page (z) and is long in the horizontal direction (x) compared to the vertical direction (y). In order to reduce computational time, only a thin slice of the slab is modeled with finite elements, as displayed in Figure 2-1. In the orientation displayed in the figure, the probe is pressing on the tissue at the top surface of the domain. Inside the slab, there is an artery with different mechanical properties than the surrounding tissue; the radius of a typical carotid artery is 4 mm and the thickness

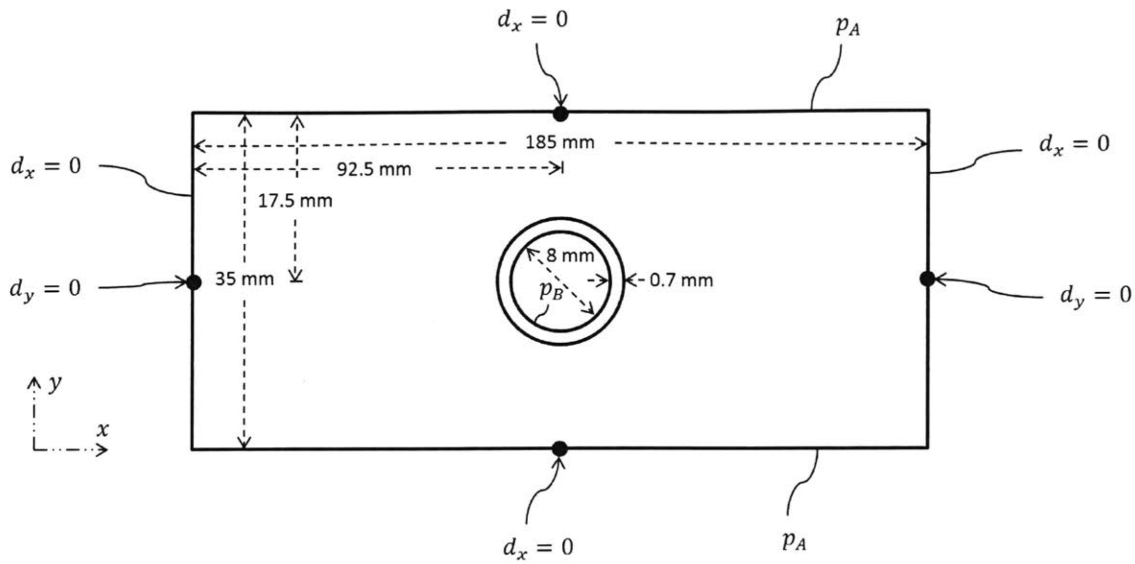

Figure 2-1: Boundary and loading conditions used in the numerical model of the carotid artery. Arrows indicate a boundary condition applied to a specific point while curved lines without arrows indicate a boundary or loading condition applied along an entire surface. In this figure, d is the displacement, p is the pressure, x is in the horizontal direction, and y is in the vertical direction. Not drawn to scale.

of a typical carotid artery is 0.7 mm [61, 62]. We neglect the fluid dynamics of the blood in the vessel; the interaction of the blood with the vessel wall is reduced to a simple pressure at the artery inner surface. The artery and the surrounding tissue are assumed to be in firm contact with each other at the interface.

The domain shown in Figure 2-1 is 185 mm in the horizontal direction and 35 mm in the vertical direction. Positive pressure, p_A, equal to the known applied pressure between the ultrasound probe and tissue, is applied to both the top and bottom surfaces of the domain while the blood pressure, p_B, is applied to the inner wall of the artery. Both the top and bottom surfaces of the domain have an applied pressure due to the symmetry of the problem.

Displacement boundary conditions are applied in order to promote a symmetric deformation due to the symmetric loading and symmetric domain. Specifically, as indicated in Figure 2-1, the left and right vertical surfaces of the domain are fixed in the horizontal direction and allowed to move in the vertical direction. The center points of the left and right vertical surfaces are fixed in both directions. The node in the middle of the bottom surface and the node in the middle of the top surface are constrained in the horizontal direction. Finally, using kinematic coupling constraints, all nodes on the top surface of the domain are constrained to move together in the vertical direction; similarly, all nodes on the bottom surface are constrained to move together in the vertical direction; this condition is included because as the ultrasound probe presses on the tissue, every point on the surface of the tissue along the face of the probe undergoes displacement together in the direction perpendicular to the face of the probe. In order to decrease computational costs even further, the domain could be cut into one quadrant with specific symmetric boundary conditions applied.

Note that we are restricting our analysis to simple finite element models because it has been shown that such models can represent the artery deformations with enough fidelity in order to accurately measure blood pressure. Future work could consist of increasing the complexity of the computational model and, thus, increasing the fidelity of the model; such a change might increase the accuracy of the blood pressure measurement technique. It is feasible that increasing the complexity of the model might broaden the applicability of the method and allow for different diseases to be specifically modeled.

2.2 Constitutive Details

The tissue surrounding the artery is modeled as a linear elastic solid such that the stress, σ, is linearly related to the strain, ϵ, through the elastic modulus, E,

$$\sigma = E\epsilon \tag{2.1}$$

The surrounding tissue is assumed to be homogeneous; this is an significant assumption in the model and is made, as discussed in Section 2.1 above, because it was found that the simple model was sufficient to represent deformations of the carotid artery. Future research could lift this assumption by considering the stiffness of the anatomical features around the artery, including bone and muscle. The Poisson ratio of the tissue is assumed to be 0.495, which is typical for soft tissue [63].

Arteries are reported to be layered and, within each layer, the artery is viscoelastic, hyperelastic, and anisotropic [64]. Assumptions are made about the constitutive law for the artery in order to model it with finite elements. There are two models for the artery that are used in our process; see Chapter 3 for an explanation of how the two artery models are implemented in the optimization procedure.

Model 1 assumes that the artery is homogeneous and linear elastic with an elastic modulus and a Poisson ratio of 0.495; the artery elastic modulus in this model need not be equal to that of the surrounding tissue.

Model 2 assumes that the artery is homogeneous and non-linear. In particular, Model 2 assumes that the elastic modulus is exponentially related to the strain,

$$E = E_0 e^{\alpha\varepsilon}, \tag{2.2}$$

as suggested by [65]. In this equation, ε is the strain, E is the elastic modulus, and E_0 and α are constitutive parameters. It is important to proceed carefully when applying the constitutive equation because we want to avoid an underdetermined optimization problem. In order to apply the constitutive equation, first the finite element program Abaqus (Version 6.8, Dassault Systems, Vélizy-Villacoublay, France) is used to fit the exponential relationship to a second order polynomial model for use in Abaqus. A parameter serves as an index into a set of those second-order polynomial models; it is this parameter that is included in the optimization discussed in Chapter 3. The strain energy is found automatically by Abaqus. The fitting allows for a single parameterization of the artery; this parameterization is critical to a stable optimization procedure, which is described in Chapter 3. Different hyperelastic constitutive laws for the artery and their impact on the results of the algorithm could be considered in future research.

2.3 Mesh Generation

A mesh is automatically generated using the following procedure, as shown in Figure 2-2. First, the node locations and element connections are calculated on a uniform rectilinear grid, as shown in Figure 2-2a. Second, as in Figure 2-2b, elements where the artery and lumen are located are removed from the mesh. Third, as in Figure 2-2c, nodes of elements adjacent to the artery are projected, along a radial line emanating from the lumen center, onto the appropriate location on the outer edge of the artery. Fourth, as in Figure 2-2d, a layer of elements representing the artery are added with associated nodes. Fifth, as in Figure 2-2e-f, the domain is extended in the horizontal direction in order to ensure that the boundaries do not impact displacements of the artery. Relevant mesh parameters are the initial artery radius and the artery thickness, both of which change as a variable in the minimization problem.

2.4 Additional Finite Element Details

A mixed, displacement-pressure finite element formulation is used such that each element has a constant pressure [66]. The formulation uses four-displacement-node quadrilateral elements with one pressure node. Further, large deformations are assumed for all models in this thesis. Plane strain is also assumed; the plane strain assumption, which has been used in the literature to model the deformation of an artery's cross-section [65,67], is accurate because deformations due to an expanding artery are in the plane and the artery can be thought of as long, length-wise, compared to other in-plane dimensions. As part of the plane strain assumption, it is assumed that the out-of-plane strain is zero. This finite element model was run using Abaqus, which is called automatically from Matlab (Version R2015a, MathWorks, Natick, Massachusetts, USA) in order to eliminate user interactions.

In Figure 2-3, sample finite element results for Artery Model 1 described above are shown. The domain is shown in Figure 2-3a, a typical stress field is shown in Figure 2-3b, and the stress field in the vicinity of the vessel is shown in Figure 2-3c.

Similar results for Artery Model 2 are shown in Figure 2-4. Note, in particular, that the deformations in Model 1 are due to the pressure applied within the vessel only (i.e. $p_A = 0, p_B \neq 0$) while the deformations in Model 2 are due to both the pressure applied within the vessel and pressure applied on the top and bottom surfaces of the domain (i.e. $p_A \neq 0, p_B \neq 0$). These differences are explained in Chapter 3.

2.5 Summary of Major Assumptions in the Computational Model

In this section, the major model assumptions are discussed.

The major assumptions are (1) the constitutive equation for the artery is assumed to be linear elastic in Model 1 and nonlinear in Model 2, (2) the tissue surrounding the artery is assumed to be homogeneous and linear elastic, and (3) the applied force on the skin is assumed to be the average force over the face of the probe, which is important considering that the skin surface at the carotid artery is likely curved. Other assumptions include (1) that the artery can be modeled as a homogeneous material, (2) that the plane strain formulation can be used, and (3) that the materials are incompressible.

2.6 Model Variation: Bone Inclusion

In order to address the second major assumption in Section 2.5, bone is optionally included in the computational model. In this version of the computational model, the bone is assumed to extend uniformly throughout the entire bottom of the domain as displayed in Figure 2-5. Furthermore, the boundary conditions and loading conditions do not change in this variation of the typical computational model discussed above. The bone is described by a linear elastic constitutive equation with a known stiffness. A typical bone stiffness is 17 GPa [68]. By including the bone in the computational model, the model becomes more representative of the human body.

2.7 Summary

In this chapter, the computational models for the carotid artery were discussed in detail. In particular, the geometry was defined, the boundary and loading conditions were specified, and the constitutive laws were discussed. The implementation in Abaqus was introduced, typical stress results were displayed, and the major assumptions in the computational models were listed. Finally, a variation to the default computational model was introduced such that the bone is included in the model.

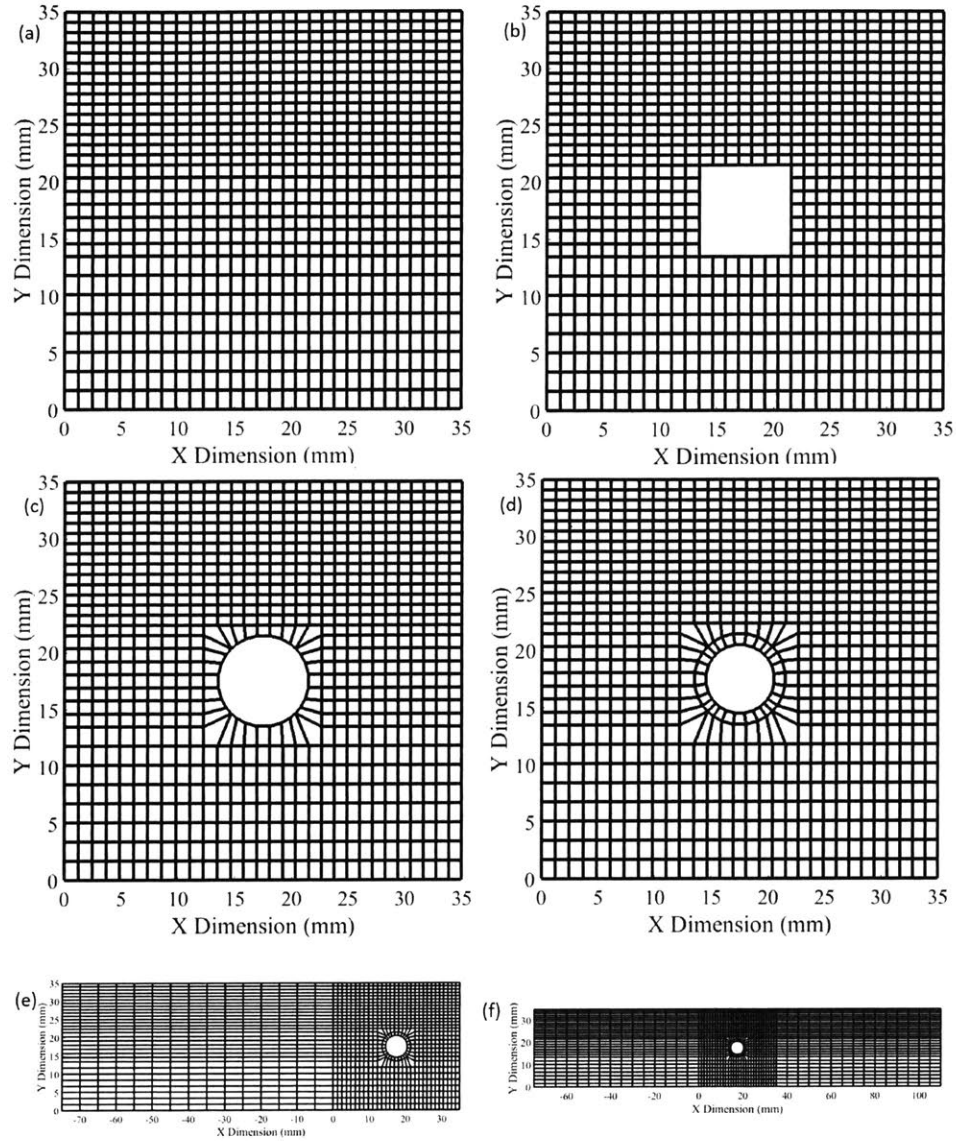

Figure 2-2: Mesh generation process used to discretize each computational model of the carotid artery. In (a), a uniform grid is generated; in (b), the elements overlapping with the artery and lumen are removed; in (c), the nodes on the inner surface are projected on the surface of the outer wall of the artery; in (d), the artery elements are added to the model; in (e) and (f), the domain is extended to fill the dimensions described in Figure 2-1.

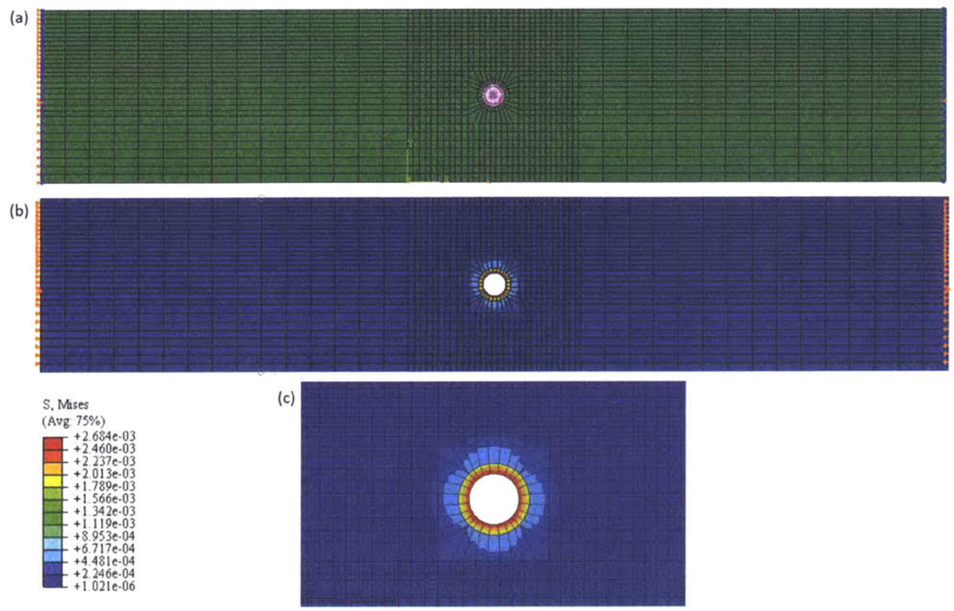

Figure 2-3: Screen captures of the Abaqus model used for Model 1. In (a), the geometry is displayed. In (b), a typical stress distribution is shown where the model is in the deformed configuration. In (c), a close up of the stress distribution near the vessel is shown. The stress units are MPa.

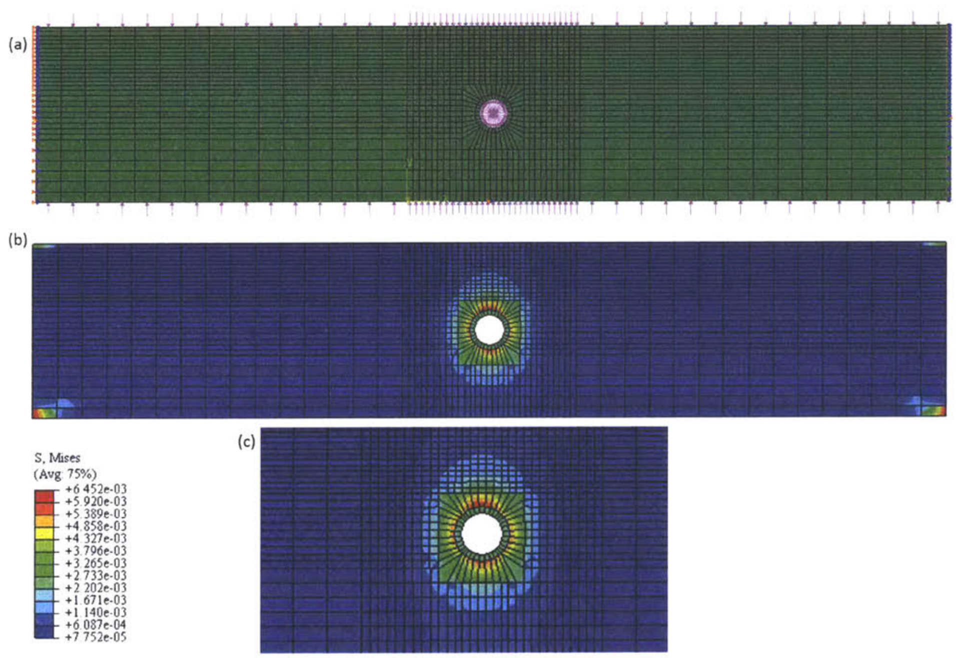

Figure 2-4: Screen captures of the Abaqus model used for Model 2. In (a), the geometry is displayed. In (b), a typical stress distribution is shown where the model is in the deformed configuration. In (c), a close up of the stress distribution near the vessel is shown. The stress units are MPa.

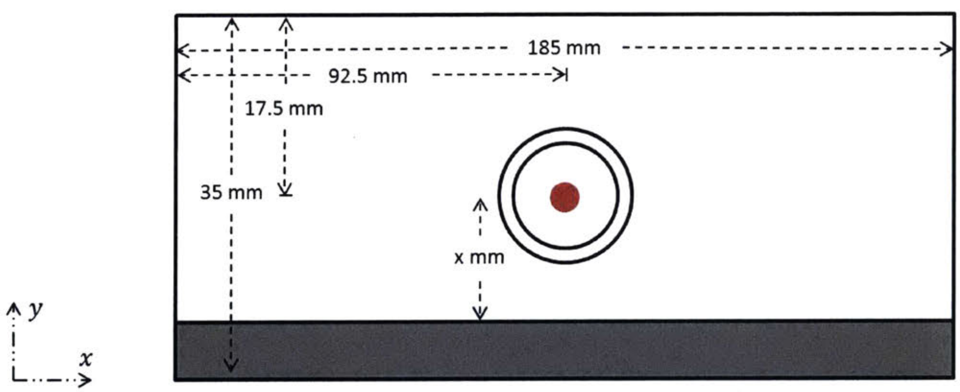

Figure 2-5: When the bone is added in the computational model, it is extended throughout the entire bottom of the computational domain.

Chapter 3

Computational Methods

This chapter describes the computational methods that are used throughout the arterial blood pressure measurement technique; for a high level overview of the technique, see Section 1.8 and Figure 1-2. The algorithms discussed in this chapter include the three-tap synchronization method, segmentation procedures, optimization procedures that solve for blood pressure, post-processing k-fold cross validation calibration details, and a real-time implementation of the optimization procedures.

3.1 Three Tap Synchronization Method

While both applied contact force and ultrasound data are recorded during data acquisition, the two data sets are currently acquired on different machines: the force data is collected on a laptop while the ultrasound images are collected on a clinical ultrasound system. Because the data streams are acquired on two different machines, the independent time axes are not inherently synchronized. It is important to synchronize the two data sets such that each ultrasound video frame is assigned a correct force. If hardware clock signals to the ultrasound machine were available, syncing the data at acquisition would be trivial.

To sync the data, a three tap synchronization method was developed in collaboration with Athena Huang [69]. In this method, the sonographer is instructed to complete three taps on the patient's carotid artery during the force sweep. The three taps will appear as spikes in the force data and as motion-induced changes in the ultrasound images. The three taps are found in the ultrasound data by manually identifying motion-induced changes in the ultrasound video; the changes are recorded as frame numbers. The three taps in the force data are found semi-automatically by first manually bounding the portion of the sweep containing the taps (using two user clicks in Matlab) and then automatically finding the peaks in the selected range; the peaks are recorded as data indices.

Once the three maximums of the force data are found (as a vector y of data indices) and the three taps in the ultrasound data are found (as a vector x of frame numbers), the synchronization method can proceed. In the discussion to follow, it is assumed that the time relationship between the ultrasound machine and laptop is constant and does not vary over time.

A linear fit of x versus y is completed in order to find a slope and y-intercept that allows each frame to be assigned a non-integer force data number. By interpolating this data onto the array consisting of data number and force value, one obtains a force value at each frame of the ultrasound video. Figure 3-1 shows a typical force sweep as a function of time, the same force sweep as a function of data number, and the final time synchronized sweep. This information is used during processing of data before inputting into the optimization algorithm.

3.2 Artery Segmentation Algorithm

A segmentation algorithm is employed in order to obtain artery diameter from the captured ultrasound B-Mode data. In particular, the size of the artery versus force is to be calculated at systole and diastole.

Many algorithms have been investigated to accomplish artery segmentation on ultrasound images taken through the cross-section of the artery [70–75]. Active contour and snake methods are sometimes used, often with good results reported in the literature [70]. However, these algorithms easily suffer from noise and require careful optimization of the relevant parameters [70]. A template matching algorithm

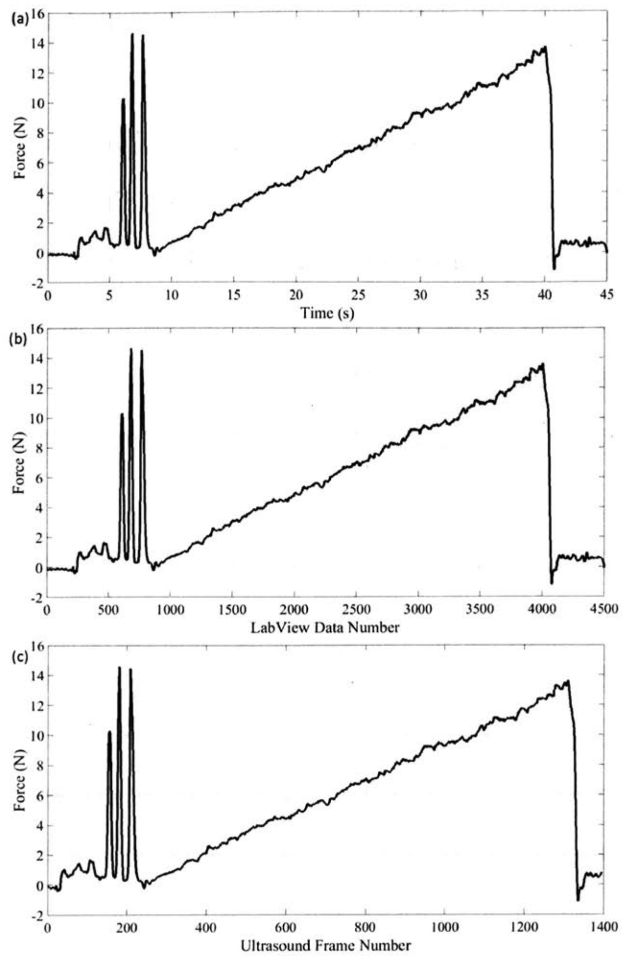

Figure 3-1: The plots demonstrate the correlation of the force sweep with the ultrasound data. In (a), the force sweep is displayed as a function of time. In (b), the force sweep is displayed as a function of LabView data number. In (c), the force sweep is displayed, after synchronization with the ultrasound video, as a function of ultrasound frame number.

can be used, but such a process requires significant computational cost [70]. Modified balloon models and hough transforms have also been used in the literature [70, 71].

The segmentation algorithm chosen for the novel blood pressure measurement technique is the Star-Kalman algorithm as described in [70, 72, 73] and customized for the ultrasound systems used to record data for this dissertation. The algorithm has been reported to be robust to noise and allows for non-circular artery segmentation, which is important when looking at the deformation of an artery under compressive external loads.

For details of the Star-Kalman segmentation algorithm, readers are referred to

[70, 72, 73]. A brief description of the algorithm as discussed in those publications is included below.

A seed point is first identified near the middle of the vessel. For the first frame of the ultrasound sequence, this seed point is obtained through a user click near the center of the artery. For all subsequent frames of the sequence, the seed point is taken as the center of mass of the previous frame's vessel segmentation; this assumes that the frame-to-frame movement of the artery is small. Before proceeding with the segmentation, a 10 pixel by 10 pixel median smoothing filter [76] is applied to the image.

After the seed point is identified and the median filter applied to the image, 100 equiangular radial lines are extended from the seed point; a sample of 6 of these radial lines are shown as the red lines in Figure 3-2. Each radial line is sampled at 0.05 mm intervals (which approximately corresponds to one pixel in the image) and the corresponding pixel values are recorded. Each line undergoes a 1D 5-pixel median filter and is then input into an edge function. The edge function, F_{edge}, as suggested in [77], is defined as

$$F_{edge}(r_k^p) = \frac{1}{3}\Big(x(r_k^p+2)+x(r_k^p+1)+x(r_k^p)-x(r_k^p-1)-x(r_k^p-2)-x(r_k^p-3)\Big) \quad (3.1)$$

where the edge function is calculated at each point along each of the radial lines. Here, r_k^p is the r^{th} pixel along the k^{th} radial line, $x(r_k^p)$ represents the grey-scale value of the r^{th} pixel along the k^{th} radial line, and the superscript p indicates that pixel numbers are being discussed. Negative values of the edge function are set to zero; this helps in the edge detection because the interior of the artery is known to appear black (zeros on a grey-scale color map) while the artery and surrounding tissue is known to appear whiter (ones on a grey-scale color map).

A total of 20 iterations are completed at each frame, where one iteration consists of angularly traversing the vessel once and running through the following equations on each radial line passed.

Kalman filter details can be found in [78]. The system for the segmentation

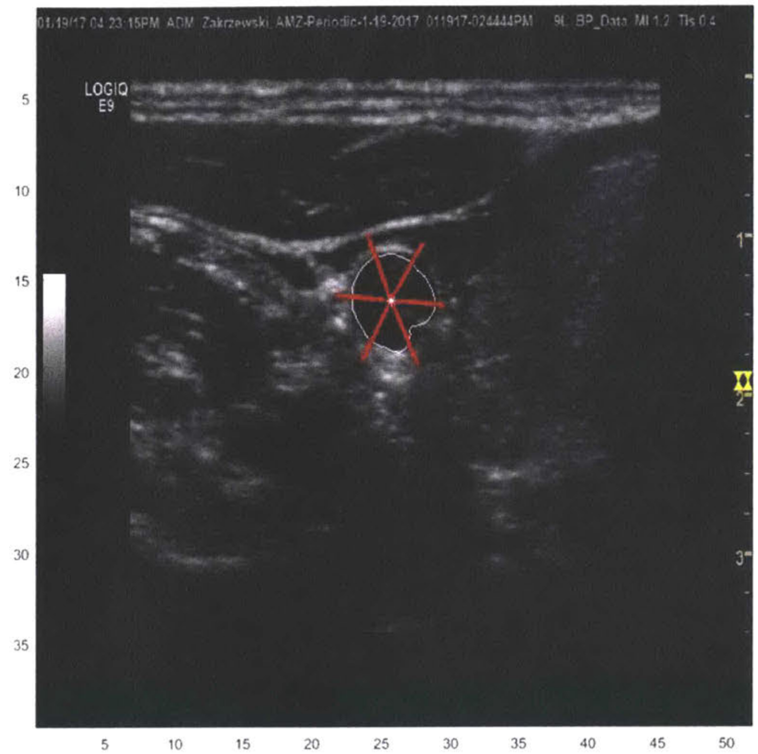

Figure 3-2: The image shows the details of the segmentation algorithm. The red lines are a sample of the 100 equiangular radial lines used in the Star-Kalman algorithm. The white contour represents the contour estimated by the algorithm for this particular frame. The white star is the center of mass of the contour.

discussed in this section is described as

$$x_{k+1} = x_k + \zeta_k$$
$$r_k = C(x_k) + \eta_k$$

where

$$C(x_k) = \frac{a_k b_k}{\sqrt{b_k^2 \cos^2(\theta_k - \phi_k) + a_k^2 \sin^2(\theta_k - \phi_k)}} \tag{3.2}$$

In these equations, x_k is the state defined by $x_k = [a_k, b_k, \phi_k]$, a_k is the semi-major axis of the ellipse, b_k is the semi-minor axis of the ellipse, ϕ_k is the angle of tilt of the ellipse, θ_k is the angle corresponding to the k^{th} radial line, r_k is the radius length along the radial line in question, and η_k and ζ_k are white, zero-mean, Gaussian noise with covariances Q and R, respectively.

First, the Jacobian of C is numerically calculated as

$$H_k = [\nabla_x C(x)^T]^T \Big|_{x=x_{k|k-1}} \tag{3.3}$$

Note that $x_{k|k}$ is an estimate of the state x_k and that $x_{k|k-1} = x_{k-1|k-1}$. After the Jacobian is numerically calculated, the algorithm proceeds to calculate the state prediction covariance, $P_{k|k-1}$, as

$$P_{k|k-1} = P_{k-1|k-1} + Q \tag{3.4}$$

In this formulation, the state prediction covariance is technically an approximate mean squared error [78]. Next, the measurement prediction covariance, S_k, is found as

$$S_k = H_k P_{k|k-1} H_k^T + R \tag{3.5}$$

This measurement prediction covariance is an indication of the uncertainty of the measurement prediction. The Kalman gain, G_k, controls the weight given to measurements and estimates when finding an estimate of the predicted state. The Kalman gain is found using

$$G_k = P_{k|k-1} H_k^T S_k^{-1} \tag{3.6}$$

The estimate of the state can then be found as

$$x_{k|k} = x_{k|k-1} + G_k(r_k - C(x_{k|k-1})) \tag{3.7}$$

The estimated edge is then

$$r_k = C(x_{k|k}) \tag{3.8}$$

Finally, in order to be used in the next step, the state prediction covariance is calculated as

$$P_{k|k} = P_{k|k-1} - G_k S_k G_k^T \tag{3.9}$$

In order to evaluate these equations, the residual in Equation 3.7 must be approximated.

To find the residual, the r_k value is chosen based on the equations from [72],

$$r_k = \sum_{i=1}^{M} r_k^i \beta_i \tag{3.10}$$

where M is the number of candidate points and

$$\beta_i = \frac{p_i(k)}{\sum_i p_i(k)} \tag{3.11}$$

In this equation, p_i is taken to be the square of the edge function in Equation 3.1; note that this choice of p_i is slightly different than specified in [72].

In order to run this segmentation algorithm, initial parameter values must be set. The initial state was taken to be

$$x_{0|0} = \left[\frac{r_{max}}{2}, \frac{r_{max}}{2}, 0\right] \tag{3.12}$$

as suggested by [70]. In this equation, r_{max} was chosen to be 4 mm for the first frame of the force sweep and, for all other frames, equal to 1.5 times the semi-minor axis calculated from the previous frame. As suggested in [70], R is chosen to be 20, and

$$Q = \begin{bmatrix} 2 & 0 & 0 \\ 0 & 2 & 0 \\ 0 & 0 & 0.1 \end{bmatrix} \tag{3.13}$$

Further, M is chosen to be 10, which is chosen as it appears to give better results than the value of 5 suggested by [70].

After all iterations are completed for a particular frame, the vertical or minor radius of the contour result is recorded for further processing.

After applying the segmentation algorithm to the force sweep, the relationship between artery minor radius and force is known, as shown by the black line in Figure 3-3. From this knowledge, the artery vertical axis at systole and diastole versus force is found by finding the peaks and valleys of the black line. A linear fit to this data

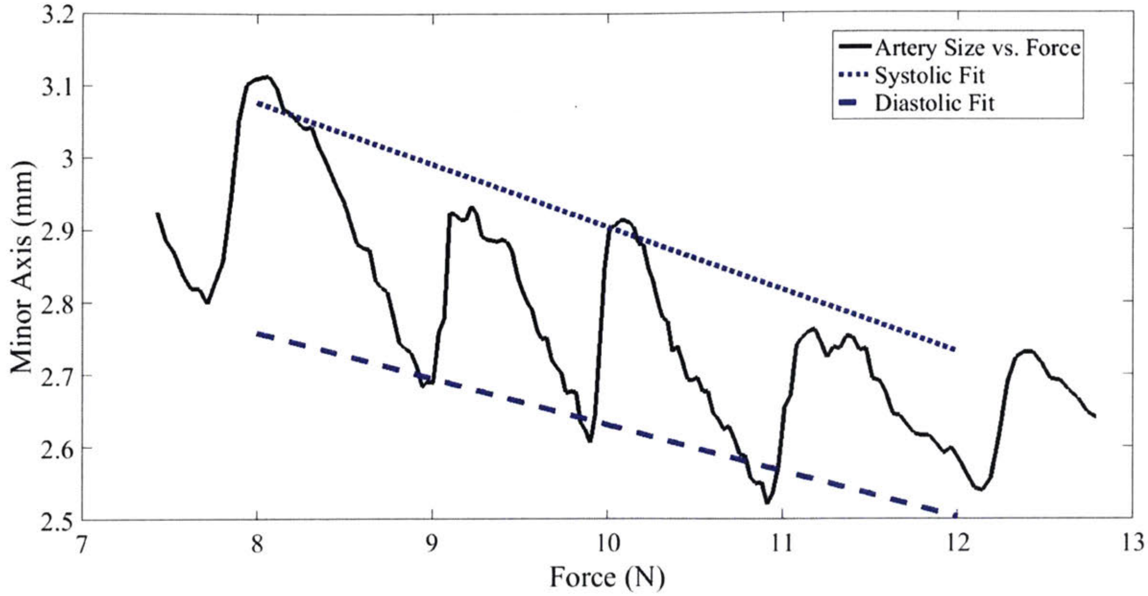

Figure 3-3: Segmentation results. The black line shows the size of the artery versus force over many cardiac cycles. The dotted blue line shows a fit to the peaks and represents the size of the artery at systole versus force. The dashed blue line shows a fit to the valleys and represents the size of the artery at diastole versus force.

is shown in the dashed and dotted blue lines in the figure. These fit lines represent the size of the artery at diastole and systole, respectively. The blue lines, specifically between the forces of 8 N and 12 N, are used as input into the optimization algorithm, which is described in the next section.

3.3 Optimization Procedures

In order to use the computational model and segmentation results to obtain blood pressure, an optimization problem is formulated. In particular, the optimization is an inverse problem because displacements are sensed and the pressure required to achieve those displacements is sought. To solve the inverse problem two successive optimizations are completed, as visualized in Figure 3-4. The first optimization solves for an estimate of pulse pressure and utilizes Artery Computational Model 1; the second utilizes Artery Computational Model 2 and solves for absolute values of systolic and diastolic blood pressures.

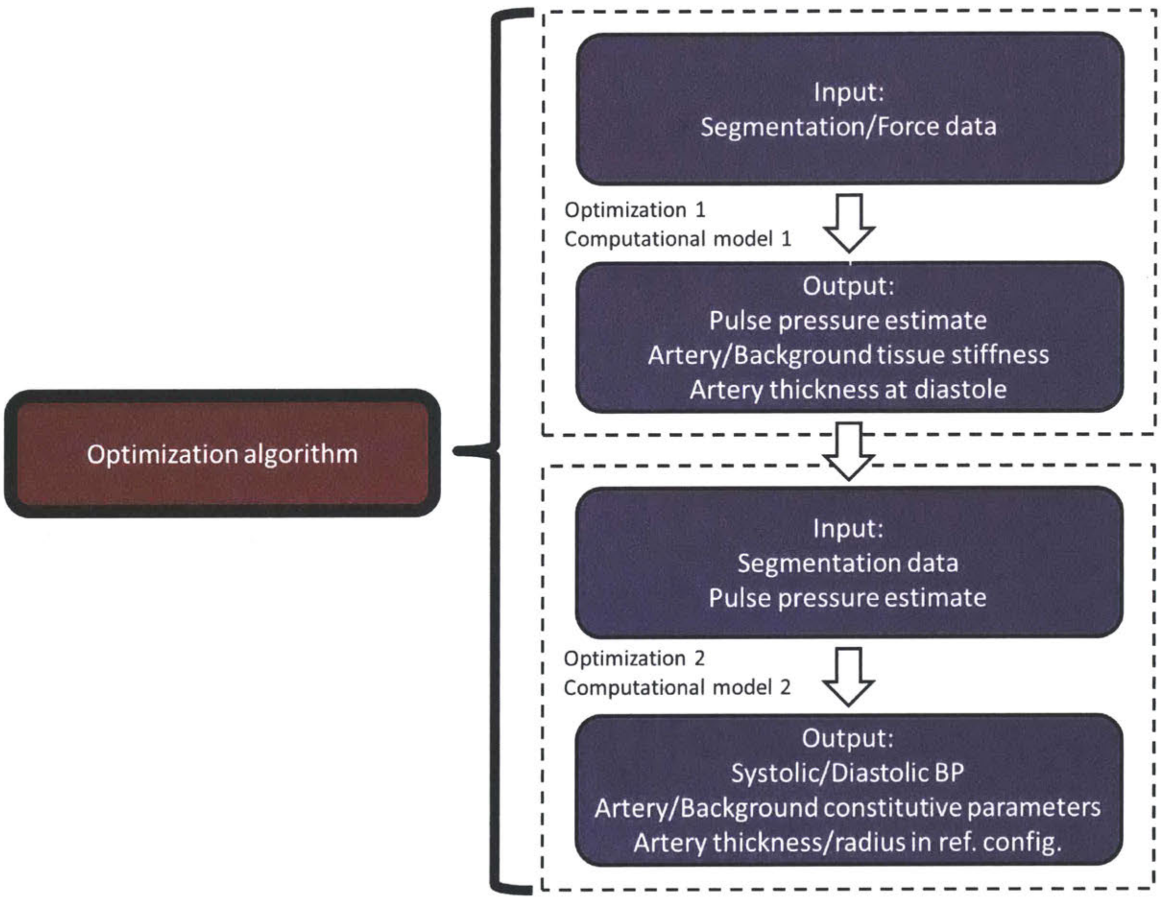

Figure 3-4: Visualization of the split of the optimization problem into two successive optimizations.

3.3.1 First Optimization Formulation

The first optimization uses the objective function

$$(x_1^d - x_1^c)^T(x_1^d - x_1^c) \tag{3.14}$$

and the parameters to be optimized over are

$$(E_1, a_1, t_1, P_1^o) \tag{3.15}$$

In this formulation, E_1 is the elastic modulus of the linear elastic background tissue, a_1 is the elastic modulus of the linear elastic artery, t_1 is the thickness of the artery at diastole at the lowest applied force, P_1^o is the pulse pressure with the subscript referring to the fact that it is estimated in the first optimization, x_1^d is the B-Mode segmentation data, i.e. artery minor axis at systole versus applied force, and x_1^c is the analogous finite element analysis artery dimensions.

The purpose of the first optimization is to analyze a simple model in which the artery is assumed to be linear elastic, the deformations occur only within the physiological pressure range (beginning at diastolic pressure and ending at systolic pressure), and the pulse pressure is the most important parameter to be estimated. The computational model, including geometry and boundary conditions, was described as Model 1 in Chapter 2. In this optimization, the absolute pressure is not estimated.

In order to evaluate the objective function in Equation 3.14, the parameters in Equation 3.15 must first be fixed and a vector, $\hat{f}$, of contact forces must be specified (e.g. such a vector is typically [8, 9, 10, 11, 12] N). The finite element model, g, described in Chapter 2, is then run with the fixed parameter set at each contact force in $\hat{f}$; from the deformed finite element models, the artery minor axis is found and recorded at each contact force in $\hat{f}$. This can be described using the notation, ${}_ix_1^c = g(\hat{f}_i, E_1, a_1, t_1, P_1^o)$. After evaluating g at each $\hat{f}_i$, the vector x_1^c is ready to be input into Equation 3.14. Next, x_1^d is found by evaluating the dotted blue line in Figure 3-3 at each contact force in $\hat{f}$; using notation, ${}_ix_1^d = h(\hat{f}_i)$, where h is the function evaluation. After evaluating h at each $\hat{f}_i$, the vector x_1^d is ready for use in Equation 3.14. Finally, the two vectors are plugged into Equation 3.14 for evaluation of the objective function.

After solving for an estimate of pulse pressure under simplified conditions, a second optimization then solves a more complex model for absolute pressure estimates.

3.3.2 Second Optimization Formulation

The second optimization uses the objective function

$$(x_2^d - x_2^c)^T (x_2^d - x_2^c) + k(P_1^o - P_2^o)^2 \tag{3.16}$$

and the parameters to be optimized over are

$$(E_2, a_2, t_2, r_2, p_2^d, p_2^s) \tag{3.17}$$

In this formulation, E_2 is the elastic modulus of the linear elastic background tissue, a_2 is an index into a set of non-linear artery elasticity functions, t_2 is the thickness of the artery in the unloaded zero-pressure state, r_2 is the radius of the artery in the unloaded zero-pressure state, P_1^o is the pulse pressure estimated from the first optimization, P_2^o is the pulse pressure estimated from the current iteration of the current optimization, and k is a scaling parameter. In Equation 3.17, p_2^d and p_2^s are diastolic and systolic pressures, respectively. In Equation 3.16, x_2^d is the B-Mode segmentation data, i.e. artery minor axis at systole *and* diastole versus applied force, and x_2^c is the analogous finite element analysis artery dimensions.

In the finite element model used for this optimization, the artery is assumed to be non-linear, as described in Model 2 of Chapter 2. Further, the deformations begin with the non-physiological (i.e. not realized on people) zero-pressure geometry and end at either diastolic or systolic pressure.

Solving for the zero-pressure state (r_2, t_2) in the second optimization is important to the overall accuracy of the algorithm. The role of the zero-pressure state can be best understood using commonly accepted circuit equivalents. Pressure in the artery is 'equivalent' to voltage in a circuit. In order to obtain a known, absolute voltage across a resistor, a ground in the system must be either known or approximated. Similarly, in order to obtain a known, absolute pressure in the artery, a ground state must be either known or approximated. This ground state is the undeformed geometry of the vessel. Restated in another way, this is the non-physical scenario where blood pressure inside the vessel is exactly zero. Since this scenario is unknown and patient-dependent, it is estimated by the algorithm. Some groups have examined the estimation of this zero-pressure state, but they have only done so with a known blood pressure [79, 80].

3.3.3 Solving Optimization Problems

For a perfect fit, the objective functions in Equations 3.14 and 3.16 would be zero. However, due to model assumptions and data inaccuracies, the objective functions will not be zero. In order to find the optimal parameter set that minimizes the functions, the iterative Levenberg-Marquardt [81] solution method is used. In each iteration of this method, a new parameter set, x_{new}, is calculated using the equations

$$x_{new} = x - \Delta g \tag{3.18}$$

and

$$\Delta g = (J^T J + \mu I)^{-1} J^T (x_e^d - x_e^c), \tag{3.19}$$

where J is the Jacobian matrix, μ is the Marquardt damping parameter, I is the identity matrix, and e indicates the optimization number being solved. In Equation 3.18, x is a vector of the estimated parameter set from the last iteration and Δg is the calculated step needed to get to the next estimate of the parameter set.

The Jacobian matrix is calculated using a finite difference formula where the step size for each parameter is 10% of the current parameter value. That is,

$$J_{ij} = \frac{\partial f_i}{\partial x_j} = \frac{f_i(x) - f_i(x^*)}{0.1 x_j} \tag{3.20}$$

$$x_i^* = x_i - 0.1 x_j \delta_{ij} \tag{3.21}$$

where x is the current parameter list, δ_{ij} is the Kronecker Delta (zero when $i \neq j$ and one when $i = j$), and subscripts on the vectors x and f refer to the entry in the vector. In this equation, f is a vector-valued finite element function that takes the parameter set and outputs the objective function value at each specified point in the force range. In Equation 3.20, the rows of the Jacobian correspond to changes in different elements of f; columns of the Jacobian correspond to slightly varying the different input parameters. Note that in Equation 3.21, Einstein summation is *not* to be used.

In the optimization process, a maximum size of Δg is enforced in order to promote favorable convergence properties. After calculating the new parameter set, x_{new}, the parameter μ is varied in order to increase the rate of convergence. The initial value of μ is 0.01; this initial value has been shown to be unimportant to the performance of the optimization procedure [82]. After the initial value is set, the iteration proceeds using two different avenues [83]. If the objective function decreases at this value of μ, then μ is decreased by factors of two (thereby decreasing damping) until further decreasing of μ does not further decrease the objective function value or until 30 decreases have been calculated; the value of 30 is chosen as a reasonable value that has been shown to yield good results for this optimization. If the objective function increases at a μ of 0.01, then μ is increased by factors of 2 (thereby increasing damping) until the objective function decreases or until 100 increases have been calculated; while the value of 100 is chosen because it has been shown to give good results for this optimization, it could be reduced, for example to 30, in order to greatly speed up the optimization process.

The first optimization is initialized using the parameters specified in Table 3.1 and the second optimization is initialized using the parameters specified in Table 3.2. The initialization parameters were chosen to be fixed for all runs of the optimization in order to effectively compare the results of the optimization; if these initialization parameters were not fixed, it would be tough to estimate the average number of iterations needed to complete the algorithm. The constitutive parameters displayed in these tables are chosen to be close to average results predicted by the algorithm. The thickness and radius values are chosen to be representative of a typical artery. The pulse pressure in the first table is chosen to be less than the likely value (40 mmHg) in order to not bias the algorithm by starting at the likely optimal value; starting at 40 mmHg would make it tough to determine if the algorithm was performing correctly. The systolic and diastolic pressure in the second table is also chosen to be offset from the expected, likely values (120 mmHg and 80 mmHg, respectively), in order to assist with a determination of algorithm performance.

Table 3.1: The initial parameter values for the first optimization.

Parameter	Value
E_1	150 kPa
a_1	300 kPa
t_1	1 mm
P_o^1	10 mmHg

Table 3.2: The initial parameter values for the second optimization.

Parameter	Value
E_2	200 kPa
a_2	Index: 15
t_2	1 mm
r_2	2.85 mm
p_1	95 mmHg
p_2	105 mmHg

The optimization is stopped when the objective function value obtained from the new parameter set is not smaller than the objective function value obtained from the previous parameter set. Typically, optimizations in this dissertation use less than 10 iterations to converge; for this reason, there is no stopping criteria regarding maximum iteration number possible.

3.4 Post-Processing Calibration Step

The three most significant assumptions in the computational model described in Chapter 2 are that (1) the artery can be modeled as linear elastic in Model 1 and nonlinear in Model 2, (2) the surrounding tissue can be modeled as a homogeneous, semi-infinite slab, and (3) the applied force can be modeled as an average force. After the optimization is completed, a data-driven calibration procedure is applied in order to partially correct for the biases introduced by the assumptions of the computational model. This can be thought of as a post-processing calibration step. The magnitude of the calibration factor is different for systolic and diastolic pressures because the impact of the assumptions change depending on the absolute value of blood pressure.

3.4.1 K-Fold Cross Validation

The magnitude of the calibration factor is obtained through the k-fold cross-validation method [84]. The k-fold cross-validation process is shown visually in Figure 3-5 and, on a high level, amounts to a learning or training algorithm. After removing outliers, the data set is randomly split into a training set and a final test set, representing 2/3 and 1/3 of the entire set, respectively. During one iteration, the training set is randomly split into K folds; the first $(K-1)$ folds are used to find the fitting parameters and the Kth fold is used to calculate the error. The fitting parameters take the form of the parameters describing a line, with slope m and intercept b. To find the parameters, a line is fitted between two data sets: (1) a vector of training set algorithm measurements, and (2) a vector of corresponding cuff measurements minus corresponding algorithm measurements. This fitting is performed once for the diastolic results and once for the systolic results.

A total of 1000 k-fold cross-validation iterations are completed on the training set and the parameter set corresponding to the iteration with the minimum error is chosen. Finally, the parameter set is applied to the final test set in order to report the relevant statistics.

3.5 Real-Time Approach To Optimization

While blood pressure is an important quantity to doctors, they are not willing to wait a long time for a blood pressure measurement. A typical optimization as described

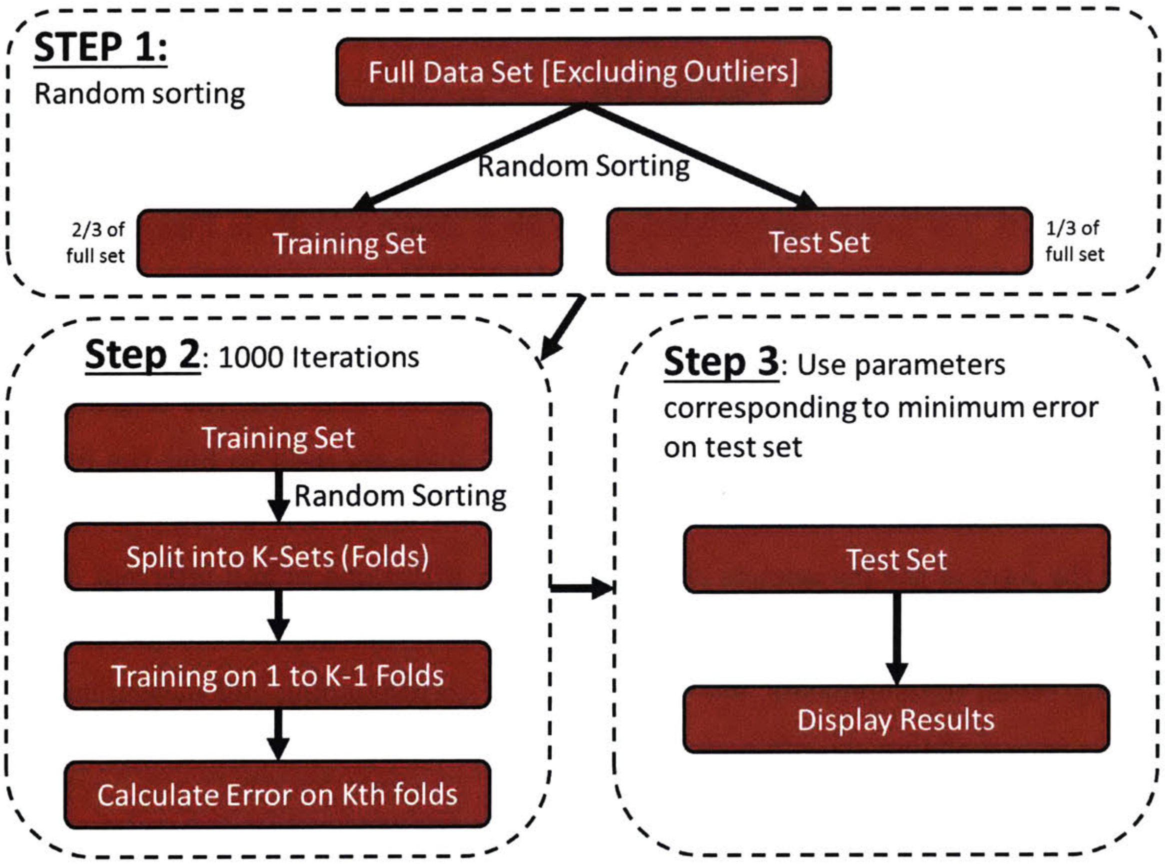

Figure 3-5: The k-fold cross-validation algorithm work flow.

above requires about 24 hours to obtain a result. This must be improved in order to have a feasible medical device.

In order to improve the speed, a table look-up approach can be used. In this approach, many sets of optimization input parameters are first used in the optimization to obtain the corresponding blood pressure results. The input parameters are the slopes and y-intercepts of the diastolic and systolic minor axis versus force plots (i.e. the parameters defining the blue lines in Figure 3-3). The output results are systolic and diastolic blood pressure. These optimizations are pre-calculated and stored. See Table 3.3 for an abbreviated sample of the table calculated for this real-time optimization approach.

Table 3.3: Sample portion of the look-up table used during the real-time optimization approach. The results displayed here are the raw algorithm results, before any calibration procedures were completed.

Algorithm Input				**Algorithm Output**	
Slope at Systole (mm/N)	Y-Intercept at Systole (mm)	Slope at Diastole (mm/N)	Y-Intercept at Diastole (mm)	Diastolic Pressure (mmHg)	Systolic Pressure (mmHg)
-0.15	2.50	-0.008	0.70	47.50	91.34
-0.02	2.50	-0.15	2.40	85.53	157.52
-0.15	4.50	-0.15	2.40	85.53	136.52
-0.02	4.50	-0.15	2.40	57.02	147.02
-0.03	3.00	-0.05	3.00	91.28	120.15

When the technique is used on a patient, their artery is segmented out of the ultrasound images and the segmentation results are interpolated onto the pre-calculated table of input parameters versus output results. This interpolation takes much less than one second for each patient. Since the segmentation algorithm has been implemented in real-time in the literature, the proposed technique is feasible for real-time estimation of blood pressure.

3.6 Bone Location Determination

In order to utilize the computational model variation discussed in Section 2.6, the location of the bone should be found in each ultrasound image in the sequence. The location of the bone is found using a simple texture-based image processing approach suggested in the Matlab documentation [85].

The process used to find the location of the bone is shown in Figure 3-6. The original ultrasound image is shown in Figure 3-6a. Next, the entropy of the ultrasound image is found using an entropy filter and then the image is converted to gray scale; in particular, the Matlab built-in function 'entropyfilt' is used and the result is shown in Figure 3-6b. Next, a filling procedure is applied using the Matlab built-in function 'imfill' and the result is shown in Figure 3-6c. Then, a closing procedure is applied using, for example, the Matlab built-in function 'imclose' and the result is shown in Figure 3-6d. Finally, the image is converted to black and white, as shown in Figure 3-6e.

From the resulting black and white image, the bone is taken to be the location of the black pixel directly below the known artery center in the particular image frame; this calculation is highlighted in Figure 3-6e.

3.7 Rejection of Low Quality Force Sweeps

In order to determine if the force sweep that the sonographer completes is of high quality, certain metrics are used. For example, the artery is tracked over the entire force sweep; if the artery moves laterally too much, the pressure distribution on the face of the probe will change over the course of the force sweep and, thus, the force sweep must be rejected. Specifically, if the artery center moves laterally by over one radius, the force sweep is rejected.

Other indications of a poor quality force sweep are discussed in Section 4.4. Force sweeps are rejected for a number of reasons, including for being too fast and for not spanning a large enough range of forces. Algorithmically, it is possible to determine the speed of the force sweep and the force range used during the force sweep. From that information, it would be possible to automatically reject force sweeps if they do not meet certain specifications. In this dissertation, force sweeps are rejected by-hand.

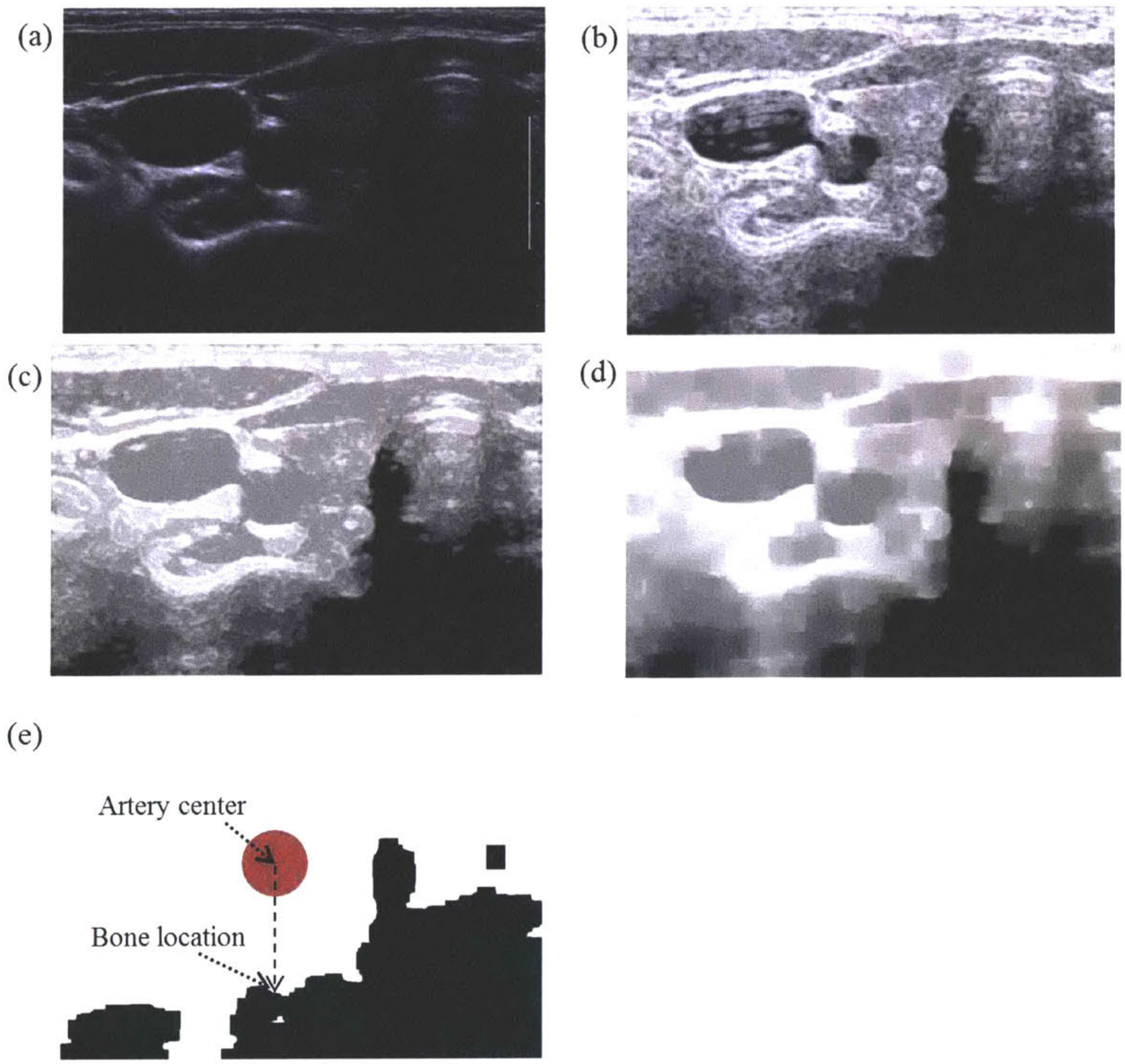

Figure 3-6: The process used to find the bone location in each ultrasound image. In (a), a typical ultrasound image frame in the study is shown. In (b), the entropy filter has been applied and the image has been converted to gray scale. In (c), the image fill function has been applied. In (d), the image close function has been applied. In (e), the image has been converted to black and white.

3.8 Summary

In this chapter, the algorithmic details of the arterial blood pressure measurement technique were discussed. In particular, the three-tap synchronization method was discussed in order to correlate force data and ultrasound data. The segmentation procedures were detailed, the optimizations were formulated, and the optimization solution procedures were discussed. The k-fold cross-validation calibration step was detailed and an approach to real-time estimation of blood pressure was presented. An algorithm to determine bone location in each ultrasound frame was described and, finally, criteria for the rejection of low quality force sweeps were discussed.

Chapter 4

Data Acquisition

This chapter describes the clinical data acquisition procedures and parameters used to obtain the results shown in subsequent chapters. For each set of volunteers, different machines and different acquisition parameters were used based on convenience and clinical considerations. However, there are many commonalities with regard to data acquisition between each set of volunteers. These commonalities are discussed in this chapter while the specifics of each data set gathered will be discussed immediately before the results are presented in Chapters 5-7.

4.1 Clinical Work Flow

Typically, when a volunteer agrees to participate in the IRB approved study, the first thing that happens is explaining the study, answering any questions that the volunteer might have about the study, and obtaining informed consent through the form of a signature. The patient then lies down on the hospital bed. An oscillometric cuff, such as the one shown in Figure 4-1, is placed by a trained medical professional on the patient's upper arm and the start button is pressed. The reading is recorded and the sonographer then proceeds with taking ultrasound data.

The sonographer completes ten force sweeps on the patient's right carotid artery proximal to the bifurcation in the neck. It is important to note that the method described in this dissertation is applicable to any artery whose deformations are visible with ultrasound; the carotid was chosen as the first site to test the method because of imaging convenience and consistency during force sweeps.

During each force sweep of the carotid artery, the sonographer is instructed to complete three taps on the patient then slowly increase force through a specified range, typically between 1 N and 12 N. During the sweeps, the ultrasound images and force data are recorded on separate machines. After the force sweeps, another measurement with the oscillometric cuff is made on the brachial artery. The study concludes after this last cuff measurement is taken.

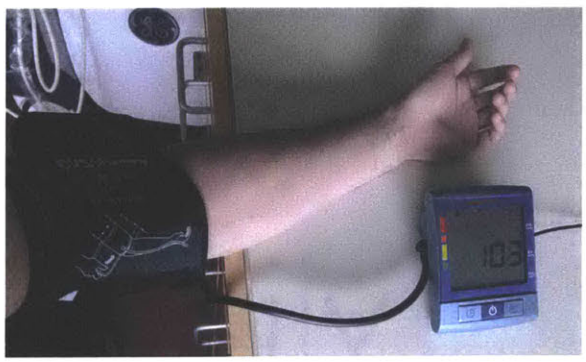

Figure 4-1: Photo of one of the oscillometric cuffs used in this work. After pressing the start button on the device, it automatically inflates and deflates, then it reports the blood pressure.

See Figure 4-2 for the typical set up during a data acquisition session at Massachusetts General Hospital (MGH). The laptop collecting the forces is in the background, the ultrasound machine shows a typical ultrasound image, and the sonographer is using the force measurement attachment on the volunteer. Each of these aspects of the data acquisition are described in the following sections.

4.2 Imaging

There are two different ultrasound machines used in this dissertation. A photo of one of the machines used, the General Electric (GE) Logiq E9 machine (General Electric, Boston, MA, USA) with 9L-D linear transducer (General Electric, Boston, MA, USA), is shown in Figure 4-3. For details of each machine used, see the following results chapters.

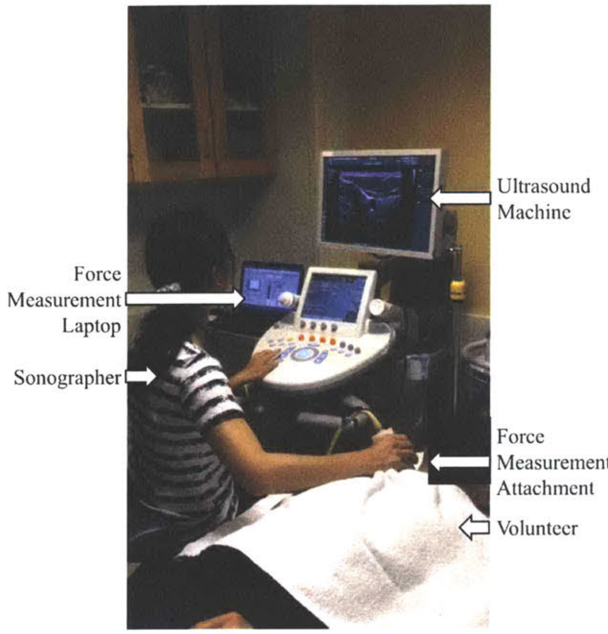

Figure 4-2: Orientation of the ultrasound system, sonographer, patient, and force measurement laptop during data acquisition at MGH.

A typical ultrasound image, obtained using a Supersonics Imagine Aixplorer machine (Aixplorer, SuperSonic Imagine, Aix-en-Provence, France), is shown in Figure 4-4; in the figure, the the lumen of the carotid artery is shown as the dark ellipse near the center of the image. Typical locations of anatomical features in the neck are shown in a cartoon in Figure 4-5; in the cartoon, the bone, trachea, muscle, thyroid, and location of the esophagus is shown relative to the carotid artery. Certain features of the cartoon, such as the bone, include typical elasticity values of the feature in order to obtain intuition for the anatomy.

As shown in Figure 4-4, the artery was imaged through its cross-section, rather than through the longitudinal axis of the artery as shown in Figure 4-6; the reason for this can be explained by the following logic. While longitudinal plane images (such that the array long axis runs parallel to artery length) allow for easy calculation of artery dimension, they are highly position dependent, error prone, and difficult for non-expert sonographers to achieve repeatably. The cross-sectional images are chosen because of their simplicity and repeatability.

Figure 4-3: Photo of one of the ultrasound systems (GE Logiq E9) used in this dissertation. The carotid artery is being imaged in the photo.

4.3 Force Measurement

The contact force between the surface of the ultrasound probe and the surface of the tissue is measured using an acrylonitrile butadiene styrene (ABS) plastic 3D printed attachment to the ultrasound probe with a strategically placed load cell, as shown in the solid modeling mock-up in Figure 4-7. The force measurement attachment has essentially three different parts. Part 1 is a tight-fitting plastic attachment to the probe; Part 2 is the load cell; Part 3 is the outer ergonomic clamshell that the sonographer holds. By connected Part 1 to Part 2 and then Part 2 to Part 3, the contact force can be accurately measured. In Figure 4-8, the attachment is shown ready for use in (a) and is shown with the inner tight-fitting piece visible in (b). This ergonomic attachment has been discussed in a number of papers in the literature [86–88] and used within the hospital work flow in a number of clinical trials. The force is recorded as the average force over the face of the probe in contact with tissue. LabView (Version

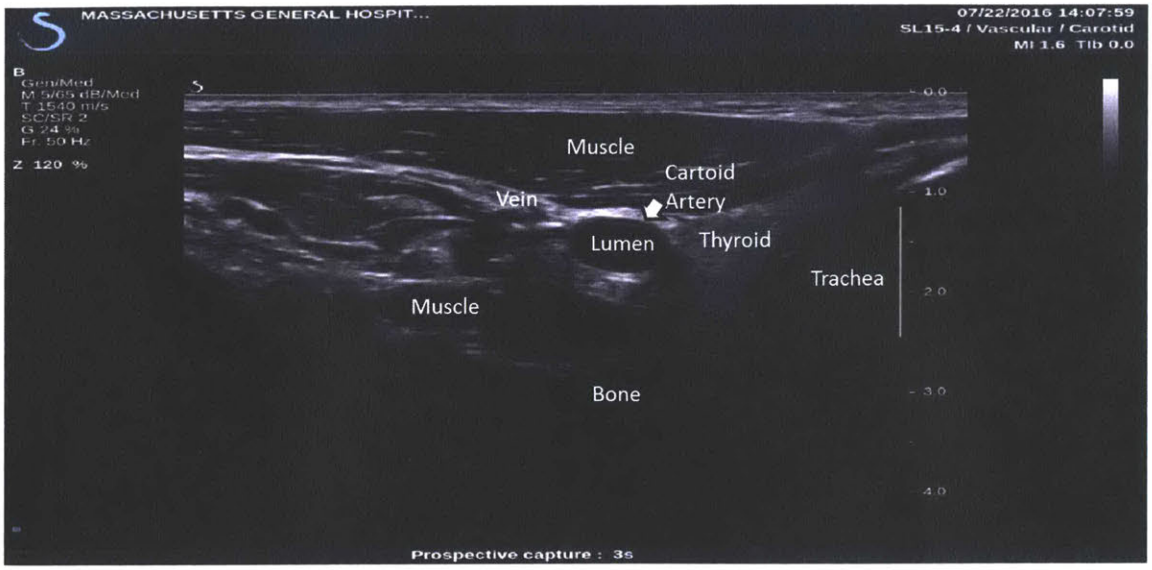

Figure 4-4: Screen capture of a typical ultrasound image obtained in the study at Massachusetts General Hospital. The ultrasound probe is pushing on the skin from the top surface of the image while the neck bone is located at the bottom of the image.

2015, National Instruments, Austin, Texas, USA) is used to aid in the data acquisition. See Figure 4-9 for the LabView program used to gather data and Figure 4-10 for a screen capture of the LabView program in use. The program, which was developed by Dr. Matthew Gilbertson and Athena Huang, displays the force to the user in real-time during the force sweep.

The DICOM ultrasound files for each force sweep were recorded and, as discussed above, the force data was recorded with LabView. Since the force data was captured on a laptop separate from the ultrasound machine, correlation between the force data and image data was necessary. In order to correlate the image files and the force files, the three tap synchronization method was used, as discussed in Section 3.1.

4.4 Avoiding Poor Data

Force sweeps are rejected if (1) the sonographer forgot to complete the three taps on the neck, (2) the force sweep was too fast, which meant that segmentation results would not be a clear function of force, (3) the artery moved laterally too much, defined as moving more than a radius in either the left or right direction over the duration

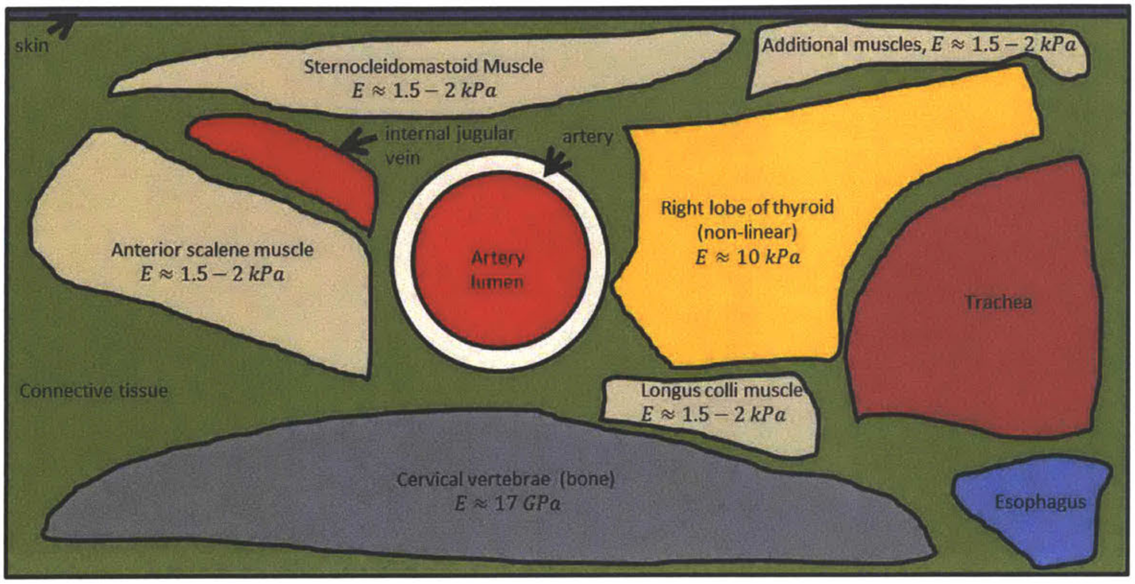

Figure 4-5: The cartoon shows the approximate location of anatomical features in the neck. In the orientation displayed here, the ultrasound probe is located next to the skin on the top surface of the cartoon. Typical elasticity values are displayed on some features in the cartoon.

of the force sweep, which indicates significantly varying pressure profiles over the probe face, (4) the force sweep did not span a large enough range of forces to allow a sufficient plot of artery minor axis versus force needed for the optimization algorithm, and (5) the carotid artery was accidentally imaged close to or at the bifurcation in the neck.

4.5 Summary

In this chapter, the procedures and devices used for data acquisition were discussed. In particular, the overall set up and patient work flow was detailed. Imaging was discussed and the method for force measurement was outlined. Finally, reasons for poor data were summarized in order to better understand the data acquisition process.

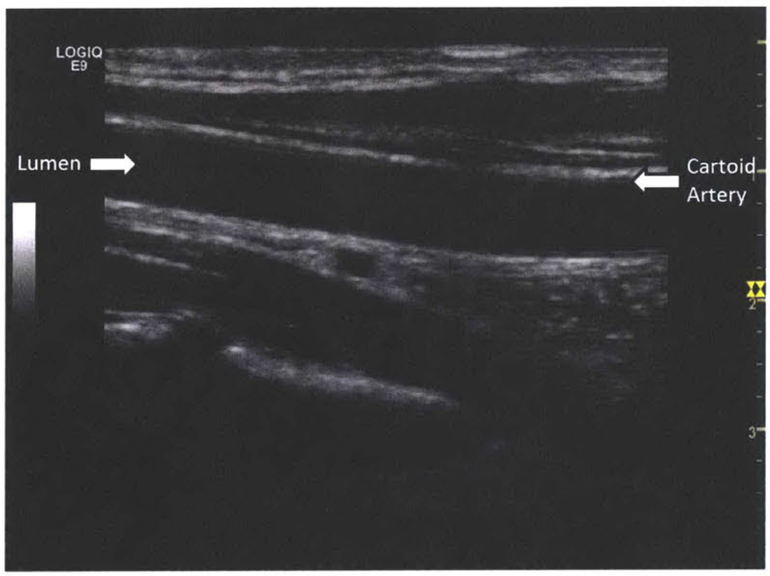

Figure 4-6: Screen capture of an ultrasound image in which the carotid artery is imaged through its axis (i.e. longitudinally).

Figure 4-7: Solid modeling mock-up of the force measurement attachment used during this dissertation. The red clamp is attached to the blue outer clam shell through a load cell. Note that while the image shows a curved probe, only linear probes were used in this dissertation. The device was developed by Dr. Matthew Gilbertson and Athena Huang.

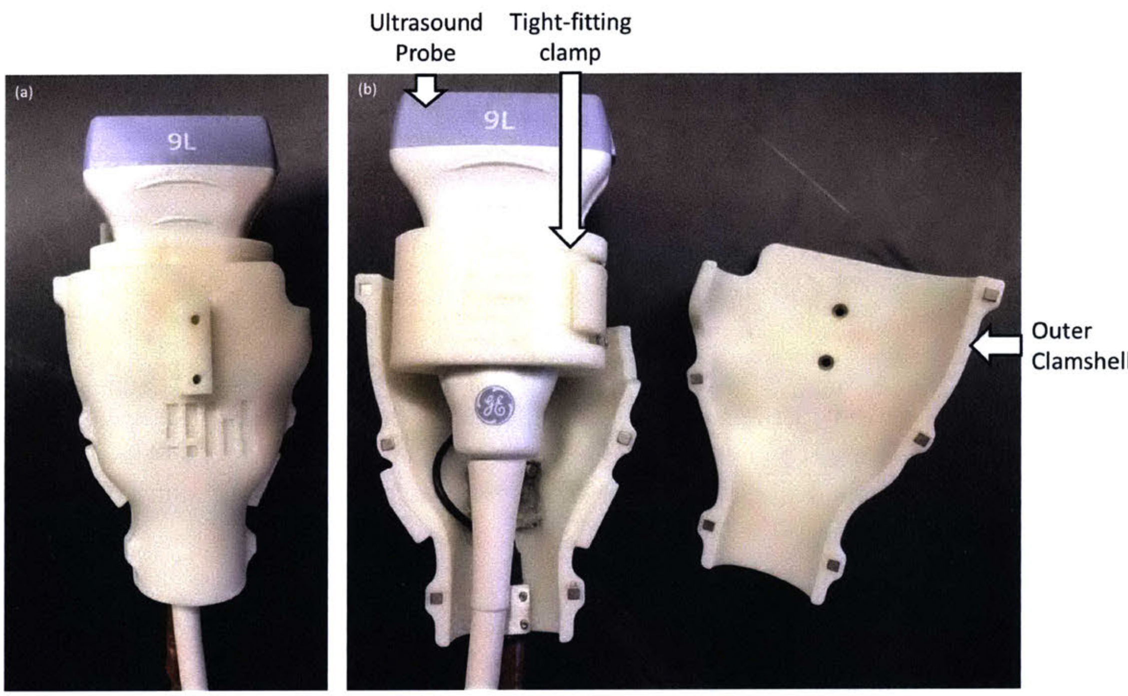

Figure 4-8: The ultrasound force measurement attachment. The 3D-printed attachment is shown attached to a GE Logiq E9 linear 9L-D probe. In (a), the attachment is ready for use. In (b), the attachment is split apart so that the inner tight-fitting piece is visible. The device was developed by Dr. Matthew Gilbertson and Athena Huang.

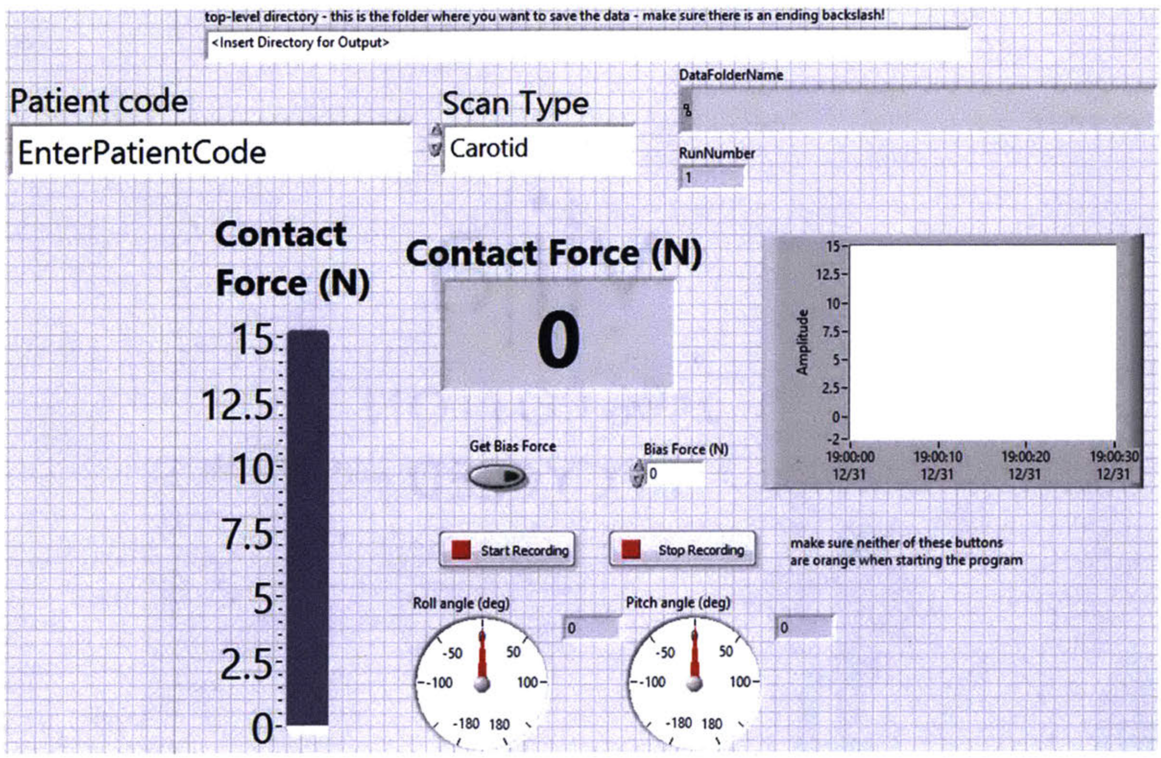

Figure 4-9: The LabView program used in order to record the applied force between the ultrasound probe and the tissue. The applied force is displayed in real time to the user. This program was designed by Dr. Matthew Gilbertson and Athena Huang.

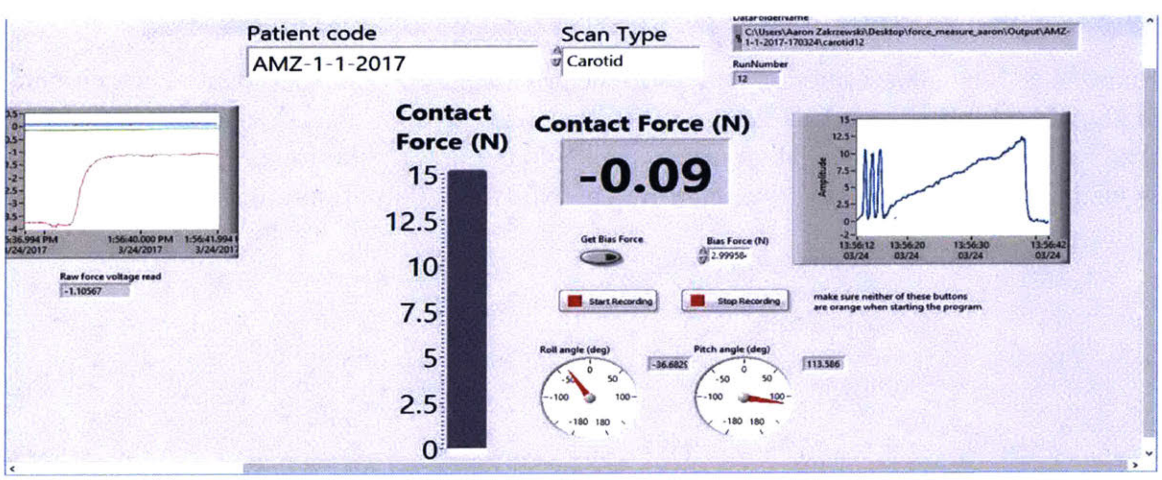

Figure 4-10: Screen capture of the LabView program in use. This program was designed by Dr. Matthew Gilbertson and Athena Huang.

Chapter 5

Sonographer Scans on Healthy Volunteers

In this chapter, the technique described in Chapters 1 - 4 is applied to nominally healthy volunteers. In particular, this chapter focuses on scans completed by a trained sonographer while Chapter 6 focuses on scans completed by the volunteer him/herself (termed 'self-scans' in this dissertation).

5.1 Data Acquisition Specifics

The Massachusetts General Hospital (MGH) Institutional Review Board (IRB) and the Massachusetts Institute of Technology (MIT) IRB approved the following study. Volunteers for this study gave informed consent. Inclusion criteria included (a) being over 18 years of age and (b) non-pregnant mothers. Exclusion criteria included (a) volunteers with pacemakers and (b) overweight volunteers (BMI 30 $\frac{kg}{m^2}$ and greater).

At MGH, the nominally healthy volunteer was given the ultrasound exam by a trained sonographer and an automatic oscillometric blood pressure cuff (Spot Vital Signs Device, Welch Allyn, Skaneateles Falls, New York, USA) was used to measure systolic and diastolic blood pressure as specified in Section 4.1. The right carotid artery proximal to the bifurcation in the neck of the supine volunteer was imaged using a Supersonic Imagine Aixplorer research ultrasound machine (Aixplorer, SuperSonic Imagine, Aix-en-Provence, France) with a 256 element linear SL15-4 probe (SuperLinear SL15-4, SuperSonic Imagine, Aix-en-Provence, France).

Due to the memory limitations of the ultrasound machine, force sweeps were limited to approximately 10 second lengths which allows for over 10 cardiac cycles per force sweep. Longer force sweeps would allow for more cardiac cycles to be recorded, a more slowly increasing force, and, ultimately, even better data. However, due to memory limitations, on each volunteer, 10 force sweeps were completed: 5 force sweeps from 1.5 to 8 N and 5 force sweeps from 6 to 12 N. Ten sweeps were chosen in order to be sure that adequate data was obtained.

5.2 Techniques to Evaluate Algorithm Performance

In order to evaluate the accuracy of the technique, algorithm estimates of arterial blood pressure are compared to oscillometric blood pressure cuff readings. Two ways to compare measurement techniques are regression analysis and method of differences. Further information reported in this chapter include the accuracy and the precision of the algorithm; in this dissertation, the accuracy is defined as the mean of the errors (cuff minus algorithm) and the precision is defined as the standard deviation of the errors (cuff minus algorithm). Note that the correlation coefficient (r^2) has been frequently condemned in the literature for comparing two different error-prone measurement techniques and thus is not considered in this dissertation to evaluate the method [89–91].

In order to further evaluate the algorithm performance, relevant plots are generated. A typical results figure is shown in Figure 5-1; while the figure is discussed in detail in Section 5.3.1 below, it is included here in order to discuss the typical form of the results. In the typical results figure, Part A is a box plot where absolute relative error is plotted against systolic and diastolic pressure. Each point in the plot represents one volunteer in the study. The absolute relative error is calculated as

$$e = \frac{|p_i^{alg} - p_i^{cuff}|}{\frac{(p_i^{alg} + p_i^{cuff})}{2}} \tag{5.1}$$

where p_i^{alg} is the pressure reported by the algorithm, p_i^{cuff} is the average of two pressure measurements reported by the oscillometric cuff (see Section 4.1), and i represents either systolic pressure or diastolic pressure. In Part B and C of the typical results figure, Bland-Altman style plots are shown for systolic and diastolic pressure, respectively. In these plots, the vertical axis is the algorithm pressure minus the cuff pressure and the x-axis is the mean of the cuff and algorithm measurements. In Part D and E of the typical results figure, correlation plots are shown for systolic and diastolic pressure, respectively. In these plots, the cuff measurement is plotted on the y-axis and the algorithm measurement is plotted on the x-axis. The purpose of the plots above is to give information about the algorithm performance, including the possible existence of any systemic error.

5.3 Results

5.3.1 Raw Algorithm Results

While there were 26 volunteers recruited in this study, two of the volunteers yielded poor data due to the reasons specified in Section 4.4. In Figure 5-1, the raw algorithm results for the 24 volunteers are displayed. The results shown in (a)-(e) are plots as described in Section 5.2. From the figure, it is clear that the algorithm over-predicts diastolic pressure and there is a large spread on the systolic pressure data. As displayed in this figure, the *median* absolute relative error for systolic pressure (excluding the one outlier) is 8.20 % and for diastolic pressure is 19.94 %. The *mean* absolute relative error for systolic pressure and diastolic pressure is 14.13 % and 18.98 %, respectively. The accuracy and precision for systolic and diastolic pressures are -1.30 $\pm$ 20.28 mmHg and 12.01 $\pm$ 12.17 mmHg, respectively.

5.3.2 K-Fold Cross-Validation Results

The differences between the raw algorithm results and the cuff are due to the assumptions in the computational model as described in Section 2.5 and noise within the data.

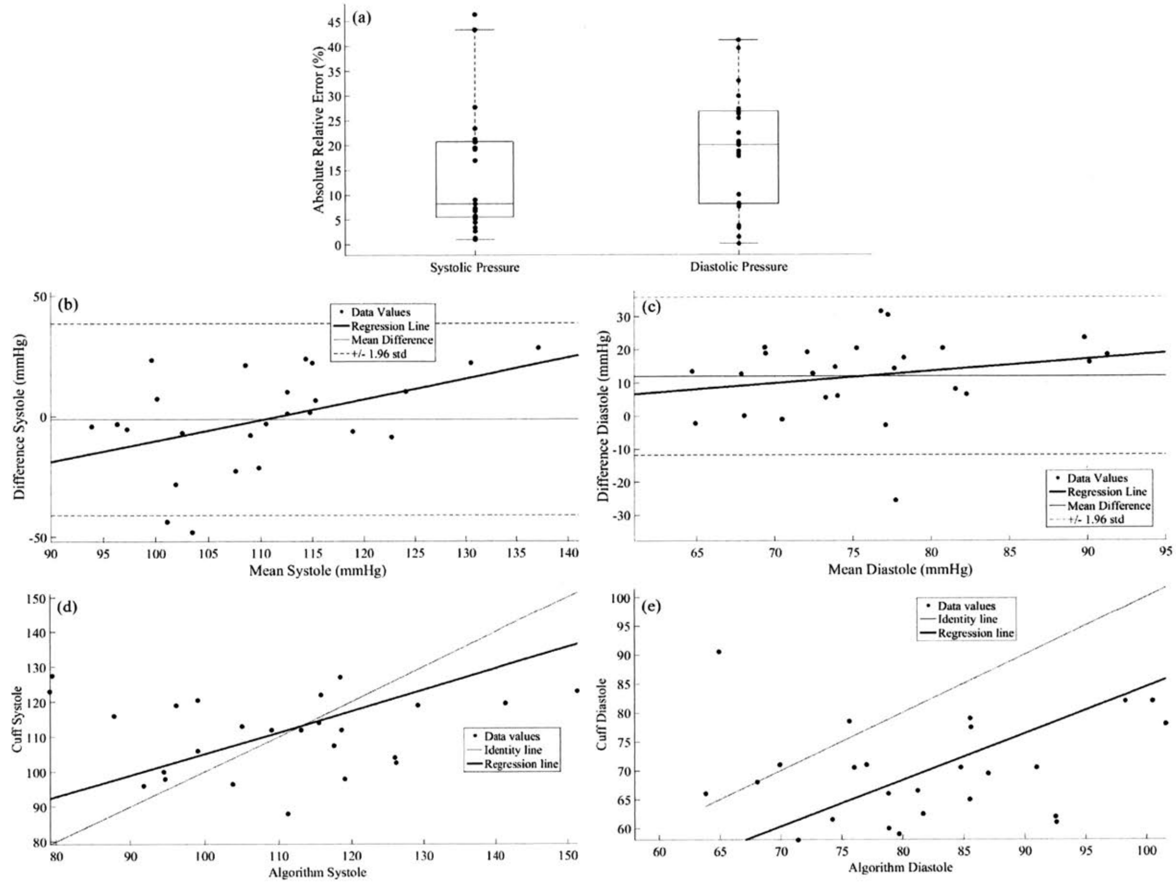

Figure 5-1: Raw algorithm results for the 24 healthy single-visit volunteers at MGH. Each point represents one volunteer in the study. The plots (a)-(e) in this figure are plotting the quantities described in Section 5.2.

As described in Section 3.4.1, the k-fold cross-validation method seeks to calibrate for these assumptions and inaccuracies.

The data is put through the k-fold cross-validation method and the results on the test set are shown in Figure 5-2. Each plot in this figure, (a)-(e), is as described in Section 5.2. Note that less points are displayed in Figure 5-2 compared to Figure 5-1 because the test set is only 1/3 of the full set (excluding outliers). The mean and median of the absolute relative error for systolic pressure are 7.14 % and 5.82 %, respectively, and for diastolic pressure are 4.85 % and 4.48 %, respectively. The accuracy and precision for systolic pressure are -1.24 mmHg $\pm$ 10.04 mmHg and for diastolic pressure are -1.45 mmHg $\pm$ 4.75 mmHg. These values must be viewed with the knowledge that the algorithm is being compared to the oscillometric cuff, which, as discussed in Section 1.3.3, is not a ground truth measurement.

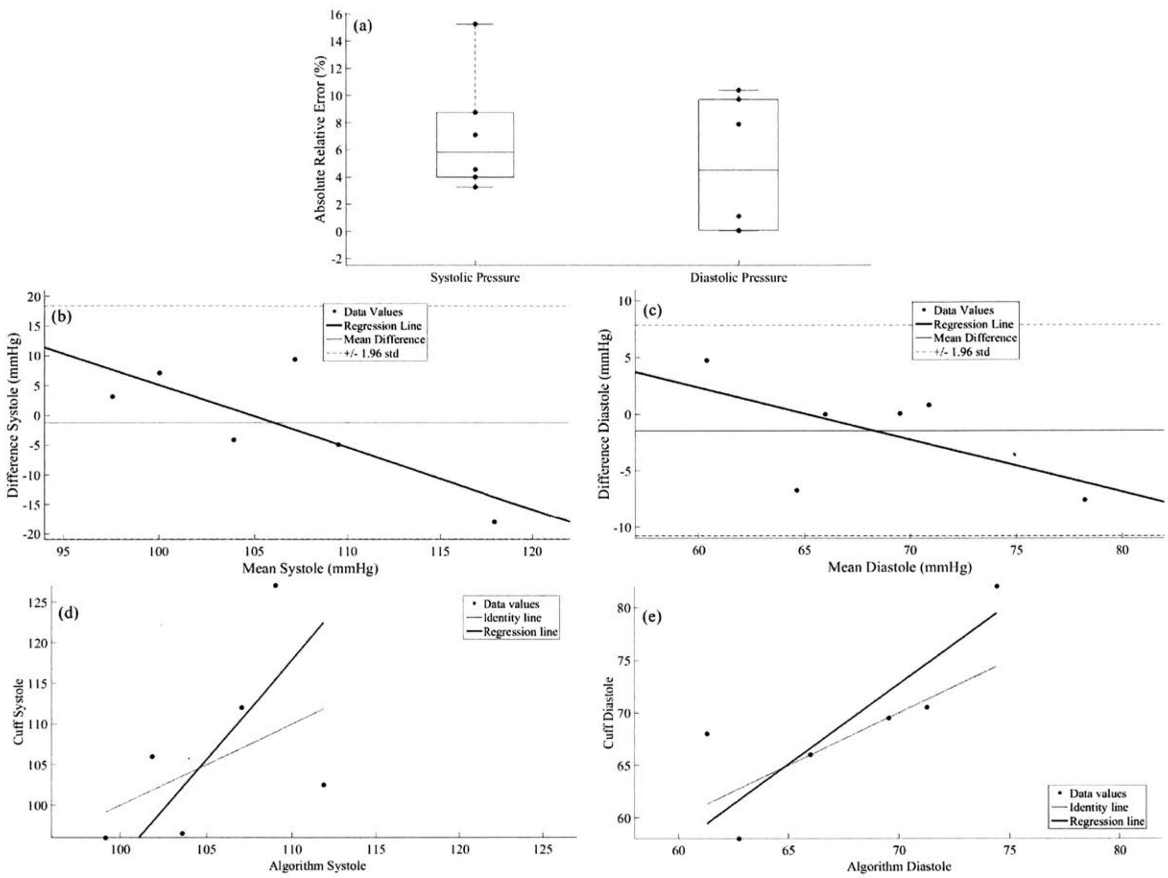

Figure 5-2: Results on the test set after the k-fold cross-validation method is applied to the 24 healthy volunteers at MGH. Each point represents one volunteer in the study. The plots (a)-(e) in this figure are plotting the quantities described in Section 5.2.

Finally, the k-fold cross-validation parameter set is applied to the full set and the results are displayed in Figure 5-3. As before, the plots in this figure are as described in Section 5.2. The mean and median of the absolute relative error for systolic pressure are 9.30 % and 7.09 %, respectively, and for diastolic pressure are 9.59 % and 8.53 %, respectively. From the data, the accuracy and precision for systolic pressure are -5.25 mmHg $\pm$ 12.37 mmHg and for diastolic pressure are -2.55 mmHg $\pm$ 8.81 mmHg.

Because of the random sorting in the k-fold cross-validation method, each run of the cross-validation algorithm yields different results. In order to quantify the performance of the technique and ensure that one run was not 'lucky' with the random sorting, k-fold cross-validation is performed for 2000 different random sortings. The

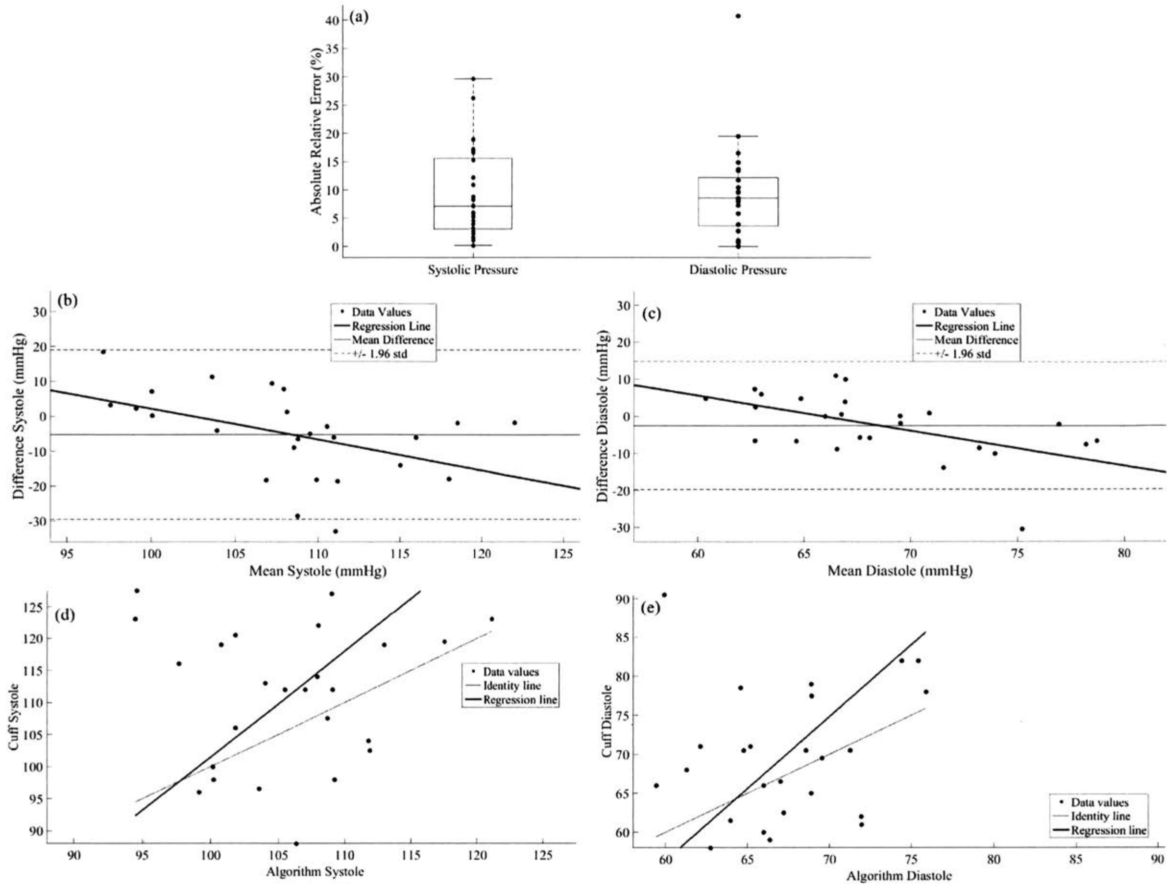

Figure 5-3: Plots showing algorithm performance after applying the k-fold parameter set to the full set of 24 healthy volunteers at MGH. Each point represents one volunteer in the study. The plots (a)-(e) in this figure are plotting the quantities described in Section 5.2.

statistics are shown in Table 5.1.

5.3.3 Discussion

The accuracy and precision of the technique described in this dissertation is best represented by the results above; in particular, the accuracy and precision for systolic pressure is -1.24 mmHg $\pm$ 10.04 mmHg and for diastolic pressure is -1.45 mmHg $\pm$ 4.75 mmHg.

At its fastest, data acquisition for each volunteer using this setup took 6 to 7 minutes from start to finish. As data acquisition procedures are optimized, the required time for data acquisition will be much lower. For example, through acquiring data,

Table 5.1: Statistics obtained after running the k-fold cross-validation method for 2000 different random sortings into training set and test set. The results here correspond to the 24 healthy single-visit volunteers at MGH. In this table, α is a 2000 element vector where each element of the vector is the mean of the errors in a particular random sorting.

	Mean of α (mmHg)	Minimum of α (mmHg)	Maximum of α (mmHg)	Minimum of Test Set Errors (mmHg)	Maximum of Test Set Errors (mmHg)
Systolic	-0.64	-15.30	14.98	-33.67	27.97
Diastolic	-0.31	-10.99	10.44	-35.65	15.58

it was learned that if the artery slips between the probe and the bone, a low quality force sweep results. By eliminating slippage of the artery, more consistent and higher quality force sweeps were obtained. Using such knowledge, it is feasible for only one 10-second force sweep to be needed in order to report blood pressure to the operator. As another example, while the current force range is from 1.5 N to 12 N, there is likely to be a small range that is acceptable for the method (e.g. between 1.5 N and 4 N). This change to the data acquisition procedures will reduce the time needed for the force sweep. In the practical implementation of the algorithm, no cuff measurements and only one force sweep will be necessary, thus reducing the data acquisition time to 10 seconds, which is less than the time needed for an oscillometric cuff measurement (approximately 40-45 seconds).

5.4 Real-Time Implementation of Algorithm

The real-time algorithm discussed in Section 3.5 was tested on a portion of the healthy-volunteer data set described above in Section 5.1. Specifically, 21 of the volunteers were tested using the real-time table look-up approach. The k-fold parameter set found in Section 5.3.2 was applied to the real-time results and the relevant plots are shown in Figure 5-4. Each part of the figure plots the quantities discussed in Section 5.2. The accuracy and precision for systolic and diastolic blood pressure are -5.19 mmHg $\pm$ 10.68 mmHg and -3.85 mmHg $\pm$ 7.98 mmHg, respectively. The mean and median of the absolute relative error for systolic pressure are 8.27 % and 5.26 %, respectively, and for diastolic pressure are 8.25 % and 4.70 %, respectively.

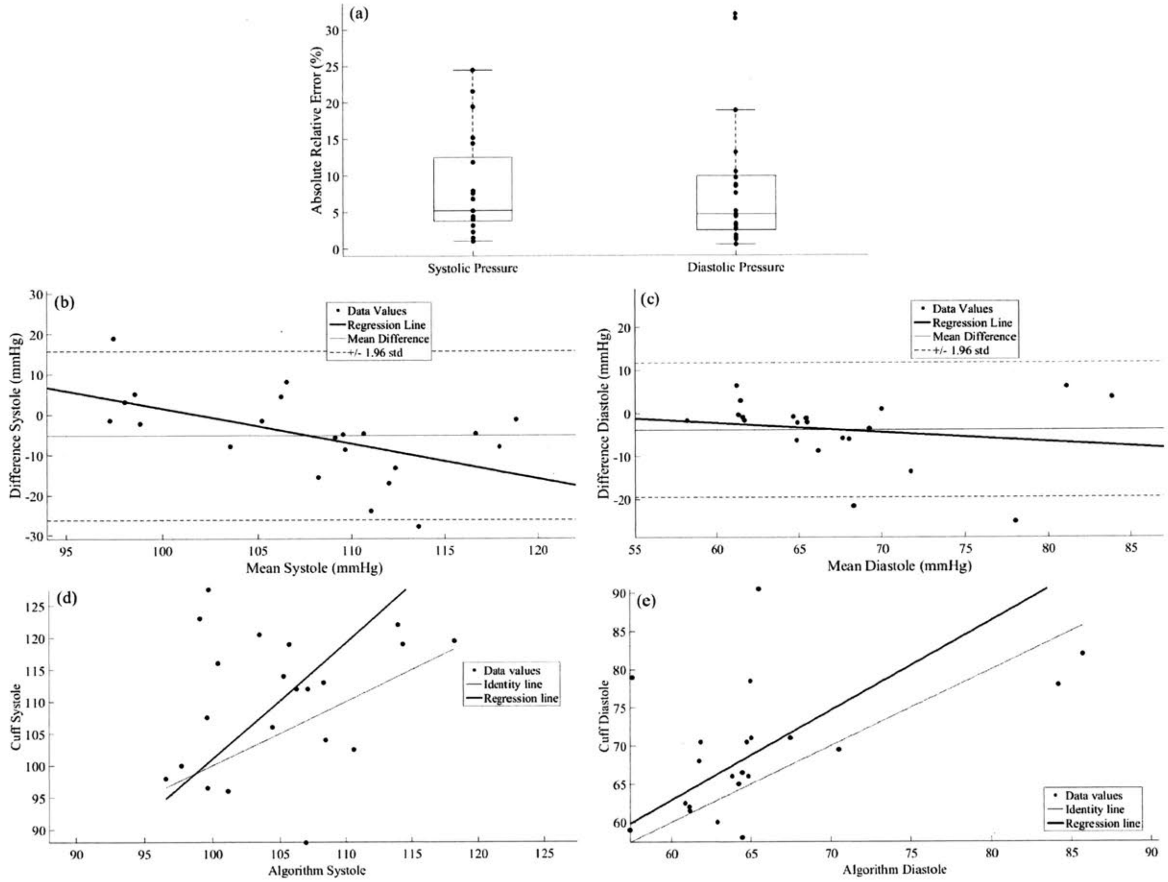

Figure 5-4: Results of the real-time table lookup approach on 21 healthy single-visit volunteers. The k-fold parameters found previously in this chapter have been used to generate this plot. The plots (a)-(e) in this figure are plotting the quantities described in Section 5.2.

5.4.1 Discussion

With the real-time implementation results presented above, every step of the process after the force sweep has the potential to be implemented in real-time. While the oscillometric cuff takes between 40 and 45 seconds to inflate, deflate, and report a blood pressure reading, the force sweeps above only took 10 seconds each. Thus, the technique in this dissertation has the potential to be faster than the cuff measurements. Any differences between the results presented above and the results presented in Section 5.3.2 are due to interpolation error; as more rows to the table are added, the interpolation error will decrease.

5.5 Results After Including Bone in the Computational Model

As discussed in Sections 2.6 and 3.6, one version of the computational model includes the bone below the artery. In this section, the bone model was applied to 10 volunteers in the data set described in Section 5.1. The raw algorithm results are shown in Figure 5-5. The mean and median of the absolute relative error are 9.80 % and 5.52 % for systolic pressure, respectively, and 20.12 % and 23.34 % for diastolic pressure, respectively. The precision and accuracy of the algorithm for systolic pressure are 10.80 mmHg ± 7.80 mmHg and for diastolic pressure are 13.10 mmHg ± 12.73 mmHg.

The algorithm results, after the k-fold cross-validation algorithm is applied, are shown for the test set in Figure 5-6. The mean and median of the absolute relative error are 7.21 % and 8.91 % for systolic pressure, respectively, and 13.44 % and 17.16 % for diastolic pressure, respectively. The precision and accuracy of the algorithm for systolic pressure are -4.59 mmHg ± 7.17 mmHg and for diastolic pressure are 8.71 mmHg ± 5.43 mmHg. The statistics for the k-fold cross-validation method are shown in Table 5.2.

Table 5.2: Statistics obtained after running the k-fold cross-validation method for all sortings into training set and test set. The results shown are those in which the bone was included in the computational model. In this table, α is a vector where each element of the vector is the mean of the errors in a particular random sorting.

	Mean of α (mmHg)	Minimum of α (mmHg)	Maximum of α (mmHg)	Minimum of Test Set Errors (mmHg)	Maximum of Test Set Errors (mmHg)
Systolic	-0.46	-11.09	13.26	-17.48	19.88
Diastolic	-1.79	-47.79	13.17	-60.35	14.22

The algorithm results, after the k-fold cross-validation parameter set found above is applied to the full set, is shown in Figure 5-7. The mean and median of the absolute relative error are 6.89 % and 7.60 % for systolic pressure, respectively, and 9.45 % and

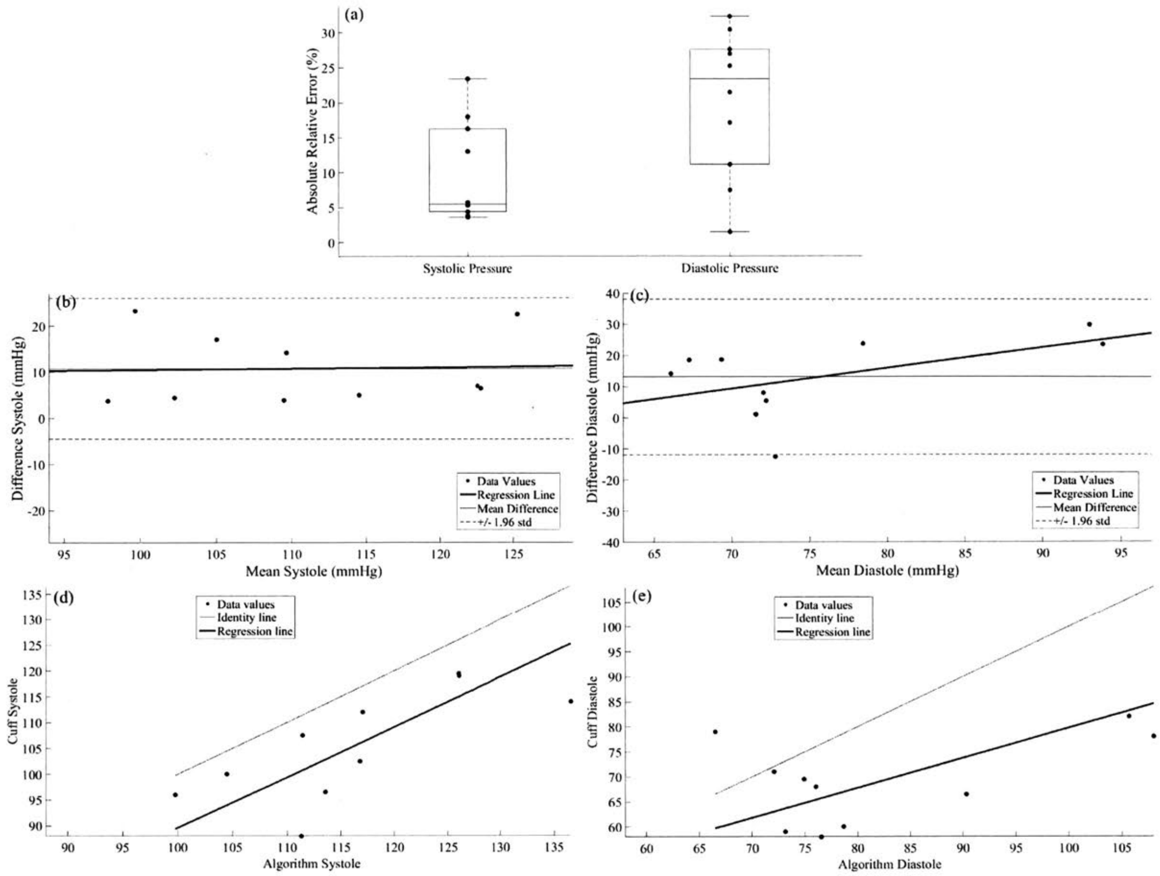

Figure 5-5: Results of the technique after including the bone in the computational model. The results displayed are the raw results of the algorithm. The plots (a)-(e) in this figure are plotting the quantities described in Section 5.2.

8.92 % for diastolic pressure, respectively. The precision and accuracy of the algorithm for systolic pressure are -2.89 mmHg $\pm$ 7.43 mmHg and for diastolic pressure are 2.31 mmHg $\pm$ 7.80 mmHg.

5.5.1 Discussion

The addition of the bone in the computational model is a first step towards more model fidelity. The results above show that, on a whole, the accuracy and precision became worse with the addition of the bone in the computational model. The reason behind this result might be because the bone finding algorithm in Section 3.6 needs to be improved. It is also important to remember that the algorithm results are compared to the oscillometric cuff and that the bone only represents one part of the

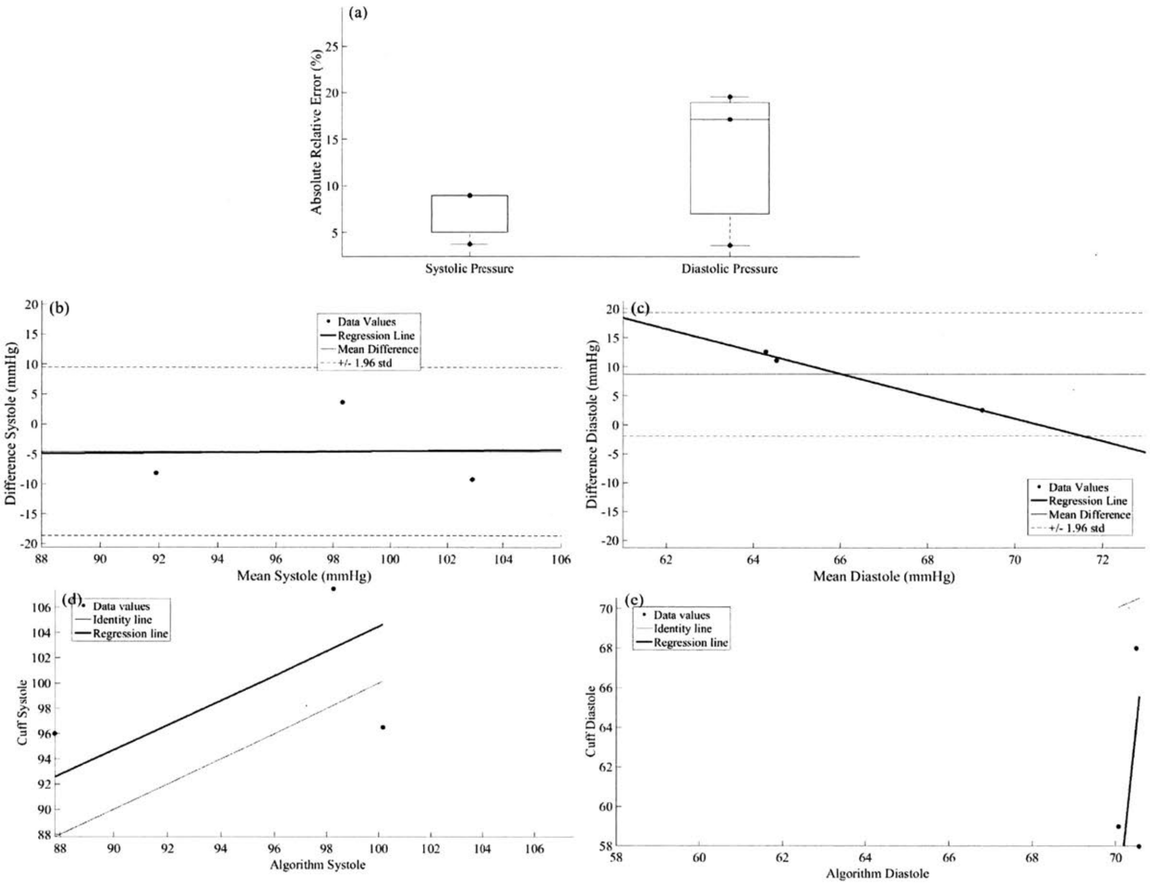

Figure 5-6: Results of the technique after including the bone in the computational model. The results displayed are the k-fold cross-validation results on the test set. The plots (a)-(e) in this figure are plotting the quantities described in Section 5.2.

tissue surrounding the artery. Further, only ten volunteers were investigated in the results above; this means that the test set of the k-fold cross-validation algorithm is rather small; by applying the new model to even more volunteers, a better idea of the accuracy could be obtained.

5.6 Algorithm Performance Metrics

5.6.1 Intraobserver Repeatability

As specified in Section 5.1, 10 force sweeps were taken for each volunteer in this study. Note that only one force sweep is needed to calculate blood pressure. Thus, there is enough data to complete an intraobserver variability analysis of the results.

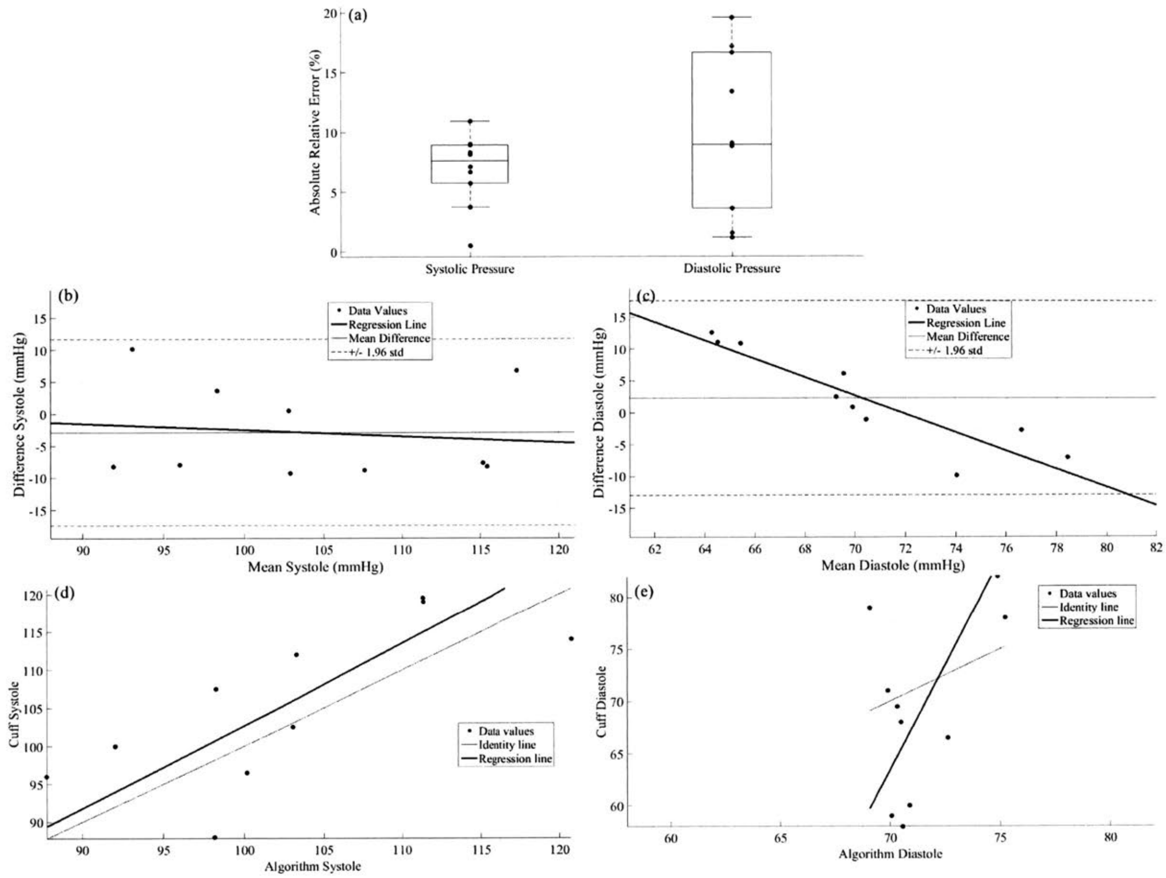

Figure 5-7: Results of the technique after including the bone in the computational model. The results displayed are the k-fold cross-validation parameter set applied to the full data set. The plots (a)-(e) in this figure are plotting the quantities described in Section 5.2.

In order to quantify repeatability, two force sweeps were separately used to calculate blood pressure for each of 10 volunteers. The blood pressure reading from the first force sweep chosen was compared to that of the second force sweep chosen. In Figure 5-8, intraobserver repeatability is quantified by plotted the two readings; systolic repeatability is shown in (a) and diastolic repeatability is shown in (b). The results shown in the figure are after the application of the k-fold cross validation parameter set found above in Section 5.3.2. Results indicate that there is room for improvement regarding algorithm repeatability. The mean difference between systolic pressure reading 1 and systolic pressure reading 2 is 12.20 mmHg and, the corresponding number for diastolic pressure is 4.61 mmHg. Possible improvement of these numbers could be obtained by standardizing the location on the neck where measurements are taken.

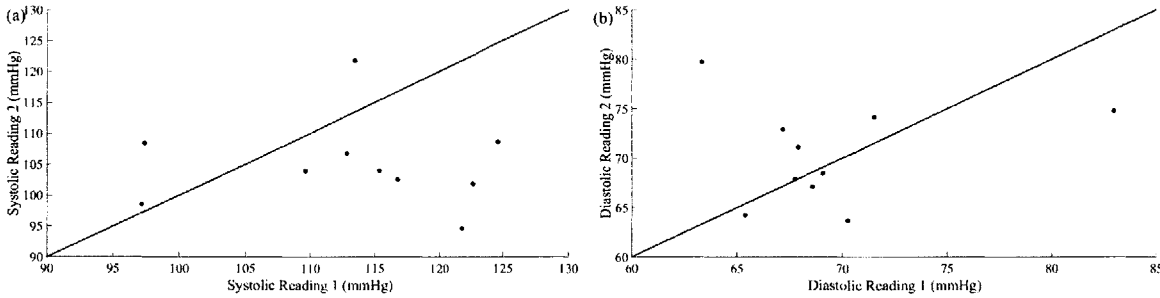

Figure 5-8: Intraobserver repeatability for systolic pressure (a) and diastolic pressure (b).

5.6.2 Sensitivity Analysis

In order to determine if the optimization is well-conditioned, the condition number of the process was calculated. The condition number is defined as

$$ConditionNumber = \frac{||J(x)||}{\frac{||f(x)||}{||x||}} \tag{5.2}$$

where J is the Jacobian, f is a finite element function evaluation yielding a vector of objective function values at each force in the specified force range, and x is a vector of input parameters to the finite element function. In this equation, 2-norms are used. The Jacobian is a matrix with i rows and j columns, and is defined as

$$J_{ij} = \frac{\partial f_i}{\partial x_j} \tag{5.3}$$

The derivatives are calculated using the finite difference formula

$$f'(x) = \frac{f(x+h) - f(x)}{h} \tag{5.4}$$

where h represents an approximately 1 % change of the parameter in question.

The condition number surface in this case has five dimensions: (1) y-intercept at systole, (2) slope systole, (3) y-intercept at diastole, (4) slope diastole, and (5) condition number. In order to visualize the data, a projection into three dimensions is taken:

(1) y-intercept at systole, (2) y-intercept at diastole, and (3) condition number. The condition number was calculated at four different points for one particular volunteer. These points were centered about the parameter set corresponding to the minimum of the objective function. See Figure 5-9 for a visualization of the surface. As the figure indicates, the magnitude of the condition number is 10^2. This means that two digits of accuracy are lost in the process in addition to any arithmetic precision losses. This is a low condition number and indicates that the problem is well-conditioned.

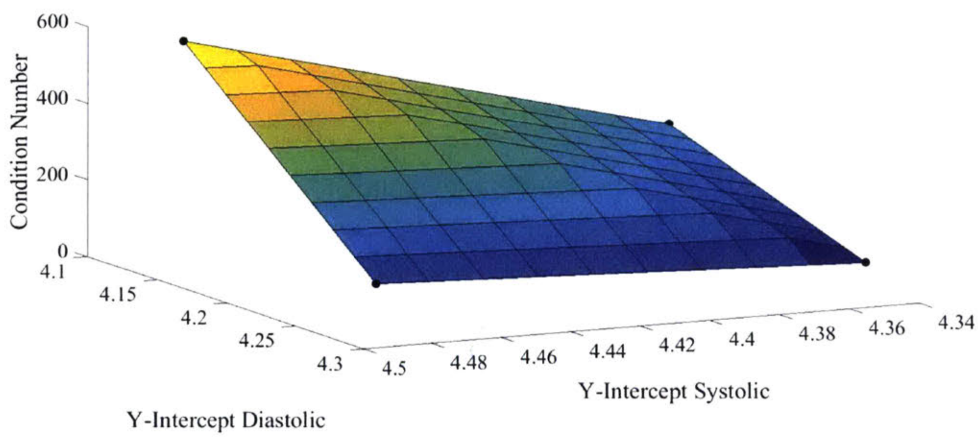

Figure 5-9: Condition number surface plot for one healthy volunteer in the study at MGH. Four points are displayed in this figure.

5.6.3 Affect of Artery Thickness on the Accuracy of the Technique

In order to determine if the accuracy of the technique is affected by the artery thickness, Figure 5-10 has been generated. In the figure, percent absolute relative error is plotted versus the artery thickness calculated in optimization 2. Note that this artery thickness corresponds to the reference configuration, as described in Section 3.3.2. From the plot, it is clear that there are outliers at both systole and diastole for high artery thicknesses; these outliers impact the trendlines.

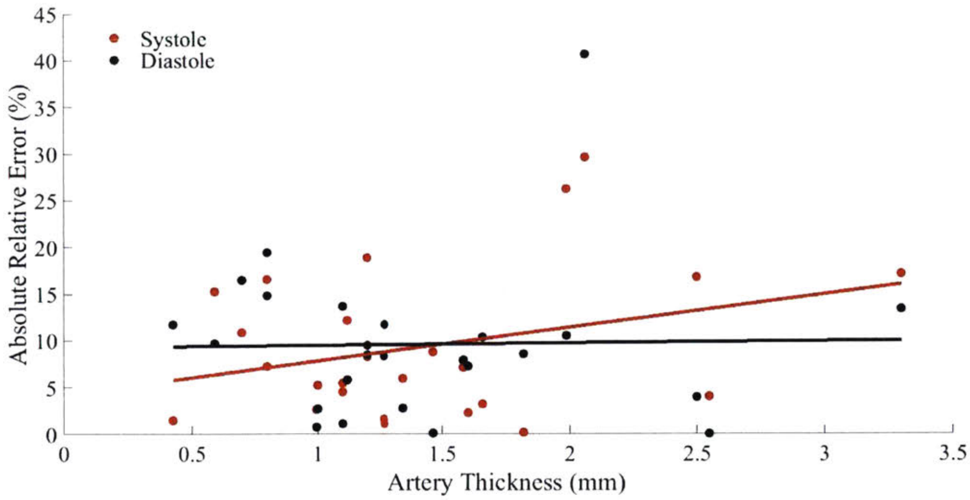

Figure 5-10: Plot of the percent absolute relative error at systole and diastole versus the artery thickness calculated by the optimization.

5.6.4 Smaller Force Ranges

In order to increase the clinical feasibility of the technique developed in this dissertation, it is important to consider how different force ranges affect the technique's accuracy. The implementation above uses a force range of 8 N to 12 N; it is worth investigating the accuracy of the technique for different ranges. In this section, the accuracy of the technique is examined for 4 different healthy volunteers on three different force ranges: 2 N to 3 N, 2 N to 7.5 N, and 2 N to 12 N.

Figure 5-11 shows the percent absolute relative error as a function of the three force ranges. The results shown in the figure are raw results of the optimization and calibration has not been completed on this data. In the figure, 'S' and 'D' refer to systolic and diastolic pressure; '1' refers to force range 1, which is from 2 N to 3 N; '2' refers to force range 2, which is from 2 N to 7.5 N; '3' refers to force range 3, which is from 2 N to 12 N. As shown in the figure, of the three force ranges investigated, the 2 N to 3 N force range has the most accuracy; in fact, the results for the 2 N to 3 N force range are comparable to the raw results of the algorithm using the 8 N to 12 N force range as in Figure 5-1. The larger two force ranges have less desirable accuracy and precision numbers. Clearly, more data on different force ranges (e.g. from 3 N to 5 N) and on more volunteers would be helpful to fully understand the impact of force range on the accuracy of the technique.

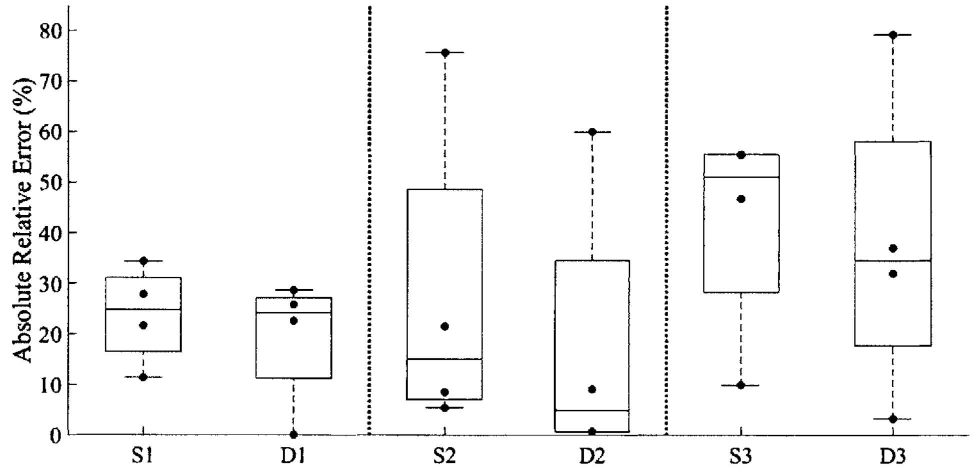

Figure 5-11: Absolute relative error corresponding to different force ranges. 'S' and 'D' refer to systolic and diastolic pressure. '1' refers to force range 1, which is from 2 N to 3 N. '2' refers to force range 2, which is from 2 N to 7.5 N. '3' refers to force range 3, which is from 2 N to 12 N. The results on four volunteers shown here are pre-calibration data.

The calibration set acquired in Section 5.3.2 was applied to this data set and the results are shown in Figure 5-12. It should be noted that the calibration used in this figure was calculated from data on the 8 N to 12 N force range; it is used here because only four volunteers were investigated with different force ranges. In the figure, it is again clear that the lowest force range, from 2 N to 3 N, has the lowest error of the three force ranges considered.

The applicability of the algorithm to lower force ranges might allow for future applications of the technique that are easier-to-use and cause less discomfort to volunteers.

5.7 Summary

In this chapter, results from healthy volunteers were displayed, including raw algorithm results and k-fold cross-validation results. The results suggest that the accuracy and precision of the blood pressure measurement technique in this dissertation for systolic pressure is -1.24 mmHg $\pm$ 10.04 mmHg and for diastolic pressure is -1.45 mmHg $\pm$

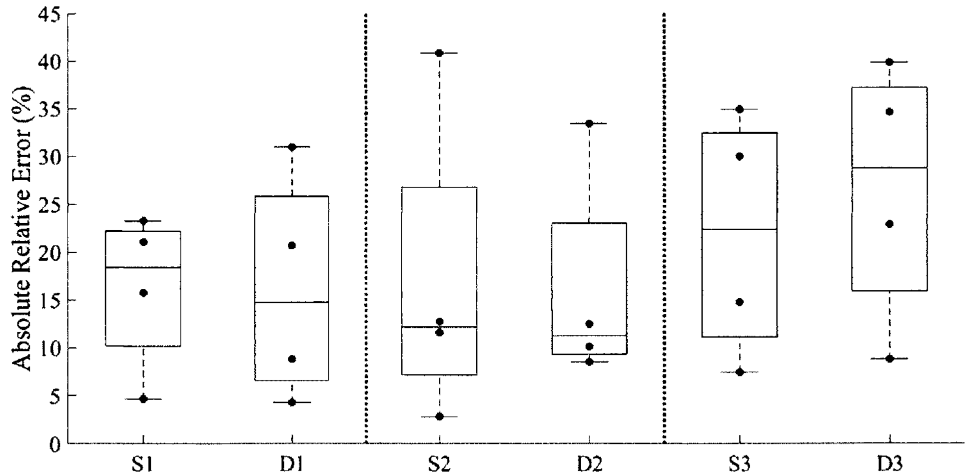

Figure 5-12: Absolute relative error corresponding to different force ranges. 'S' and 'D' refer to systolic and diastolic pressure. '1' refers to force range 1, which is from 2 N to 3 N. '2' refers to force range 2, which is from 2 N to 7.5 N. '3' refers to force range 3, which is from 2 N to 12 N. The results on four volunteers shown here are post-calibration data, where the calibration was found in Section 5.3.2.

4.75 mmHg. While these results are deemed sufficient for a proof-of-concept of the technique, it is important to recall that the technique is being compared to the error-prone oscillometric cuff. Further, this chapter displayed results using the real-time table look-up approach to the optimization, and using the computational model that includes the bone. It also analyzed the condition number, intraobserver repeatability, the affect of artery thickness on the accuracy of the technique, and the affect of chosen force range on the accuracy of the technique.

Chapter 6

Self-Scans on Healthy Volunteers

In this chapter, the novel blood pressure measurement technique is applied to nominally healthy volunteers who have completed self-scans on their own carotid artery. This contrasts with Chapter 5, in which healthy volunteers were recruited and the scans were completed by trained sonographers.

6.1 Data Acquisition Specifics

The Massachusetts Institute of Technology (MIT) IRB approved the following studies. Volunteers for the studies gave informed consent. Inclusion criteria included (a) being over 18 years of age and (b) non-pregnant mothers. Exclusion criteria included (a) volunteers with pacemakers and (b) overweight volunteers (BMI 30 $\frac{kg}{m^2}$ and greater).

The volunteer was first familiarized with the study, gave informed consent, and then received instruction on how to complete the force sweep process. The volunteer was shown the location of the carotid artery and informed about the three taps needed at the beginning of each force sweep. Further, volunteers were instructed to ensure that the artery only moved vertically in the image. After taking a blood pressure measurement using an oscillometric cuff (Premium Automatic Blood Pressure Monitor, CVS Health, Woonsocket, RI, USA), the seated volunteer proceeded to complete force sweeps on their own carotid artery while in view of the both the real-time ultrasound images and the real-time force data. The GE Logiq E9 ultrasound machine (General

Electric, Boston, MA, USA) and a GE 9L-D linear probe (General Electric, Boston, MA, USA) were used for data acquisition. During the scan, a study investigator read out-loud the forces from LabView so that the volunteer could focus on the ultrasound images. After the scans were completed, a final cuff measurement was taken.

Note that in the final application, force data could be conveyed to the user either using visual clues on the ultrasound machine or by using audio clues. The forces in this study were read out-loud to volunteers because of the difficulty in focusing on both the ultrasound images and laptop displaying force at the same time.

6.2 Variation of Cuff Measurements Over Minutes

In this section, the variations over time in the *oscillometric cuff* measurements are investigated. In the next section, this information will be compared to the performance of the novel technique over time.

6.2.1 Study Specifics

For these results, a volunteer took oscillometric cuff measurements every two minutes for 90 minutes. The systolic pressure, diastolic pressure, and pulse rate were recorded. During the test, the volunteer was instructed to sit on a chair and remain still. There were no distractions for the volunteer: no talking, changing of posture, or smartphone usage.

6.2.2 Results

The results of this study are displayed in Figure 6-1; in (a), the cuff pressure versus time is displayed and, in (b), the pulse per minute versus time is displayed. From (b), it is clear that the volunteer began to relax after the study began; the pulse rate levels off after approximately 40 minutes of rest. From start to finish, the cuff typically took 40-45 seconds to inflate, deflate, and display a reading. Calculated for the entire 90 minutes of data, the mean systolic and diastolic pressures reported by the cuff were,

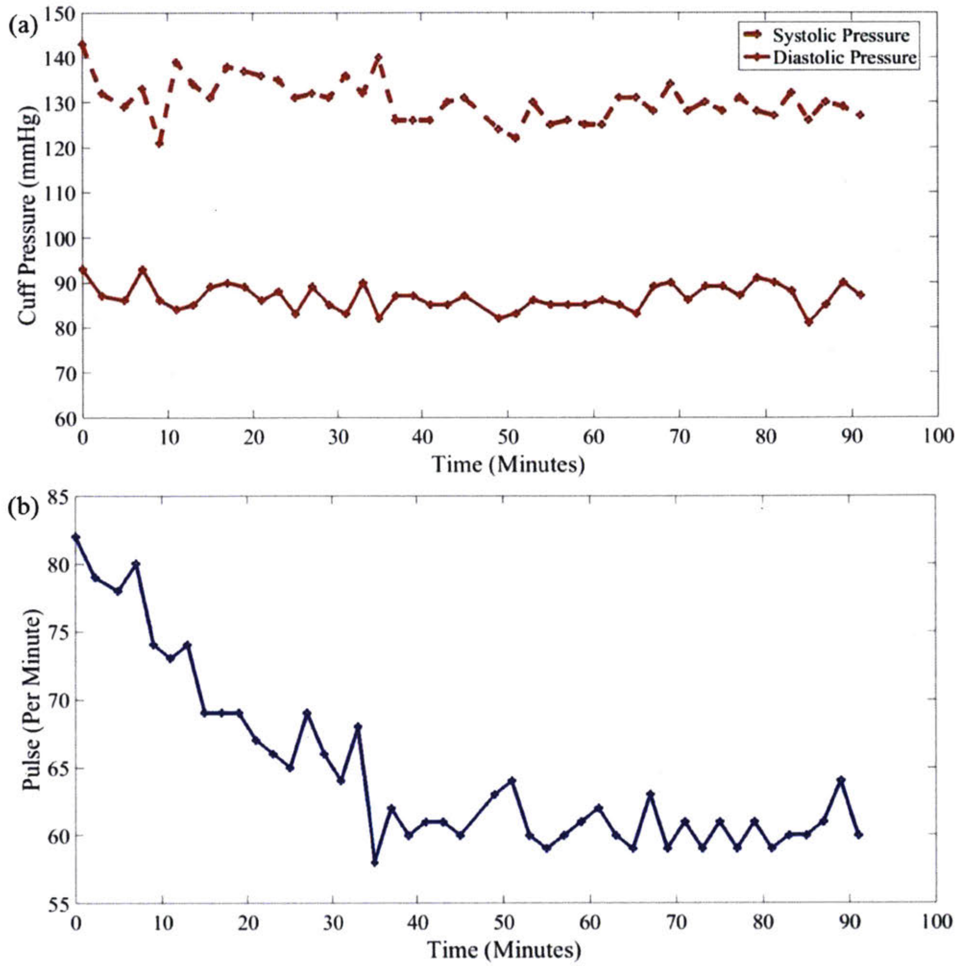

Figure 6-1: Cuff measurements versus time on a healthy volunteer. Measurements were taken once every two minutes for 90 minutes. In (a), systolic and diastolic pressures versus time are displayed. In (b), the pulse rate is displayed versus time.

respectively, 130.4 ± 4.7 mmHg and 86.7 ± 2.8 mmHg. However, calculated after levelling off at minute 40, the mean systolic and diastolic pressures reported by the cuff were, respectively, 128.16 ± 2.9 mmHg and 86.4 ± 2.7 mmHg. These standard deviations give information about the variation of the cuff measurements over the course of minutes in this idealized study.

6.2.3 Discussion

The results shown above indicate a small standard deviation for cuff measurements once the pulse rate reaches steady state. However, it should be noted that the volunteer above was very still and was not talking during the 90 minute data acquisition; these conditions are not typical of a doctor's office or other data acquisition environments.

6.3 Variation of Algorithm Measurements Over Minutes

6.3.1 Study Specifics

Two healthy volunteers were used in order to evaluate the variations of the algorithm over minutes, similar to the previous section which evaluated variations of the cuff over minutes. In the study, the ultrasound sweeps were self-administered and thus required more movement than the oscillometric cuff readings discussed in Section 6.2 above.

Healthy Volunteer 1

During the visit, an ultrasound sweep was completed once every three minutes for a total of 90 minutes. Every 9 minutes, an oscillometric cuff measurement was obtained; in order to do so, the cuff had to be placed on the arm and taken off after the measurement completed. Removing the cuff was important in order to facilitate the movement needed to complete a force sweep. However, removing the cuff resulted in more movement that might have increased variability in the algorithm measurements over time.

Healthy Volunteer 2

During the study, the volunteer took data over the course of 15 minutes. Cuff measurements were taken at the beginning and end of the study only. Algorithm measurements were taken throughout the 15 minutes.

6.3.2 Results

Healthy Volunteer 1

In Figure 6-2, the raw algorithm results from healthy volunteer 1 are shown with no k-fold cross-validation applied. In particular, the result quantities discussed in Section 5.2 are shown in (a)-(e) of the figure and, in part (f), the blood pressure readings for the algorithm and cuff are plotted versus minutes from the beginning of the study. Note that in order to generate (a)-(e), the cuff pressures were interpolated onto the times at which the algorithm was used to measure blood pressure; this interpolation allowed direct comparison between cuff measurements and algorithm measurements. From these plots, the mean and standard deviation of the algorithm measurements for systolic pressure are 109.40 mmHg and 9.11 mmHg, respectively, and for diastolic pressure are 79.50 mmHg and 8.16 mmHg, respectively. The mean and median of the absolute relative error for systolic pressure are 21.65 % and 20.13 %, respectively, and for diastolic pressure are 11.10 % and 11.42 %, respectively. The precision and accuracy for systolic pressure are -26.20 mmHg $\pm$ 8.45 mmHg and for diastolic pressure are -6.87 mmHg $\pm$ 7.90 mmHg.

The k-fold cross-validation algorithm is applied to the raw data discussed above and the results on the test set are displayed in Figure 6-3. The quantities plotted in (a)-(f) in this figure replicate those quantities displayed in Figure 6-2. When applied to the test set, the mean and standard deviation of the algorithm measurements for systolic pressure are 135.62 mmHg and 2.52 mmHg, respectively, and for diastolic pressure are 85.83 mmHg and 0.42 mmHg, respectively. The mean and median of the absolute relative error for systolic pressure are 1.97 % and 1.78 %, respectively, and for diastolic pressure are 2.32 % and 1.63 %, respectively. The precision and accuracy for systolic pressure are 0.23 mmHg $\pm$ 3.32 mmHg and for diastolic pressure are -1.30 mmHg $\pm$ 2.20 mmHg. As in Section 5.3.2, in order to be sure that the k-fold algorithm was not 'lucky' regarding random sorting, statistics for 2000 different random sortings are displayed in Table 6.1.

Finally, the k-fold cross-validation parameter set found above is applied to the full

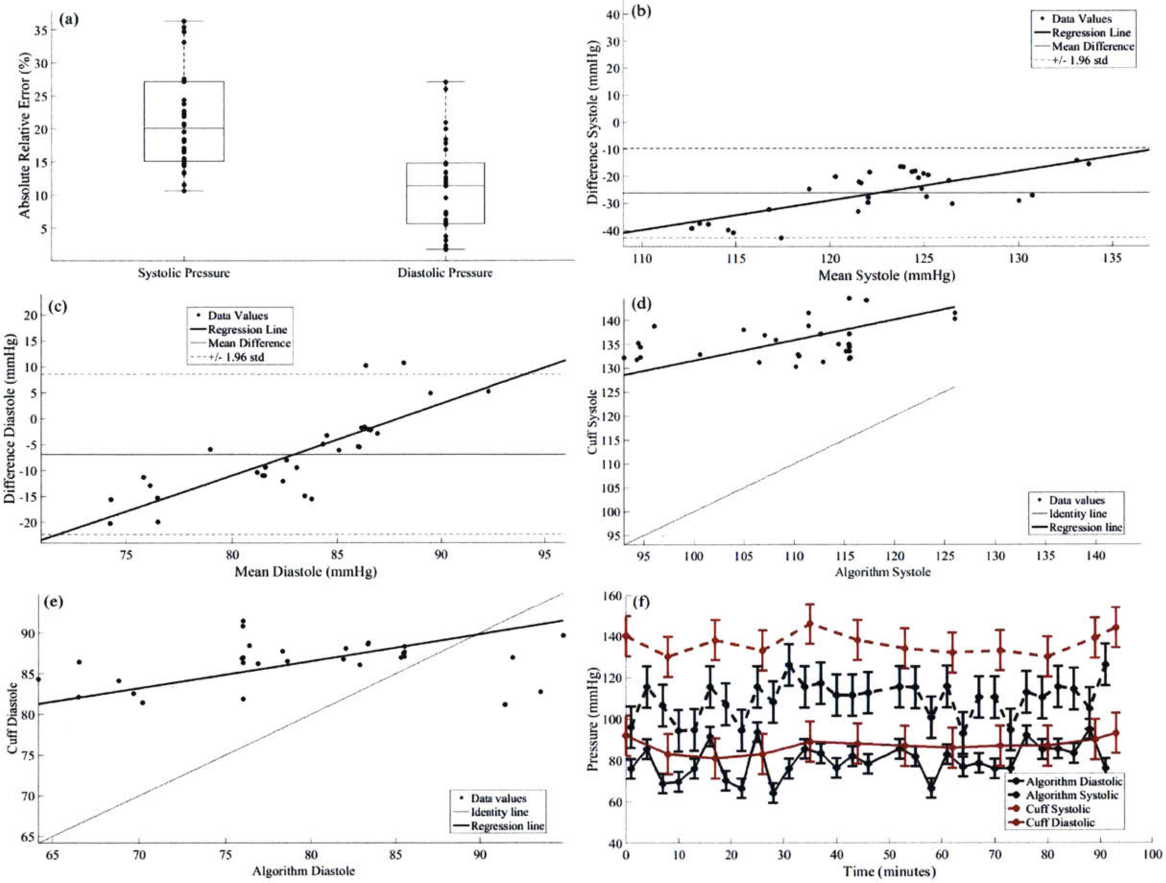

Figure 6-2: Results showing the variation of the algorithm measurements over a period of 90 minutes on healthy volunteer 1. The results presented here are raw algorithm results and did not undergo any post-processing cross-validation step. Part (a)-(e) show the quantities discussed in Section 5.2 and the plot in (f) shows the pressure versus minutes in the study.

data set and the results are displayed in Figure 6-4. The plots in this figure represent the same quantities as the previous two figures. For this figure, the mean and standard deviation of the algorithm measurements for systolic pressure are 135.65 mmHg and 2.10 mmHg, respectively, and for diastolic pressure are 85.75 mmHg and 0.77 mmHg, respectively. The mean and median of the absolute relative error for systolic pressure are 2.17 % and 2.12 %, respectively, and for diastolic pressure are 2.45 % and 2.27 %, respectively. The precision and accuracy for systolic pressure are 0.06 mmHg $\pm$ 3.67 mmHg and for diastolic pressure are -0.62 mmHg $\pm$ 2.62 mmHg.

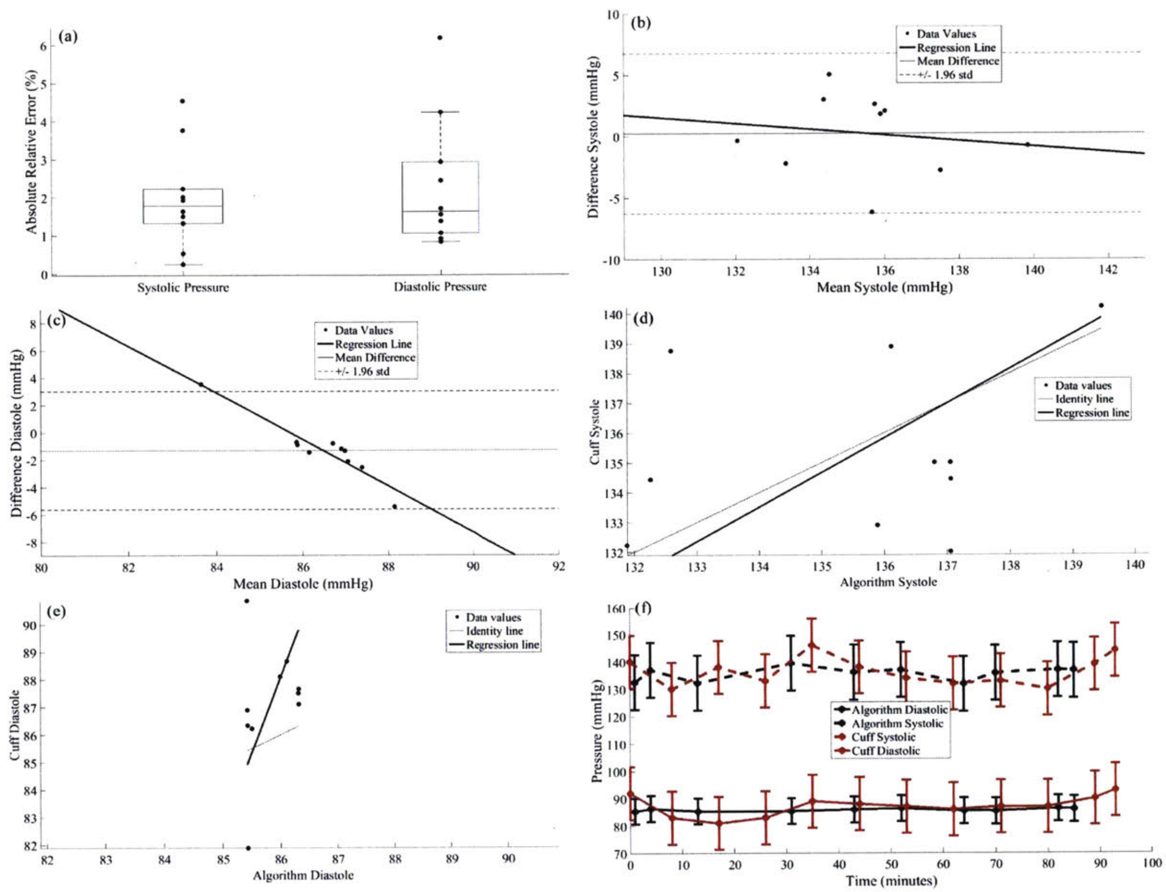

Figure 6-3: Results showing the variation of the algorithm measurements over a period of 90 minutes on healthy volunteer 1. The results presented here are algorithm results in which the k-fold cross-validation algorithm has been applied and the resulting parameter set is applied to the test set.

Healthy Volunteer 2

The raw algorithm results from healthy volunteer 2 are shown in Figure 6-5. For this figure, the mean and standard deviation of the algorithm measurements for systolic pressure are 104.65 mmHg and 9.30 mmHg, respectively, and for diastolic pressure are 74.50 mmHg and 8.29 mmHg, respectively. The mean and median of the absolute relative error for systolic pressure are 15.25 % and 15.51 %, respectively, and for diastolic pressure are 9.42 % and 7.10 %, respectively. The precision and accuracy for systolic pressure are -16.97 mmHg $\pm$ 11.50 mmHg and for diastolic pressure are 1.95 mmHg $\pm$ 8.43 mmHg.

The test set results after applying the k-fold cross-validation method to healthy

Table 6.1: Statistics obtained after running the k-fold cross-validation method for 2000 different random sortings into training set and test set. The table shows the results from healthy volunteer 1 who had measurements taken many times of a period of 90 minutes. In this table, α is a 2000 element vector where each element of the vector is the mean of the errors in a particular random sorting.

	Mean of α (mmHg)	Minimum of α (mmHg)	Maximum of α (mmHg)	Minimum of Test Set Errors (mmHg)	Maximum of Test Set Errors (mmHg)
Systolic	-0.04	-5.32	4.63	-10.97	7.06
Diastolic	0.06	-3.26	3.38	-6.69	8.84

volunteer 2 are shown in Figure 6-6. In this figure, the mean and standard deviation of the algorithm measurements for systolic pressure are 119.49 mmHg and 1.82 mmHg, respectively, and for diastolic pressure are 72.47 mmHg and 0.05 mmHg, respectively. The mean and median of the absolute relative error for systolic pressure are 5.26 % and 5.35 %, respectively, and for diastolic pressure are 0.53 % and 0.60 %, respectively. The precision and accuracy for systolic pressure are -6.45 mmHg $\pm$ 3.06 mmHg and for diastolic pressure are -0.39 mmHg $\pm$ 0.11 mmHg.

The k-fold cross validation parameters were applied to the full set from healthy volunteer 2 and the results are shown in Figure 6-7. For this figure, the mean and standard deviation of the algorithm measurements for systolic pressure are 119.20 mmHg and 1.99 mmHg, respectively, and for diastolic pressure are 72.43 mmHg and 0.08 mmHg, respectively. The mean and median of the absolute relative error for systolic pressure are 2.71 % and 2.04 %, respectively, and for diastolic pressure are 0.33 % and 0.36 %, respectively. The precision and accuracy for systolic pressure are -2.42 mmHg $\pm$ 3.98 mmHg and for diastolic pressure are -0.12 mmHg $\pm$ 0.28 mmHg.

6.3.3 Discussion

The results above indicate that the self-scan algorithm results have a lower standard deviation (2.52 mmHg and 0.42 mmHg for healthy volunteer 1 systolic and diastolic pressures) than for the cuff measurements (4.7 mmHg and 2.8 mmHg for systolic and diastolic pressure). Note that it is assumed that the results on the test set most accurately represent the algorithm performance. The lower standard deviation is in

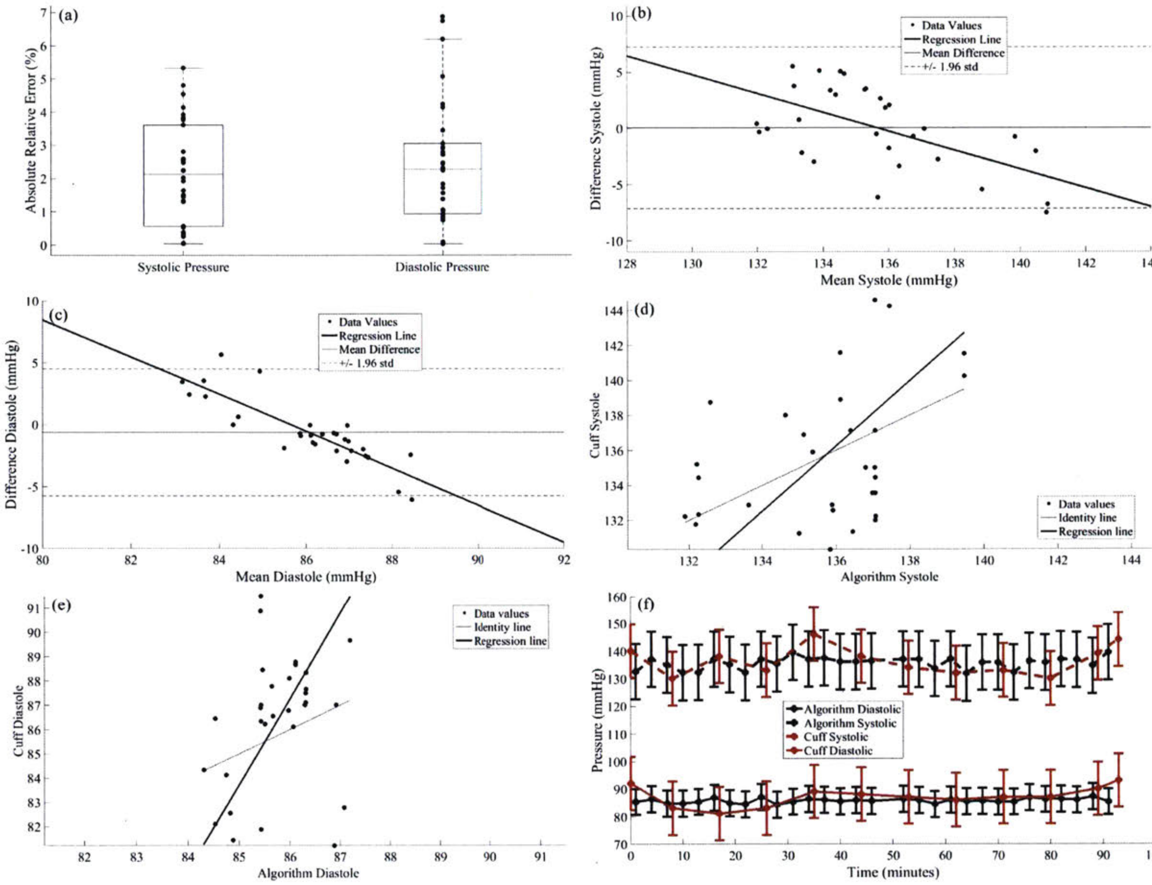

Figure 6-4: Results showing the variation of the algorithm measurements over a period of 90 minutes on healthy volunteer 1. The results presented here are algorithm results in which the k-fold cross-validation algorithm has been applied and the resulting parameter set is applied to the full set.

spite of the fact that the algorithm measurements require more movement than the cuff measurements.

It is notable that the diastolic pressure in the raw algorithm results agree more closely with the cuff than the corresponding systolic pressure results. This is an interesting phenomenon because, as specified in Section 1.1, the diastolic pressure varies much less throughout the arterial tree than systolic pressure; systolic pressure is also known to be greater in the brachial artery than in the carotid. Again, this is exactly what is displayed in the raw algorithm results.

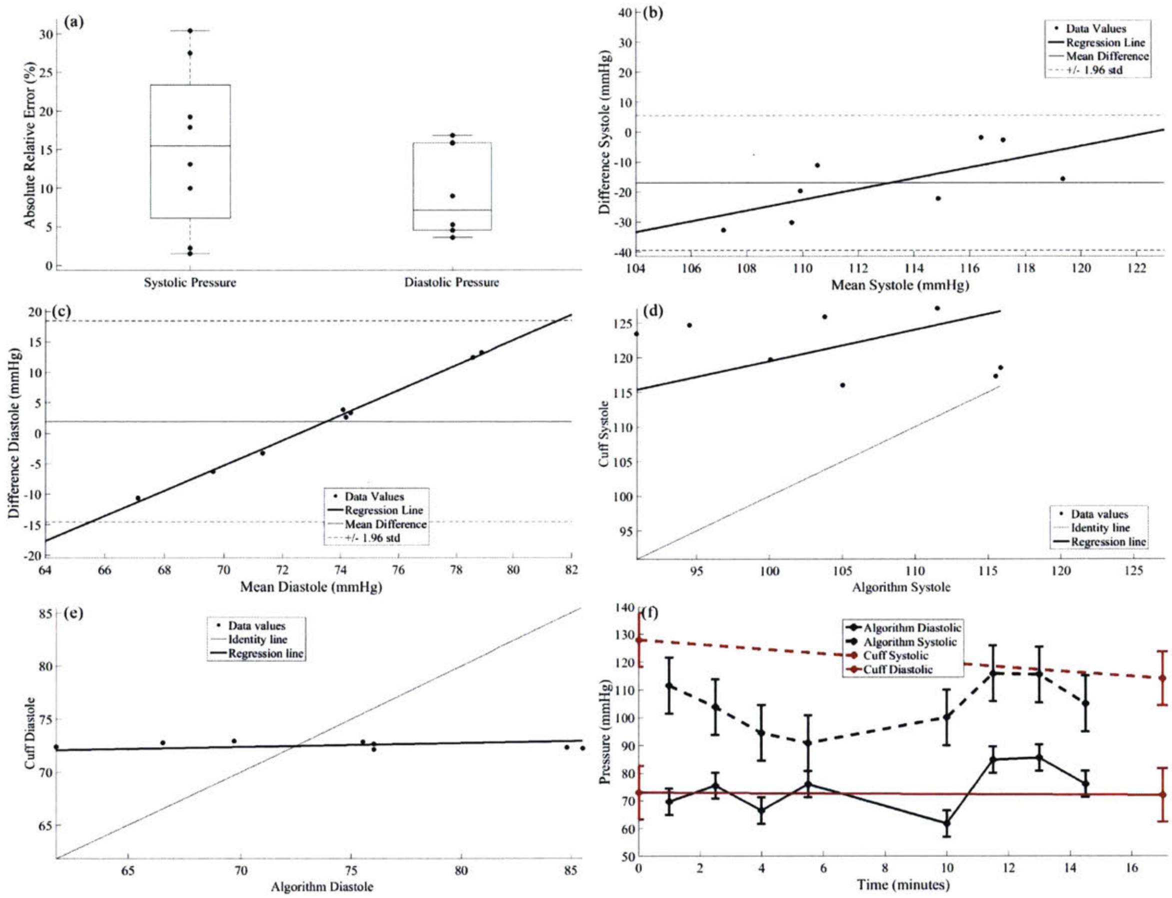

Figure 6-5: Results showing the variation of the algorithm measurements over a period of minutes on healthy volunteer 2. The results presented here are raw algorithm results and did not undergo any post-processing cross-validation step. Outliers were excluded from the plots.

6.4 Variation of Cuff and Algorithm Over Days

6.4.1 Study Specifics

The two volunteers from Section 6.3 also completed a longitudinal study over 14 days. They repeatedly completed self-scans on the carotid artery using the protocol described in Section 6.1. During each visit, an oscillometric cuff measurement was first taken, the ultrasound force sweeps were taken, then a final oscillometric cuff measurement was completed. The purpose of this study was to evaluate if the algorithm measurements tracked the cuff measurements consistently over time.

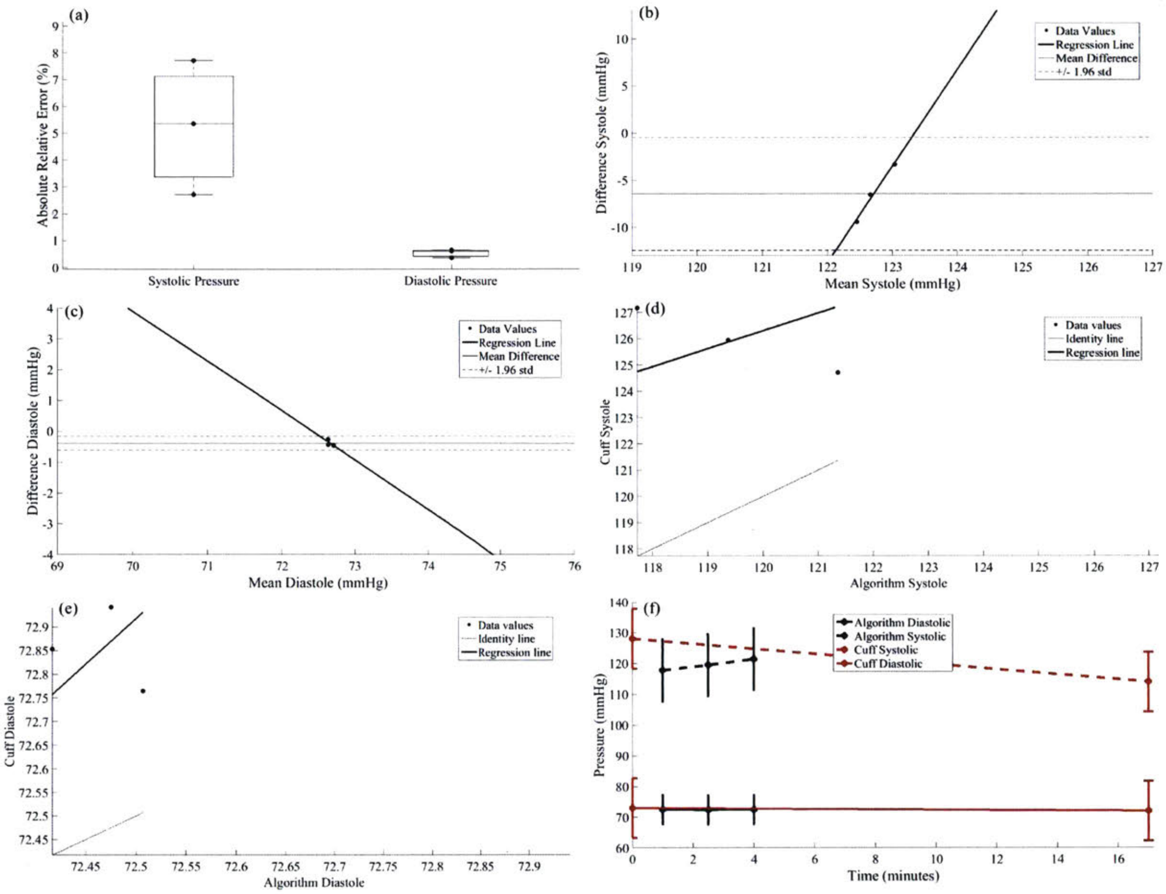

Figure 6-6: Results showing the variation of the algorithm measurements over a period of minutes on healthy volunteer 2. The results presented here are algorithm results in which the k-fold cross-validation algorithm has been applied and the resulting parameter set is applied to the test set. Outliers were excluded from the plots.

6.4.2 Results

Healthy Volunteer 1

In Figure 6-8, the raw algorithm results for healthy volunteer 1 are shown without any post-processing cross-validation performed. Parts (a)-(e) of the figure plot the quantities specified in Section 5.2 while the plot in (f) of the figure is pressure versus data acquisition day. The mean and median of the absolute relative error in these plots are 16.88 % and 16.40 %, respectively, for systolic pressure and 9.15 % and 7.80 %, respectively, for diastolic pressure. The accuracy and precision displayed in the figure are -19.20 mmHg ± 12.62 mmHg for systolic pressure and -1.46 mmHg ± 9.54 mmHg for diastolic pressure.

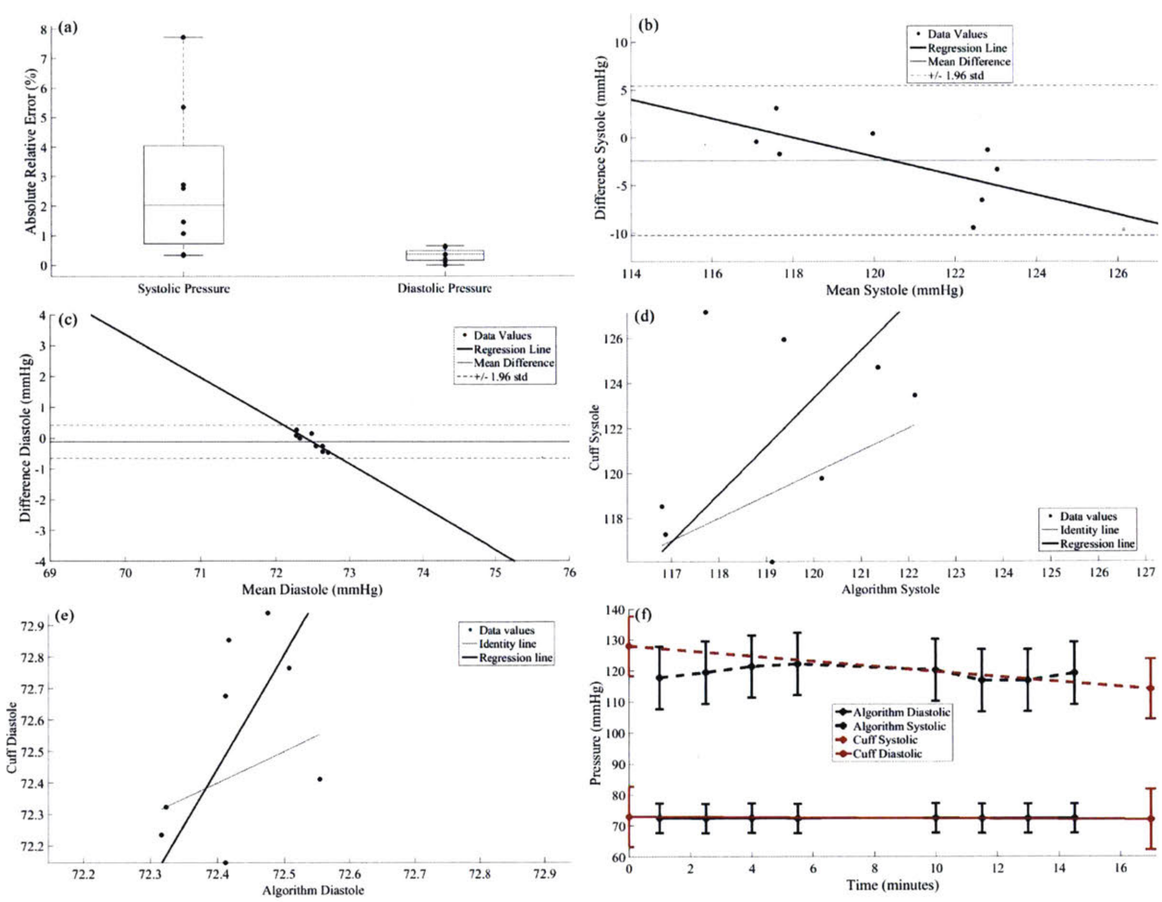

Figure 6-7: Results showing the variation of the algorithm measurements over a period of minutes on healthy volunteer 2. The results presented here are algorithm results in which the k-fold cross-validation algorithm has been applied and the resulting parameter set is applied to the full set. Outliers were excluded from the plots.

In Figure 6-9, the k-fold cross-validation parameter set from healthy volunteer 1 in Section 6.3.2 is applied and the result is shown on the full set. Note that this amounts to a patient-specific calibration because healthy volunteer 1 in this section is the same person as healthy volunteer 1 in Section 6.3.2. In (a)-(f), the quantities plotted are similar to those plotted in previous figures in this chapter. The mean and median of the absolute relative error in these plots are 7.62 % and 7.10 %, respectively, for systolic pressure and 6.51 % and 7.08 %, respectively, for diastolic pressure. The accuracy and precision displayed in the figure are 9.12 mmHg ± 7.34 mmHg for systolic pressure and 4.91 mmHg ± 5.10 mmHg for diastolic pressure.

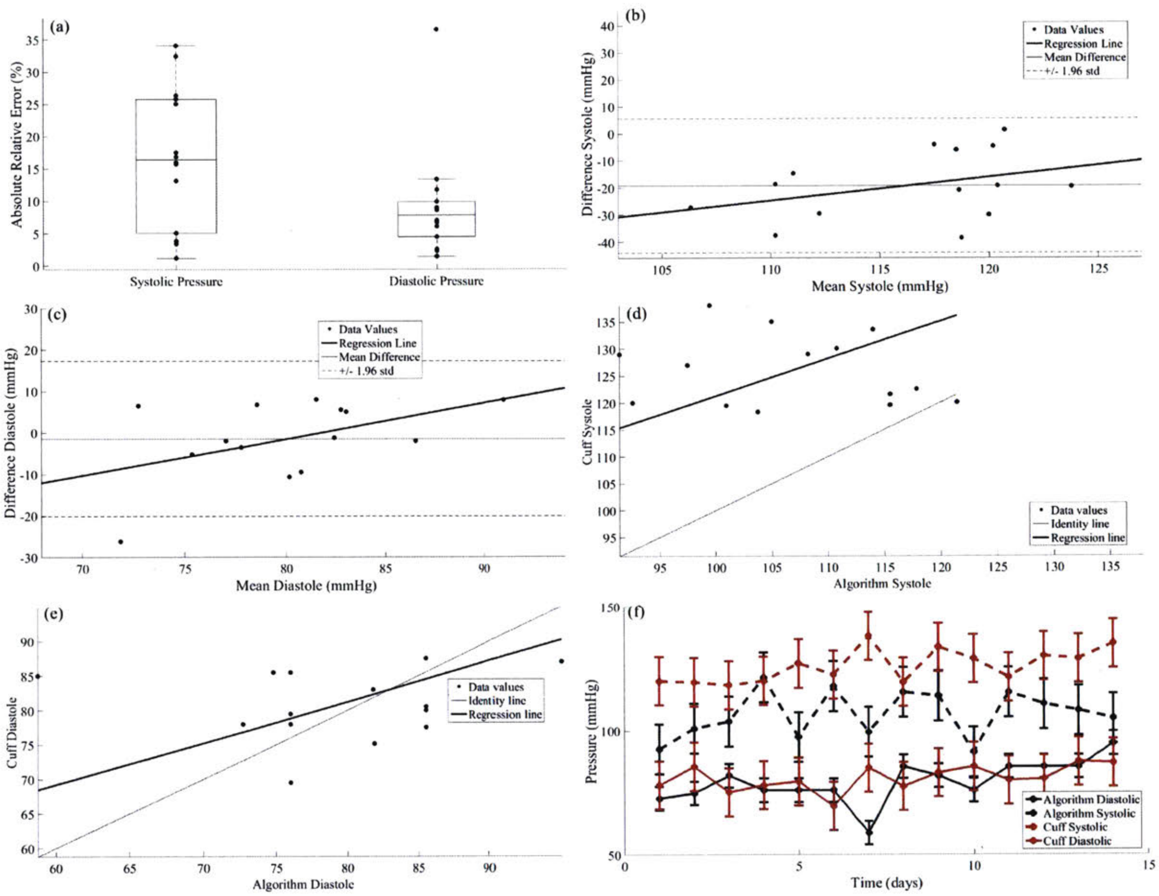

Figure 6-8: The algorithm was applied to healthy volunteer 1 over 14 non-consecutive days. The figure shows the raw results of the algorithm before cross-validation. Part (a)-(e) show the quantities discussed in Section 5.2 and the plot in (f) shows the pressure versus day number.

Healthy Volunteer 2

The raw algorithm results from the second healthy volunteer are shown in Figure 6-10. From the results in the figure, the mean and median of the absolute relative error in these plots are 20.28 % and 19.35 %, respectively, for systolic pressure and 10.46 % and 8.68 %, respectively, for diastolic pressure. The accuracy and precision displayed in the figure are -22.31 mmHg ± 9.91 mmHg for systolic pressure and -6.83 mmHg ± 6.67 mmHg for diastolic pressure.

The k-fold cross validation parameter set from healthy volunteer 2 in Section 6.3.2 is then applied and results on the full set are shown in Figure 6-11. Note again that this amounts to a patient-specific calibration. From the results in the figure, the

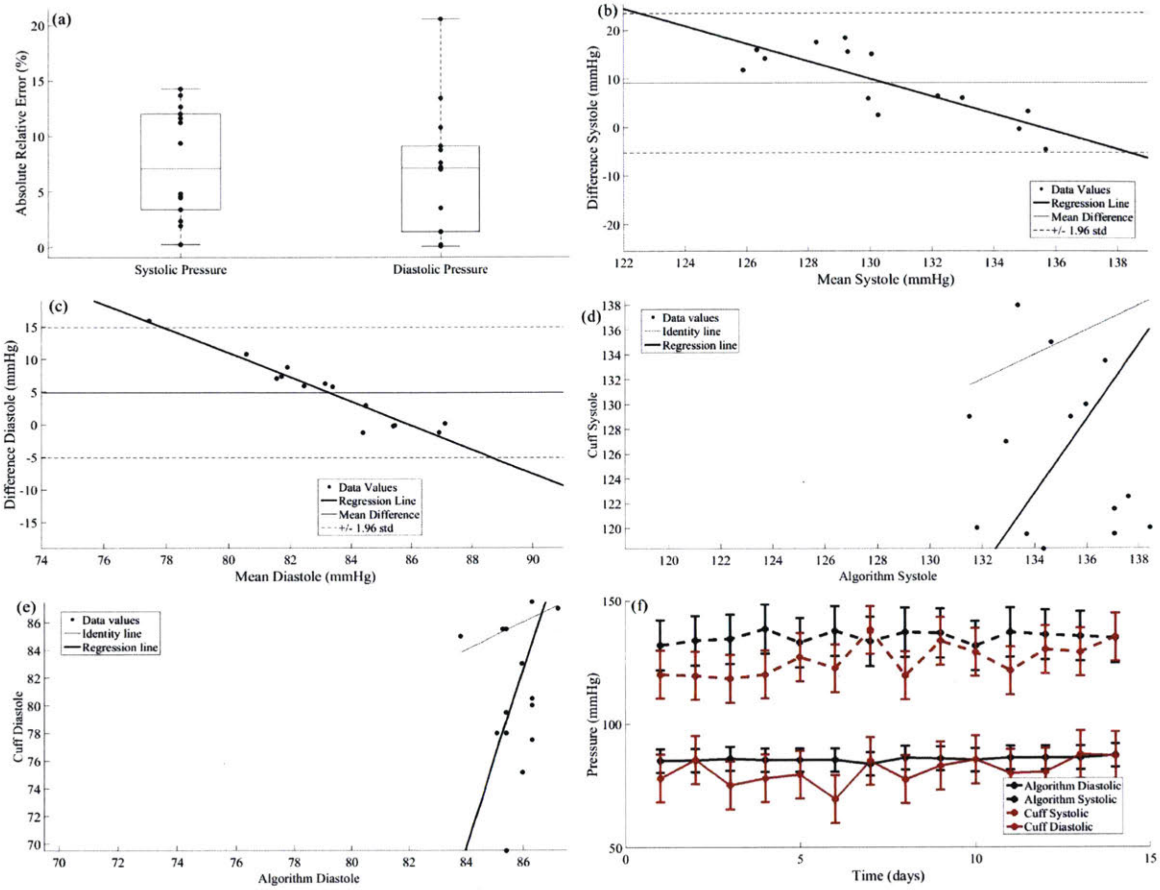

Figure 6-9: The algorithm applied to healthy volunteer 1 over 14 non-consecutive days. The results displayed here show the results after the k-fold cross-validation parameter set from healthy volunteer 1 in Section 6.3 (same volunteer as in this figure) was applied to the full set. Part (a)-(e) show the quantities discussed in Section 5.2 and the plot in (f) shows the pressure versus day number.

mean and median of the absolute relative error in these plots are 4.20 % and 4.09 %, respectively, for systolic pressure and 7.25 % and 4.70 %, respectively, for diastolic pressure. The accuracy and precision displayed in the figure are -1.89 mmHg ± 5.54 mmHg for systolic pressure and -5.16 mmHg ± 4.49 mmHg for diastolic pressure.

6.4.3 Discussion

In Figure 6-8 and Figure 6-10, the raw algorithm systolic pressure results agree less with the cuff than the raw algorithm diastolic pressure results (this phenomenon was first identified and discussed in Section 6.3.3). The k-fold cross-validation results above

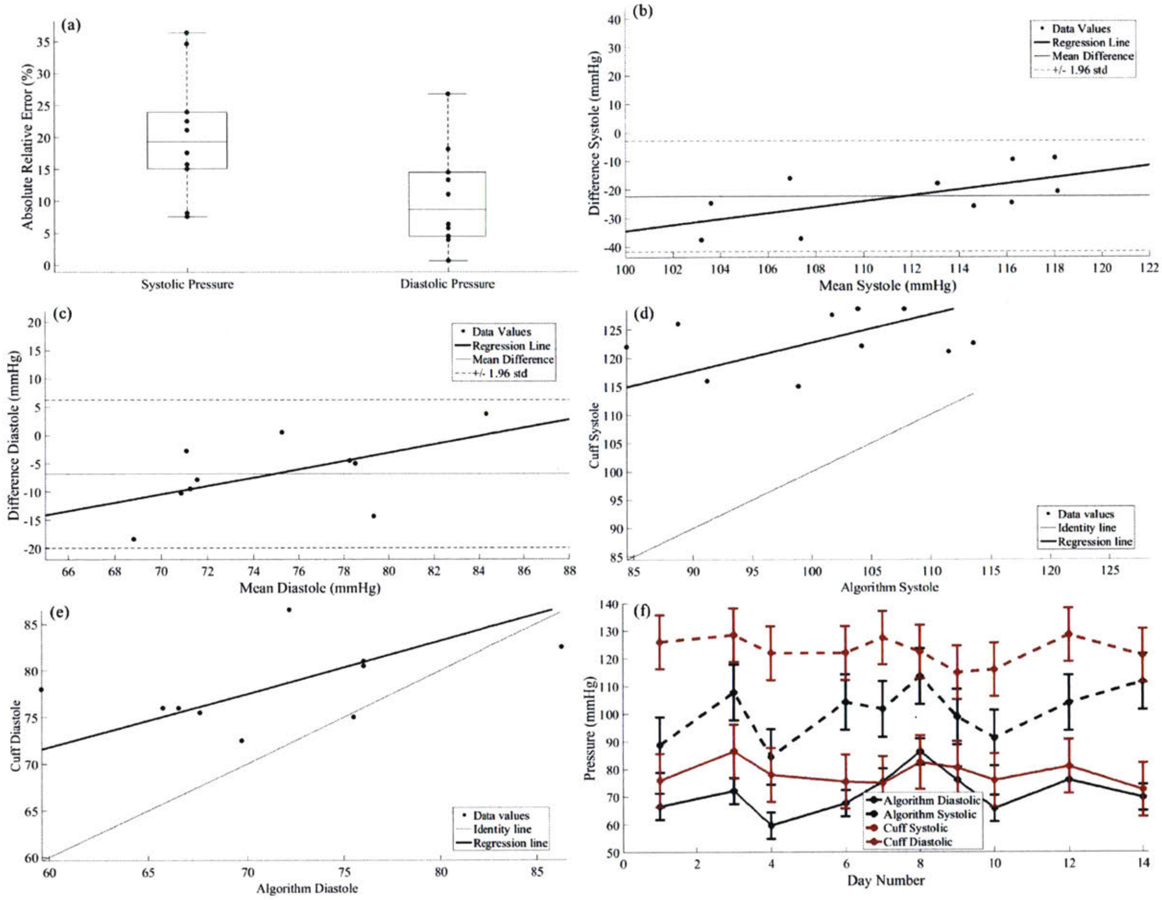

Figure 6-10: The algorithm was applied to healthy volunteer 2 over 14 non-consecutive days. The figure shows the raw results of the algorithm before cross-validation. Part (a)-(e) show the quantities discussed in Section 5.2 and the plot in (f) shows the pressure versus day number. Outliers were excluded from the plots.

show that the k-fold parameter set imparts significant smoothing to the algorithm results over time. The smoothing is due to a high y-intercept and low slope in the calculated calibration parameter set. This smoothing is likely due to the fact that the raw algorithm results in Figure 6-2 and Figure 6-5 show a lot of variability about the cuff measurements; the cross-validation algorithm finds the parameters that give the lowest error in the Kth fold (as described in Section 3.4.1), so it makes intuitive sense that there will be smoothing from the results in order to minimize error between the cuff and the algorithm. At the same time, volunteers for this study were relaxed during data acquisition and, thus, little variation in blood pressure is expected from these volunteers. Still, this consequence of the k-fold cross validation algorithm is one

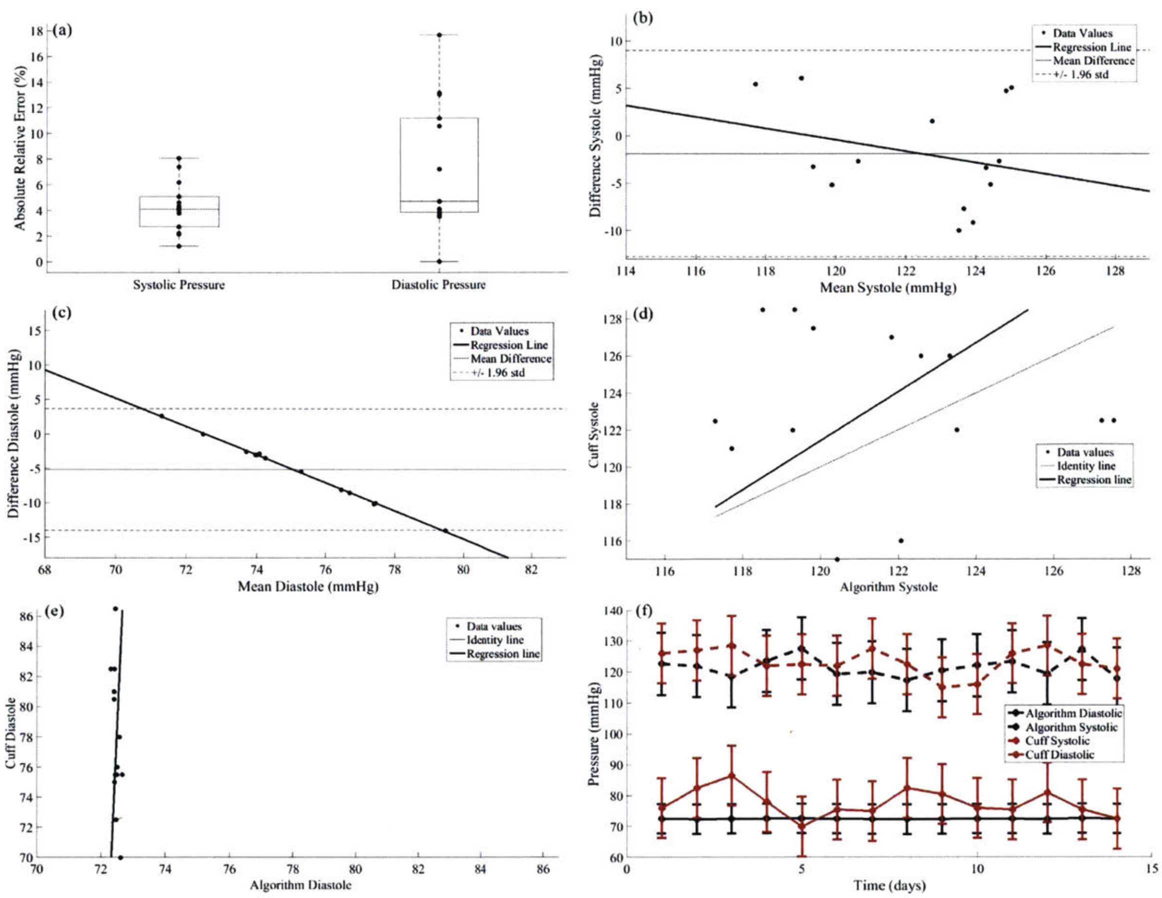

Figure 6-11: The algorithm applied to healthy volunteer 2 over 14 non-consecutive days. The results displayed here show the results after the k-fold cross-validation parameter set from healthy volunteer 2 in Section 6.3 (same volunteer as in this figure) was applied to the full set. Part (a)-(e) show the quantities discussed in Section 5.2 and the plot in (f) shows the pressure versus day number.

important factor that could be addressed by improving the calibration method.

The accuracy and precision numbers given above are excellent and represent a validation of the method over the period of days. In fact, the precision displayed above is less than that reported for the cuff compared to the invasive catheter (9.7 mmHg, see Chapter 1). All trend line data shows that the algorithm measurements are within the error bars of the cuff measurements.

6.5 Volunteers With Artificially Elevated Blood Pressure Due to Caffeine Intake

6.5.1 Study Specifics

In this study, the volunteer first completes the protocol in Section 6.1. Then, the volunteer takes caffeine. Each volunteer was given a choice of their preferred caffeine source. A typical 'dose' of caffeine for this study consisted of either a cup of coffee or a five-hour energy drink (Innovation Ventures LLC, Farmington Hills, MI, USA). After waiting at least 10 minutes after taking caffeine, the protocol in Section 6.1 is repeated. In this study, we investigate whether the direction of blood pressure changes due to caffeine as predicted by the algorithm agree with the blood pressure changes as predicted by the cuff.

6.5.2 Results

Results are shown in Figure 6-12, where the change in a pressure measurement (post-caffeine measurement minus pre-caffeine measurement) is plotted against the volunteer number. For each volunteer, the changes in a pressure measurement (in mmHg) is plotted for algorithm systolic and diastolic pressures and for cuff systolic and diastolic pressures. The purpose of the plot is to show how the cuff measurements change due to caffeine and, similarly, how the algorithm measurements change due to caffeine. The results presented in the figure are raw algorithm results.

In Figure 6-13, the k-fold cross-validation parameter set from healthy volunteer 1 in Section 6.4.2 is applied to the raw data set. The figure is again plotting pressure changes due to caffeine.

6.5.3 Discussion

In the caffeine results shown above, all pressure changes, except those from volunteer 1, were within the standard deviation expected from the cuff; recall from Section 1.3.3 that the standard deviation in the cuff measurement is approximately 9.7 mmHg

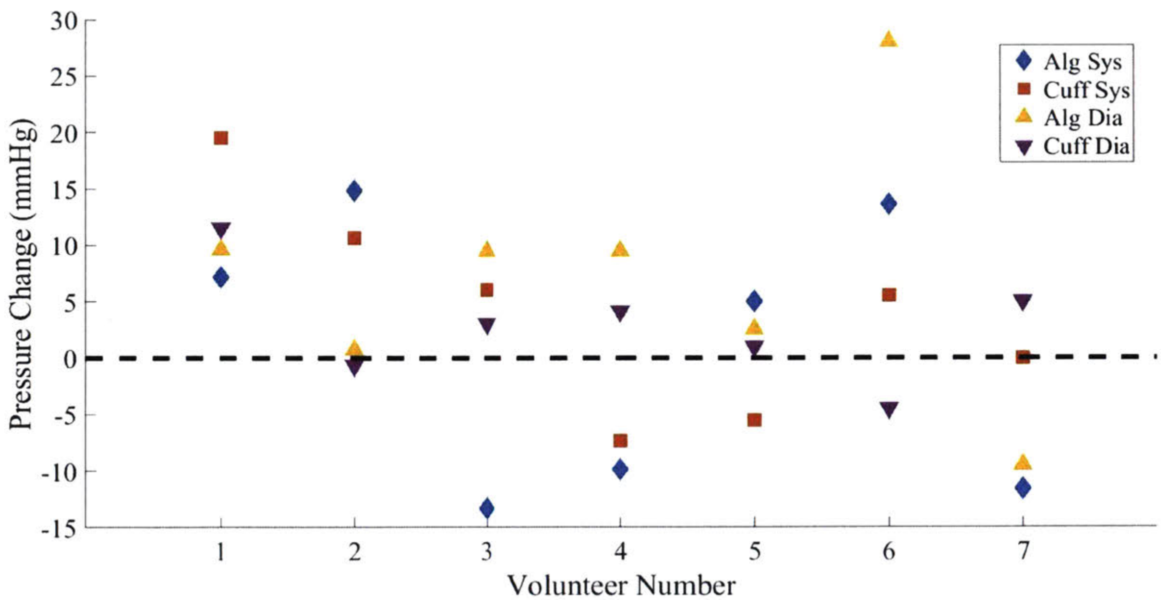

Figure 6-12: Post-caffeine measurement minus pre-caffeine measurement for seven volunteers. Changes are displayed for algorithm systolic and diastolic pressures as well as oscillometric cuff systolic and diastolic pressure. The algorithm results shown are the raw algorithm results.

compared to the invasive catheter. Furthermore, the literature states that caffeinated beverages only slightly change systolic and diastolic pressure [92]; in that paper, peripheral diastolic pressure and central systolic pressure both experienced statistically significant increases of approximately 4 mmHg between the baseline and 30 minutes after caffeine consumption. This change is well within the standard deviation of the cuff and is in line with the data that is displayed above. However, note that the study in the literature waited 30 minutes to take a measurement while the study in this dissertation waited only 10 minutes. It is possible that the aberrant data in volunteer 1 is due to variations in the cuff as described in Section 1.3.3. During testing, multiple cuff measurements should have been made in order to be sure of the reported cuff values. In summary, the caffeine results are inconclusive based on the inaccuracy of the cuff and the study design.

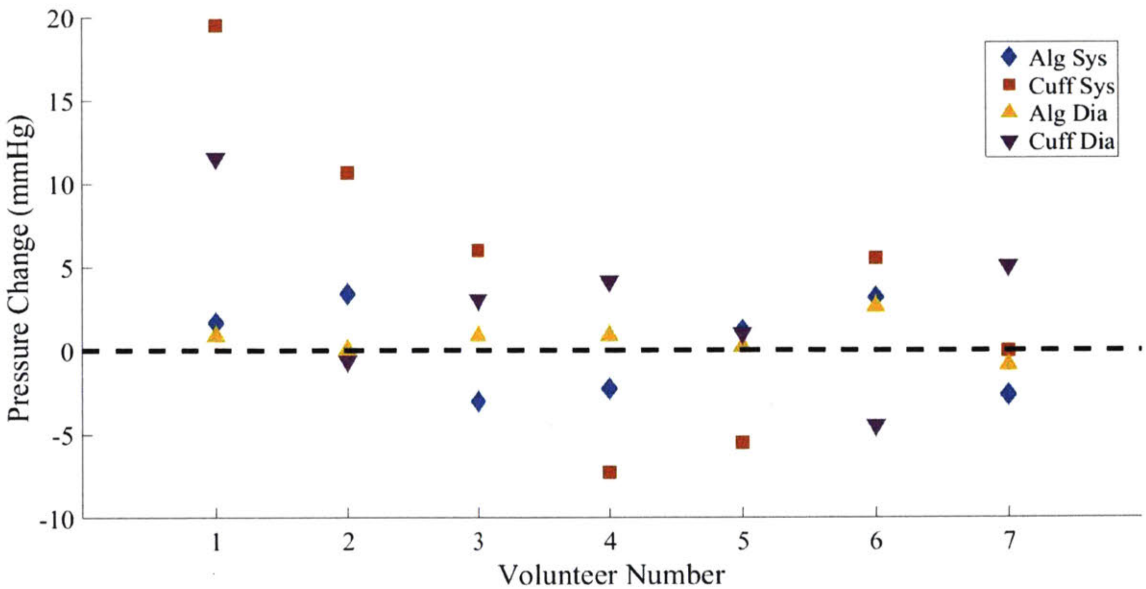

Figure 6-13: Post-caffeine measurement minus pre-caffeine measurement for seven volunteers. Changes are displayed for algorithm systolic and diastolic pressures as well as oscillometric cuff systolic and diastolic pressure. The algorithm results are shown after the k-fold cross-validation parameter set from healthy volunteer 1 in Section 6.4.2 is applied.

6.6 Volunteers With Artificially Elevated Blood Pressure Due to Exercise

6.6.1 Changes in Blood Pressure: Pre-Exercise to 10 Minutes Post-Exercise

Study Specifics

In this study, the protocol in Section 6.1 was first completed, then each volunteer completed their choice of exercise in order to elevate blood pressure. The volunteer was instructed to only exercise to a comfortable level and not to exhaustion. A typical exercise session consisted of either a short 5-10 minute jog or exercises including squats, wall-sits and push-ups. Finally, shortly after the exercises concluded, the protocol in Section 6.1 was completed again.

In this study, we investigate whether the blood pressure measurement trends predicted by the algorithm agree with those given by the cuff when a volunteer is instructed to complete aerobic exercise. In the study in this section, the protocol ended less than 10 minutes after exercise concluded. In the next section, longer-term changes in pressure due to exercise are examined (e.g. up to 45 minutes after exercise).

Results

Raw algorithm results are shown in Figure 6-14, where the data plotted is similar to that plotted in Figure 6-12 except that the focus is now blood pressure changes due to exercise. From the plot, it is clear that the systolic pressure reported by the cuff increased significantly for all patients while the systolic pressure reported by the algorithm did not undergo such a consistent, drastic change.

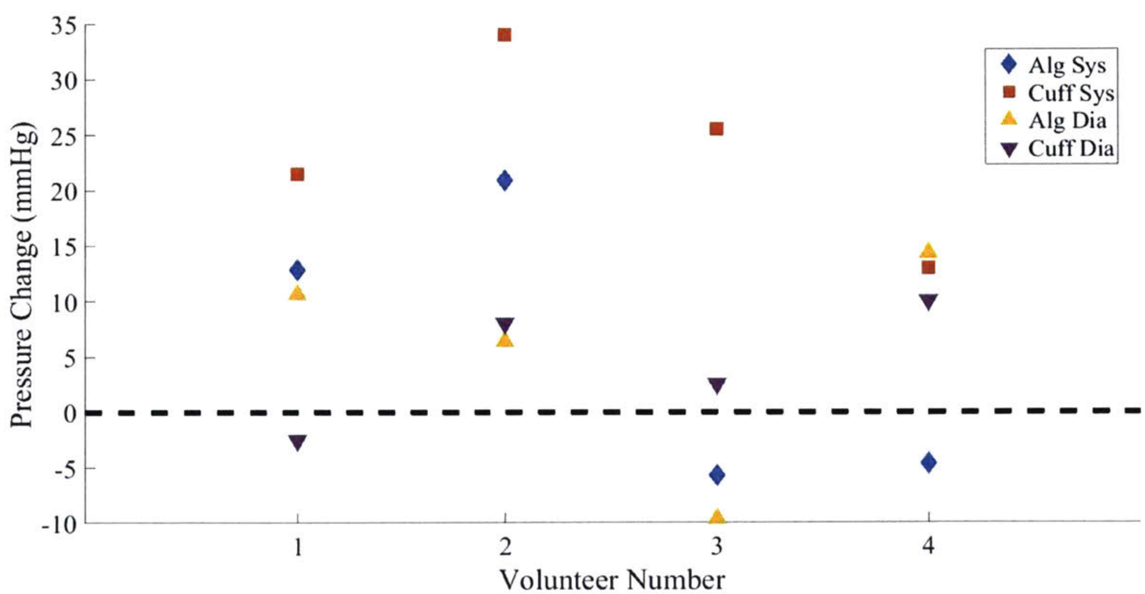

Figure 6-14: Post-exercise measurement minus pre-exercise measurement for four volunteers. Changes are displayed for algorithm systolic and diastolic pressures as well as oscillometric cuff systolic and diastolic pressure. The algorithm results shown are the raw algorithm results.

The k-fold cross-validation parameter set from healthy volunteer 1 in Section 6.4.2 was applied to this exercise data set and the result is shown in Figure 6-15. As previous trend-line plots indicated and as discussed in previous sections, the k-fold parameter set calibration serves to smooth algorithm results over time. This characteristic is also present in the results displayed in Figure 6-15; the changes in blood pressure reported by the algorithm are indeed smoothed over time compared to the cuff in these exercise results.

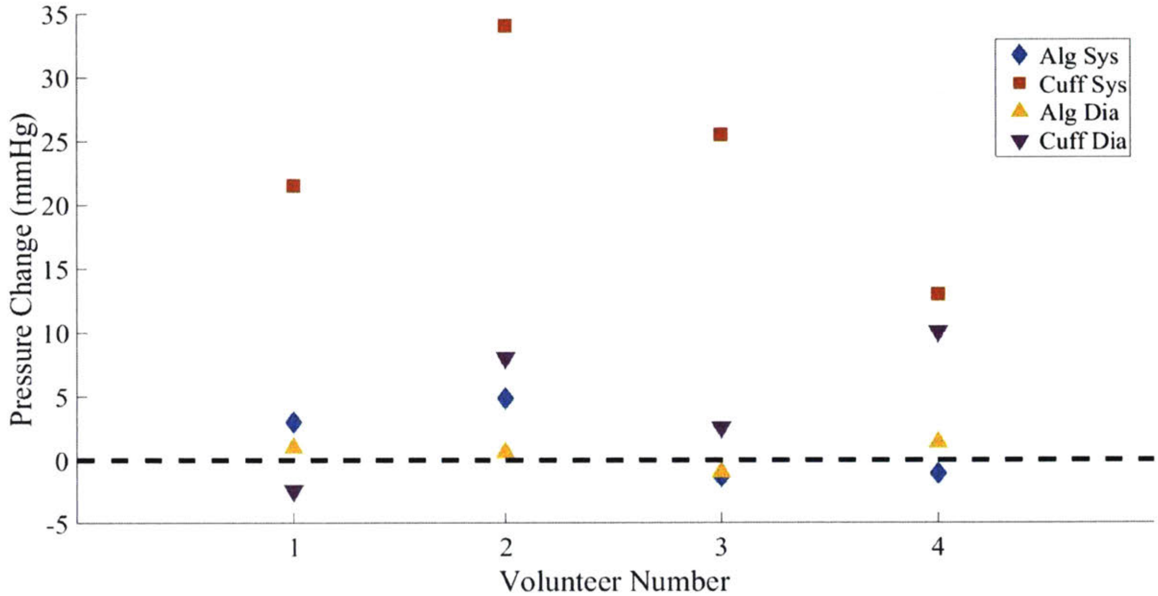

Figure 6-15: Post-exercise measurement minus pre-exercise measurement for four volunteers. Changes are displayed for algorithm systolic and diastolic pressures as well as oscillometric cuff systolic and diastolic pressure. The algorithm results are shown after the k-fold cross-validation parameter set from healthy volunteer 1 in Section 6.4.2 is applied.

Discussion

In the exercise results above, it appears that the brachial artery systolic pressure is reported to be highly elevated due to exercise but the carotid artery systolic pressure does not undergo such consistent, drastic changes. As seen in previous plots in this chapter, the k-fold cross-validation parameter set seems to smooth out large variations in the algorithm reported blood pressure; this is also the case in the results presented above.

The discrepancies between the algorithm changes and the cuff changes can be explained based on observations in the literature. In [93], a study of central blood pressure was completed such that pressure was measured before exercise, at peak exercise, at 5 minutes after exercise, and at 10 minutes intervals thereafter. It was reported that central diastolic pressure at the 5 minute mark was less than the control while the central systolic pressure at the 15 minute mark became less than the control. However, in this study in the literature, the subjects were requested to achieve maximal effort during exercise, which was not the case in the study in this dissertation.

In [94], systolic brachial pressure first drastically increased at the 1 to 3 minute mark after exercise then reached the baseline after 15 minutes. In that paper, diastolic brachial pressure had decreased slightly after 1 to 3 minutes post-exercise and was slightly increased from the baseline at the 15 minute mark.

Based on this information from the literature, it is possible that the discrepancies in the results above are due to the timing difference between cuff measurements and force sweeps. That is, the cuff systolic pressure changes are much higher than the algorithm changes because one cuff measurement occurred closer to the end of the exercise session than the force sweeps. After the cuff measurement was taken, the blood pressure decreases and the force sweeps were then taken. The decrease occurs quickly, as reported in the literature, and is evident in the results reported in Figure 6-14 above.

6.6.2 Changes in Blood Pressure: Pre-Exercise to 45 Minutes Post-Exercise

Study Specifics

In this study, one nominally-healthy volunteer completed a similar protocol as in Section 6.6.1. In Section 6.6.1, data was not gathered longer than 10 minutes after exercise ended. In this section, blood pressure changes are tracked with the cuff and algorithm for more than 15 *pre*-exercise minutes and 45 *post*-exercise minutes; this protocol allows for better evaluation of the algorithm over time. For this volunteer, the exercise consisted of a 30 minute jog.

Results

The results in Figure 6-16 show the raw algorithm measurements and cuff measurements before any calibration was completed. In this plot, error bars on the cuff measurements indicate the 9.7 mmHg standard deviation of the oscillometric cuff (see Section 1.3.3) and error bars on the algorithm measurements indicate the precision as discussed in Section 5.3.3. Note that, as shown in the figure, exercise occurred between minute 18 and minute 48.

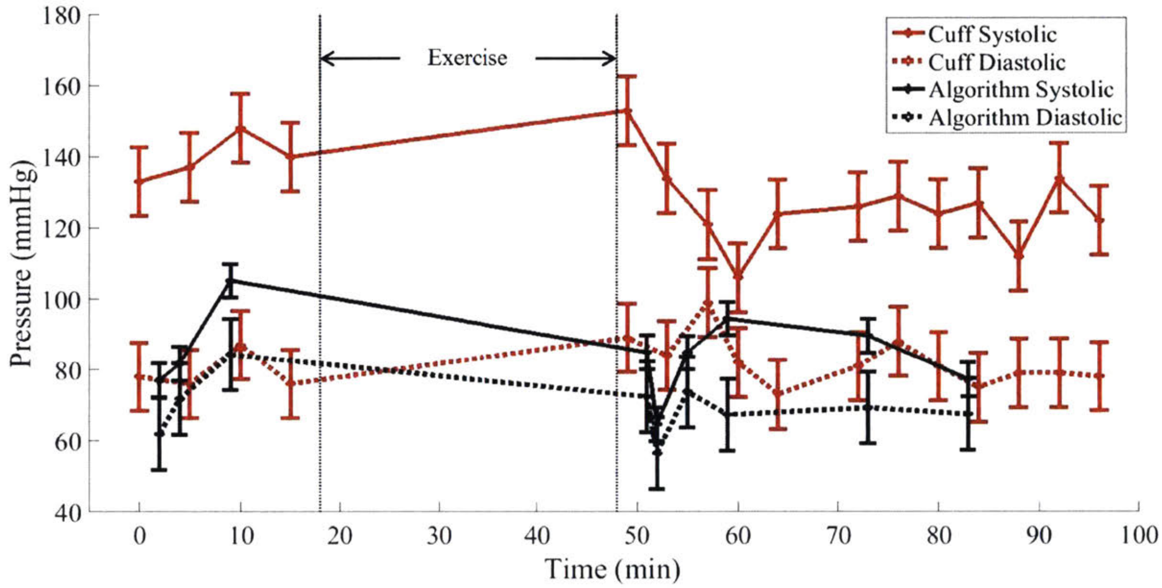

Figure 6-16: Results on a healthy volunteer both before and after exercise. The results shown here are raw results of the optimization before any calibration took place.

The calibration found from healthy volunteer 1 in Section 6.3.2 has been applied to this raw exercise data and the result is shown in Figure 6-17.

Discussion

Before analyzing the plots, it is important to understand what to expect both before and after exercise. It is expected that the blood pressure is stable before exercise begins. After exercise concludes, it is expected that the blood pressure is initially highly elevated; however, the blood pressure will then decrease from the maximum. In fact, the blood pressure is expected to decrease so much that it will be below the baseline. After going below the baseline, the blood pressure gradually recovers and eventually reaches steady state again.

From the raw data plot in Figure 6-16, it is clear that the blood pressure readings from both the cuff and algorithm first increase slightly before exercise occurred. If

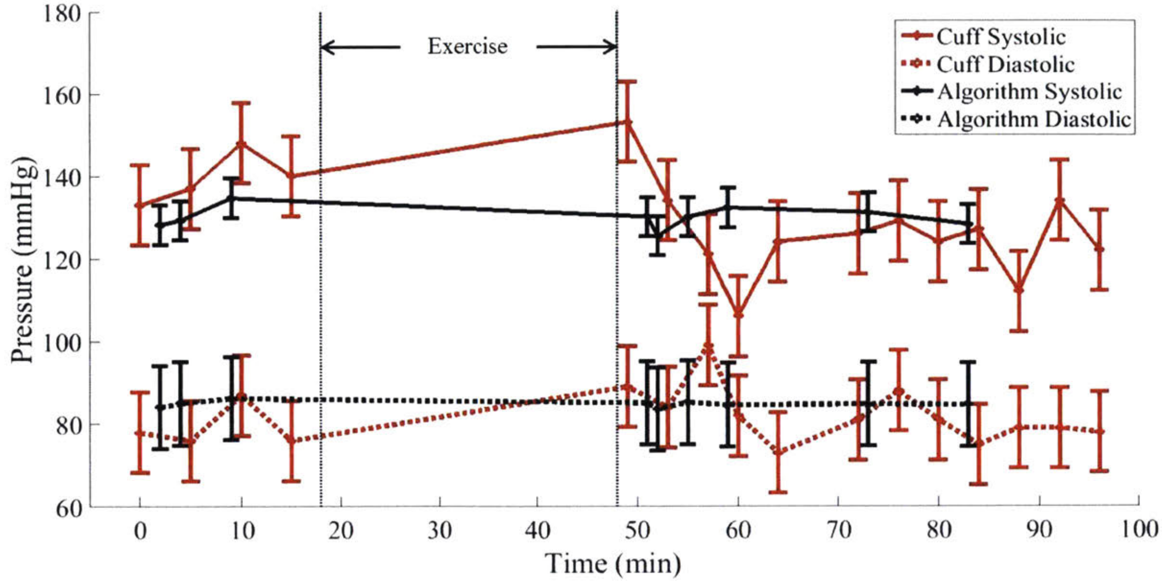

Figure 6-17: Results on a healthy volunteer both before and after exercise. For the results shown here, the k-fold cross validation parameter set from healthy volunteer 1 in Section 6.3.2 was applied to the full data set.

more algorithm measurements were taken before exercise (especially between the 10 and 18 minute mark), it might be shown that the algorithm decreases before exercise begins; this decrease might be similar to the decrease in cuff pressure over the same period.

Within two minutes after exercise concluded, the first cuff measurement was taken. It is clear from the figure that cuff pressure increased from before exercise and to immediately after exercise. While the algorithm trendlines decrease from before exercise to after exercise, the trendlines shown make sense because (1) the pressure likely decreased after the last pre-exercise algorithm measurement as indicated by the cuff pressure between minute 10 and 18 and (2) the first post-exercise algorithm measurement is lower than the maximum post-exercise blood pressure in the carotid artery because of the time between ending exercise and taking an algorithm measurement. Further, from the literature, it is expected that the blood pressure minimum in the carotid after exercise occurs sooner than the blood pressure minimum in the brachial artery after exercise; this is exactly what is shown in the raw results plot. After reaching a minimum, the blood pressure is expected to plateau near the baseline, which is exactly what the algorithm measurements show in the raw data plot. Based on the above analysis, the trendlines displayed in Figure 6-16 make intuitive sense.

While pulse pressures reported in the raw results are lower than expected, this phenomenon has been apparent from other algorithm trendlines examined in this chapter; it might be possible to correct for this problem by increasing the parameter k in Equation 3.16. Further, it is clear from the plots that diastolic pressure predicted by the algorithm more closely agrees with the cuff than the systolic pressure measurement; again, this is exactly as discussed in other plots in this chapter.

The algorithm results obtained after calibration with the parameters found from healthy volunteer 1 in Section 6.3.2 show significantly less variation than the cuff over time. As expected from previous discussions of the calibration technique, the calibration serves to smooth or dampen changes in blood pressure reported by the algorithm. This is likely due to high y-intercepts and low slopes in the final calibration parameters. In the future, limits on these calibration parameters could increase agreement between the cuff and algorithm.

6.7 Carotid Artery Self-Scans Compilation

6.7.1 Study Specifics

As part of this chapter, many algorithm measurements were taken using the 'self-scan' protocol. In this section, most of the self-scans taken are combined; the scans completed immediately after exercise or caffeine intake were excluded from the compilation.

6.7.2 Results

When the self-scans are combined as specified above, Figure 6-18 can be generated, which displays the raw results of the algorithm. The mean and median of the absolute relative error results in the figure are 18.01 % and 16.84 %, respectively, for systolic pressure and 12.06 % and 8.60 %, respectively, for diastolic pressure. The precision and accuracy for systolic and diastolic pressures are -19.43 mmHg ± 14.11 mmHg and

-3.31 mmHg ± 10.99 mmHg, respectively.

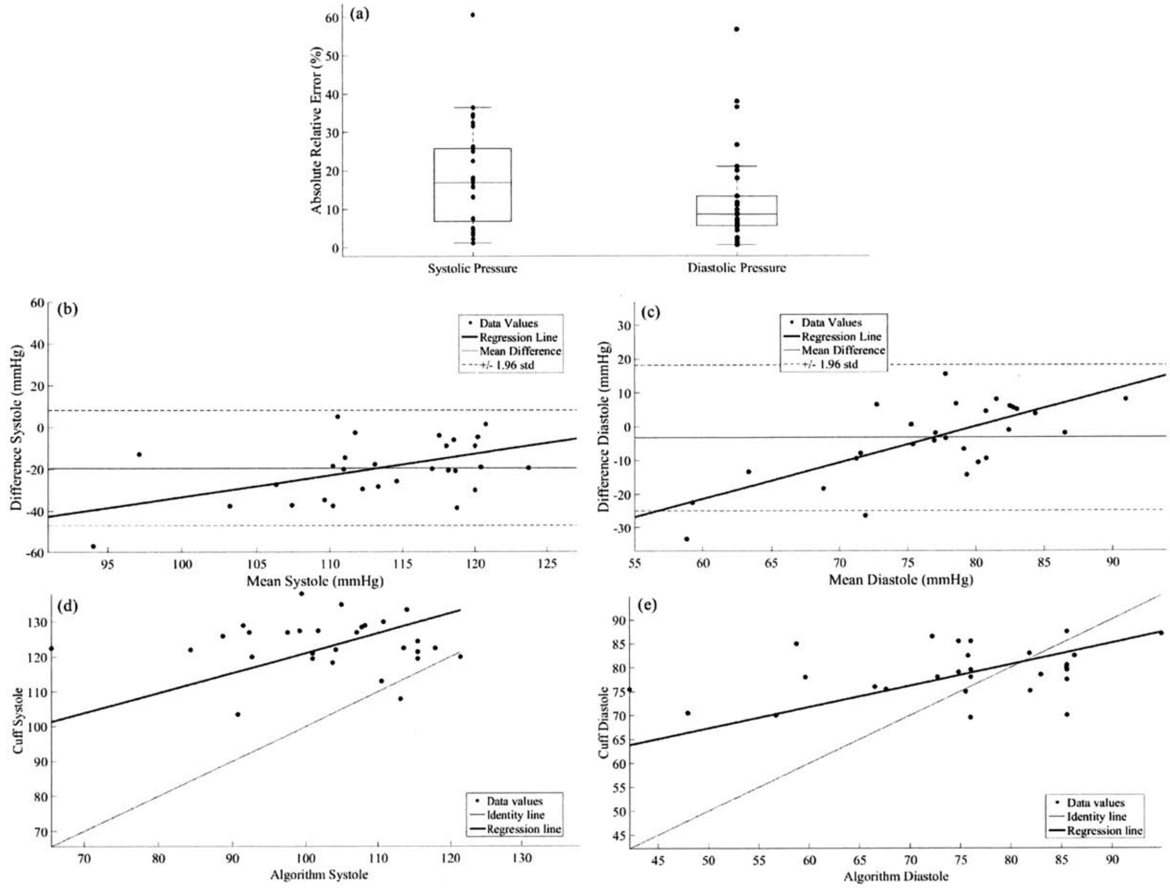

Figure 6-18: Results showing a compilation of most self-scans completed for the studies on healthy volunteers in this chapter. The results presented here are raw algorithm results. The figure plots the quantities discussed in Section 5.2.

The k-fold cross-validation method is applied to the raw algorithm results and the result on the test set is shown in Figure 6-19. The mean and median of the absolute relative error results in the figure are 4.21 % and 2.82 %, respectively, for systolic pressure and 6.59 % and 6.71 %, respectively, for diastolic pressure. The precision and accuracy for systolic and diastolic pressures are -0.14 mmHg ± 7.55 mmHg and 1.81 mmHg ± 6.17 mmHg, respectively. Table 6.2 shows the statistics of the k-fold cross-validation method applied to 2000 different sortings into training and test sets.

The k-fold cross-validation parameter set found above was then applied to the entire data set. The results are shown in Figure 6-20. The mean and median of the absolute relative error results in the figure are 4.30 % and 3.51 %, respectively, for

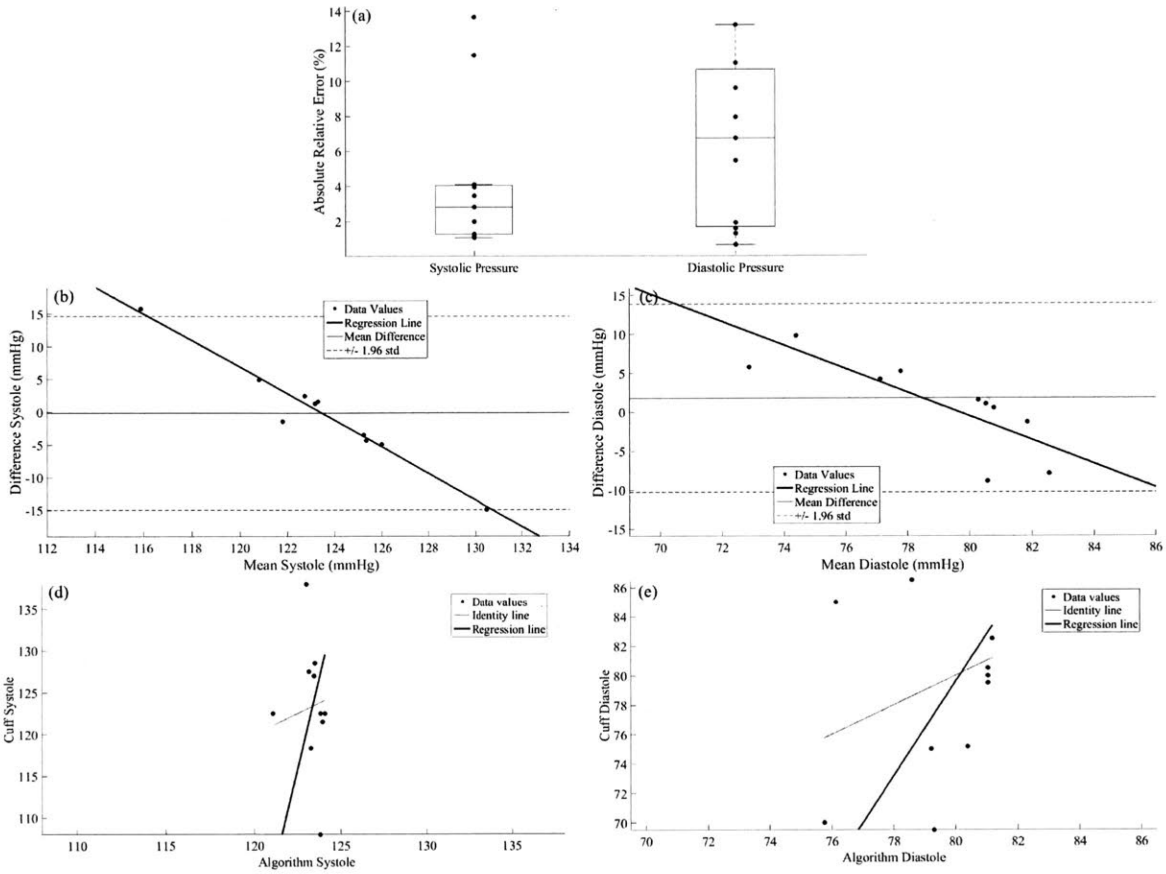

Figure 6-19: Results showing a compilation of most self-scans completed for the studies on healthy volunteers in this chapter. The results presented here are test set results from the k-fold cross-validation method. The figure plots the quantities discussed in Section 5.2.

systolic pressure and 4.78 % and 3.23 %, respectively, for diastolic pressure. The precision and accuracy for systolic and diastolic pressures are 0.06 mmHg ± 7.00 mmHg and 0.62 mmHg ± 4.88 mmHg, respectively.

6.7.3 Discussion

The results presented above indicate an excellent precision and accuracy for the algorithm. However, it is not clear what is the proper calibration procedure. For example, in a final medical device, one option is to take data many times of the course of minutes in order to calibrate the algorithm to the volunteer's specific carotid artery (such as in Sections 6.3 and 6.4). Another option is calibrate based on 'stock' data

Table 6.2: Statistics obtained after running the k-fold cross-validation method for 2000 different random sortings into training set and test set. The results are from a compilation of self-scans on healthy volunteers. In this table, α is a 2000 element vector where each element of the vector is the mean of the errors in a particular random sorting.

	Mean of α (mmHg)	Minimum of α (mmHg)	Maximum of α (mmHg)	Minimum of Test Set Errors (mmHg)	Maximum of Test Set Errors (mmHg)
Systolic	0.10	-8.08	10.19	-17.69	26.01
Diastolic	-0.05	-6.47	7.10	-13.54	12.62

captured on a wider population (such as in Chapter 5), thus eliminating the need for a volunteer-specific calibration. In this section, the calibration occurs using the 'stock' data on a wider population.

6.8 Summary

In this chapter, the results of self-scans on healthy volunteers were examined. In particular, longitudinal studies on two healthy volunteers were completed. The effect of caffeine and exercise on blood pressure was also investigated in this chapter. Finally, a compilation of most of healthy self-scans in this chapter was examined.

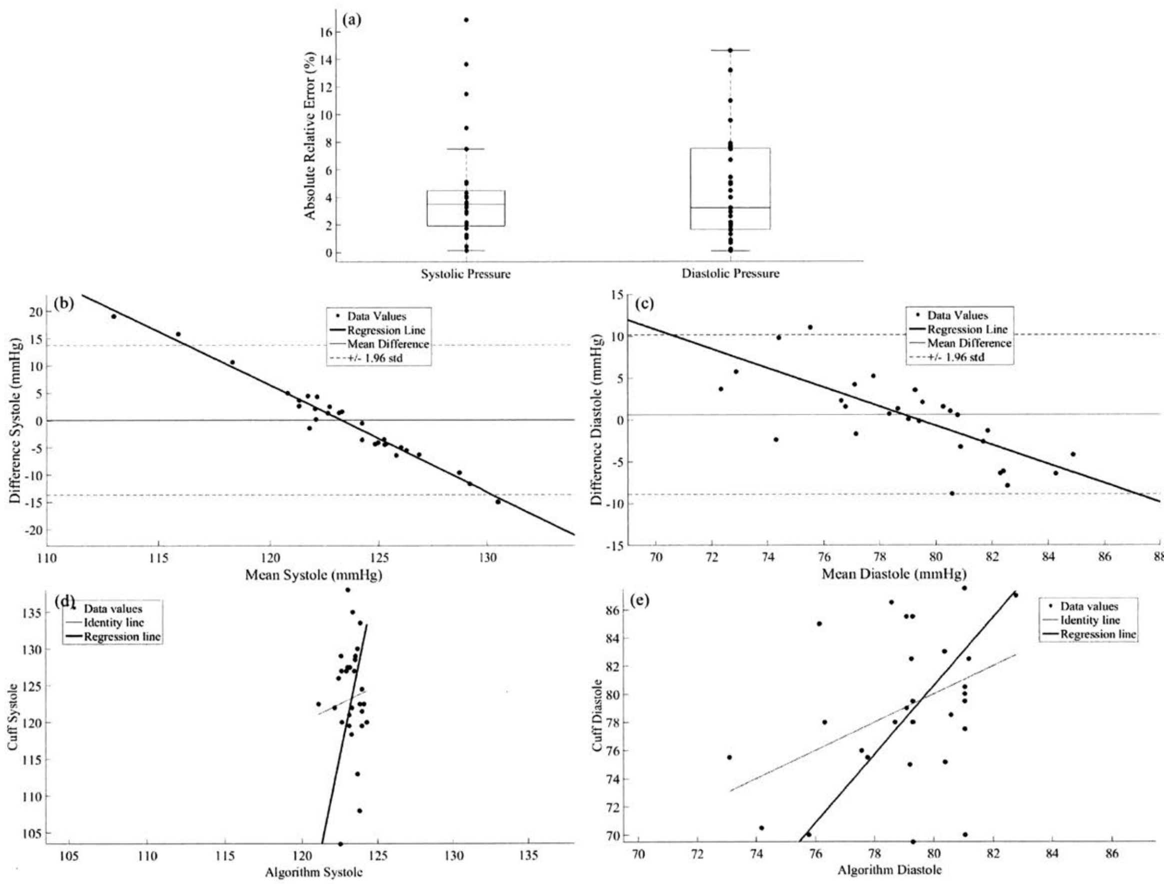

Figure 6-20: Results showing a compilation of most self-scans completed for the studies on healthy volunteers in this chapter. The results presented here are full data set results after the k-fold cross-validation parameter set was applied.

Chapter 7

Hypertensive, Hypotensive, and Older Volunteers

In this chapter, the algorithm performance is tested and verified on a medicated hypertensive volunteer, on a hypotensive volunteer, and on a set of four older volunteers. Note that the volunteers in previous chapters were mostly in their 20s. The purpose of this chapter is to evaluate the algorithm performance on volunteers that are not nominally-healthy.

7.1 Data Acquisition Specifics

The Massachusetts Institute of Technology (MIT) IRB approved the following studies. Volunteers for the studies gave informed consent. Inclusion criteria included (a) being over 18 years of age, (b) non-pregnant mothers, (c) being diagnosed as hypertensive or hypotensive, and (d) being older than 30 years of age. Exclusion criteria included (a) volunteers with pacemakers and (b) overweight volunteers (BMI 30 $\frac{kg}{m^2}$ and greater).

First, a cuff measurement was taken on the volunteer. Next, force sweeps were taken using the GE Logiq E9 ultrasound machine (General Electric, Boston, MA, USA) and a GE 9L-D linear probe (General Electric, Boston, MA, USA). Each force sweep began at a contact force of approximately 1.5 N and ended at appropriately 12 N. Due to the available buffer of this GE machine, the sweeps lasted approximately

30 seconds each. After the force sweeps were completed, the cuff was used to take another blood pressure measurement on the volunteer's arm.

7.2 Variation of the Algorithm Over Minutes

7.2.1 Medicated Hypertensive Volunteer

Data Acquisition Specifics

Because 10 full seated force sweeps were completed on each visit day for this volunteer, the algorithm performance over the course of 15 minutes can be investigated. The study protocol described in Section 7.1 was followed and sweeps were administered by study personnel and were not self-administered.

Results

In Figure 7-1, the raw algorithm results are displayed, without any post-processing. In the figure, (a)-(e) display plots as described in Section 5.2 and (f) shows the results as a function of minutes after the study began. A comparison between this plot and Figure 6-1 allows an evaluation of how the variability of the algorithm compares with the cuff. The means of the data shown in Figure 7-1 are 109.09 mmHg and 85.53 mmHg for systolic and diastolic pressures, respectively. The standard deviations are 14.39 mmHg and 9.05 mmHg for systolic and diastolic pressures, respectively. For the data displayed in the figure, the mean and median of the absolute relative error for systolic pressure are 15.00 % and 10.90 %, respectively, and for diastolic pressure are 8.54 % and 8.38 %, respectively. The precision and accuracy of the data for systolic and diastolic pressure are -15.78 mmHg $\pm$ 14.59 mmHg and 3.43 mmHg $\pm$ 10.06 mmHg, respectively.

For this hypertensive volunteer, k-fold cross validation parameters were obtained using the process described in Section 3.4.1; the parameters obtained using that process were applied to the test set and the results are shown in Figure 7-2. The means of the data shown in Figure 7-2 are 120.88 mmHg and 83.49 mmHg for systolic and diastolic

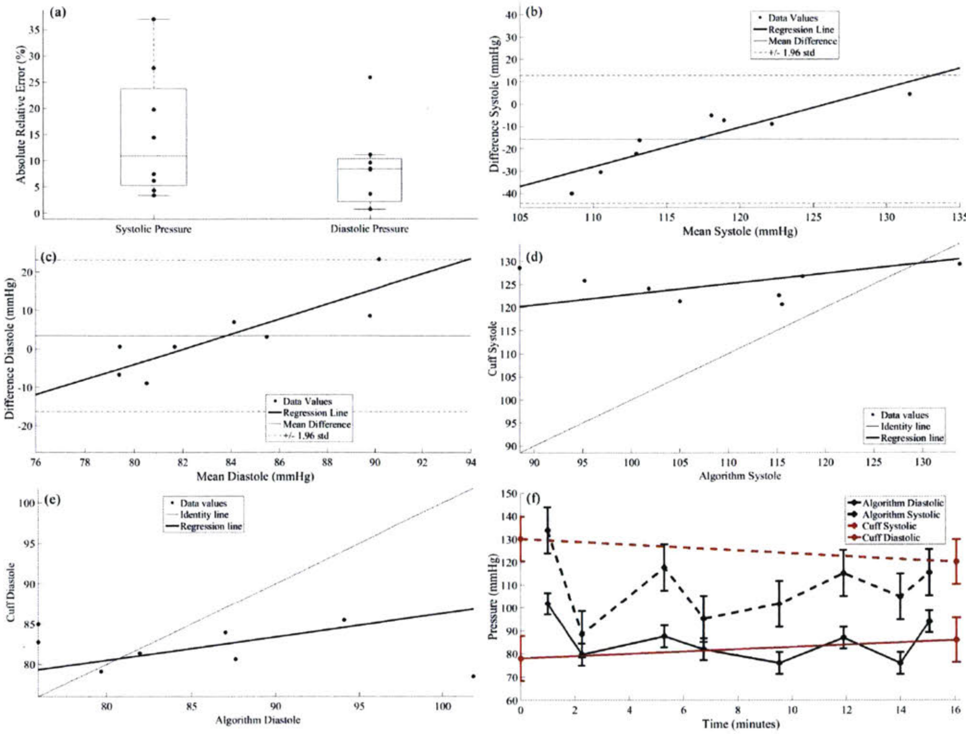

Figure 7-1: Algorithm results showing the variation of blood pressure readings on a medicated hypertensive volunteer over the course of approximately 15 minutes. The results displayed here are the raw results of the algorithm without any post-processing. Plots (a) through (e) show the quantities discussed in Section 5.2; plot (f) shows the trend lines over approximately 15 minutes for both cuff and algorithm.

pressure, respectively. The standard deviations are 1.52 mmHg and 0.32 mmHg for systolic and diastolic, respectively. For the data displayed in the figure, the mean and median of the absolute relative error for systolic pressure are 4.16 % and 4.14 %, respectively, and for diastolic pressure are 2.96 % and 2.23 %, respectively. The precision and accuracy of the data for systolic and diastolic pressure are -4.34 mmHg ± 5.21 mmHg and 1.67 mmHg ± 2.73 mmHg, respectively. The k-fold cross-validation method was applied to all different sortings between the training set and test set. The relevant statistics are shown in Table 7.1.

Finally, the k-fold cross validation parameters found above were applied to the full set in order to examine the technique performance on the entire data set. Results are shown in Figure 7-3. The means of the data shown in Figure 7-3 are 123.23 mmHg and 82.81 mmHg for systolic and diastolic pressures, respectively. The standard deviations

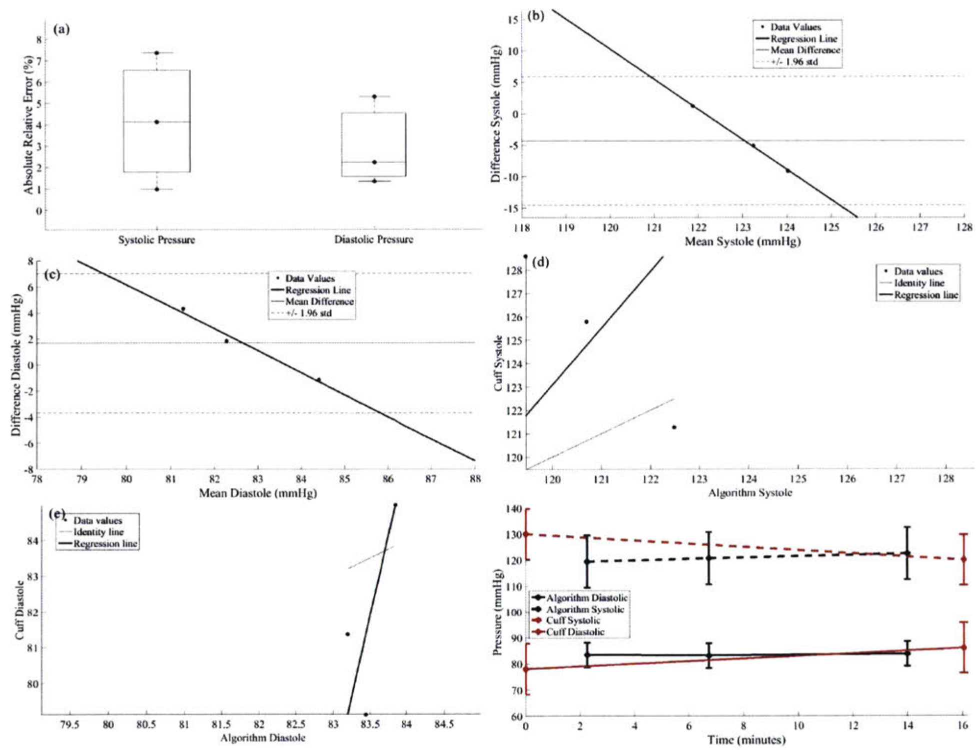

Figure 7-2: Algorithm results showing the variation of blood pressure readings on a medicated hypertensive volunteer over the course of approximately 15 minutes. The results displayed here are the test set results after the k-fold cross-validation algorithm was applied. Plots (a) through (e) show the quantities discussed in Section 5.2; plot (f) shows the trend lines over approximately 15 minutes for both cuff and algorithm.

are 2.63 mmHg and 0.98 mmHg for systolic and diastolic pressures, respectively. For the data displayed in the figure, the mean and median of the absolute relative error for systolic pressure are 2.69 % and 1.64 %, respectively, and for diastolic pressure are 2.70 % and 2.30 %, respectively. The precision and accuracy of the data for systolic and diastolic pressure are -1.64 mmHg $\pm$ 4.10 mmHg and 0.71 mmHg $\pm$ 2.55 mmHg, respectively.

Discussion

In the results presented above, cuff measurements were only taken twice: once before the force sweeps were started and once after the force sweeps completed. Thus, in order to obtain the statistics above, the cuff measurements were interpolated onto the time that the algorithm measurement was taken; as part of this process, the cuff

Table 7.1: Statistics obtained after running the k-fold cross-validation method for all sortings into training set and test set for the multi-visit medicated hypertensive volunteer. In this table, α is a vector where each element of the vector is the mean of the errors in a particular random sorting.

	Mean of α (mmHg)	Minimum of α (mmHg)	Maximum of α (mmHg)	Minimum of Test Set Errors (mmHg)	Maximum of Test Set Errors (mmHg)
Systolic	-1.12	-10.36	5.74	-15.35	6.75
Diastolic	0.19	-4.71	4.88	-7.50	10.16

measurements were assumed to be taken one minute before the start of the first force sweep and one minute after the end of the last force sweep. This is a source of error as it is unknown how the cuff measurements vary within that 15 minute timespan.

Another source of error for this particular data set is the fact that the data set consists of only 8 points; this means that the test set, described in Section 3.4.1 as only 1/3 of the full set excluding outliers, is small. The consequence of this is less robust cross-validation results. Still, the results presented above show an accuracy and precision that is acceptable for a final medical device.

7.2.2 Hypotensive Volunteer

Data Acquisition Specifics

The hypotensive volunteer had data taken once every 90 seconds for 15 minutes. A cuff measurement was taken before the force sweeps began and again after the force sweeps ended. The force sweeps were self-administered by the seated volunteer.

This volunteer was diagnosed as hypotensive and, while not taking medication, was implementing life-style changes to address the condition, including a high sodium diet.

Results

The raw results of the algorithm on the hypotensive volunteer are shown in Figure 7-4. The means of the data shown in Figure 7-4 are 92.95 mmHg and 67.93 mmHg for systolic and diastolic pressures, respectively. The standard deviations are 4.66

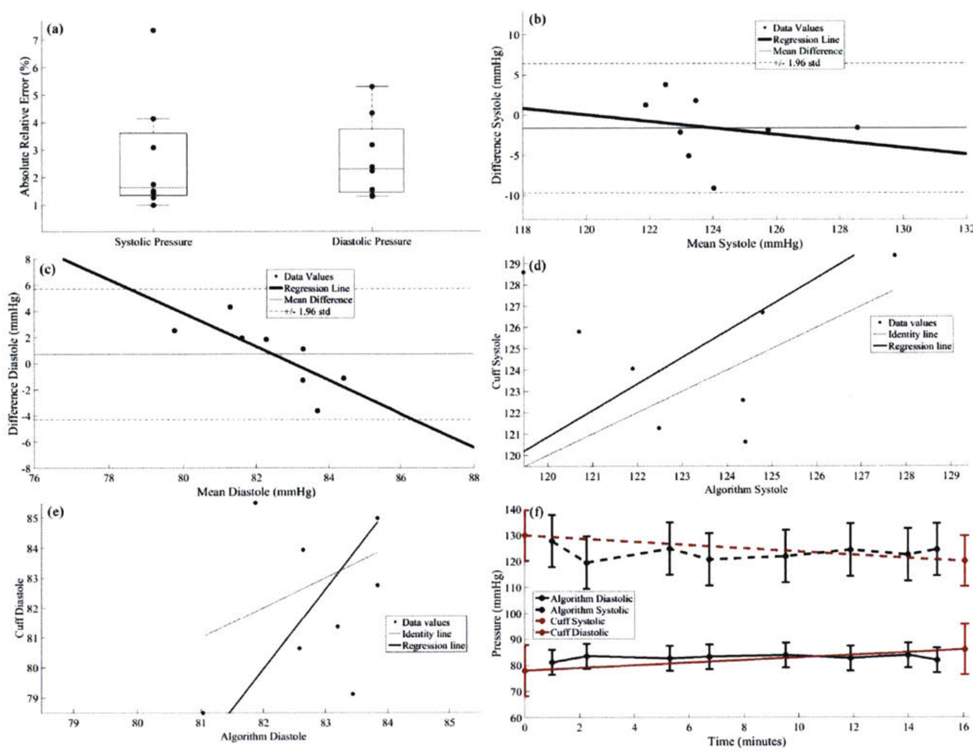

Figure 7-3: Algorithm results showing the variation of blood pressure readings over the course of approximately 15 minutes for the multi-visit medicated hypertensive volunteer. The results shown here are the results of the algorithm after the k-fold cross-validation parameter set is applied to the entire set. Plots (a) through (e) show the quantities discussed in Section 5.2; plot (f) shows the trend lines over approximately 15 minutes for both cuff and algorithm.

mmHg and 7.90 mmHg for systolic and diastolic pressures, respectively. For the data displayed in the figure, the mean and median of the absolute relative error for systolic pressure are 10.74 % and 11.75 %, respectively, and for diastolic pressure are 9.51 % and 11.48 %, respectively. The precision and accuracy of the data for systolic and diastolic pressure are -10.50 mmHg $\pm$ 7.35 and 0.54 mmHg $\pm$ 7.89 mmHg, respectively.

The raw algorithm results were used in the k-fold cross validation algorithm from Section 3.4.1, and the results on the test set are shown in Figure 7-5. The means of the data shown in Figure 7-5 are 104.22 mmHg and 67.42 mmHg for systolic and diastolic pressures, respectively. The standard deviations are 2.91 mmHg and 0.09 mmHg for systolic and diastolic pressures, respectively. For the data displayed in the figure, the mean and median of the absolute relative error for systolic pressure are 2.83 % and 2.67 %, respectively, and for diastolic pressure are 0.28 % and 0.27 %,

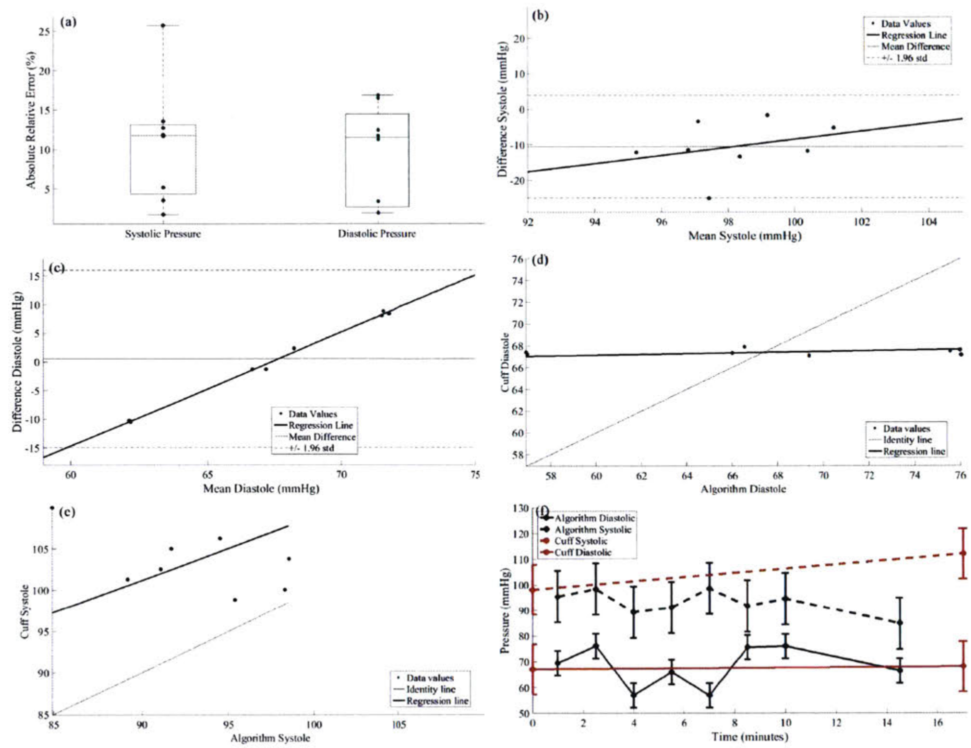

Figure 7-4: Algorithm results showing the variation of blood pressure readings on a hypotensive volunteer over the course of approximately 15 minutes. The results displayed here are the raw results of the algorithm without any post-processing. Plots (a) through (e) show the quantities discussed in Section 5.2; plot (f) shows the trend lines over approximately 15 minutes for both cuff and algorithm. Outliers were excluded from the plots.

respectively. The precision and accuracy of the data for systolic and diastolic pressure are 2.93 mmHg $\pm$ 2.1440 mmHg and 0.19 mmHg $\pm$ 0.09 mmHg, respectively.

The k-fold cross validation parameter set from above was used on the full data set and the results are shown in Figure 7-6. The means of the data shown in Figure 7-6 are 104.17 mmHg and 67.41 mmHg for systolic and diastolic pressures, respectively. The standard deviations are 2.82 mmHg and 0.08 mmHg for systolic and diastolic pressures, respectively. For the data displayed in the figure, the mean and median of the absolute relative error for systolic pressure are 2.37 % and 2.77 %, respectively, and for diastolic pressure are 0.34 % and 0.33 %, respectively. The precision and accuracy of the data for systolic and diastolic pressure are 0.71 mmHg $\pm$ 3.04 mmHg and 0.02 mmHg $\pm$ 0.27 mmHg, respectively.

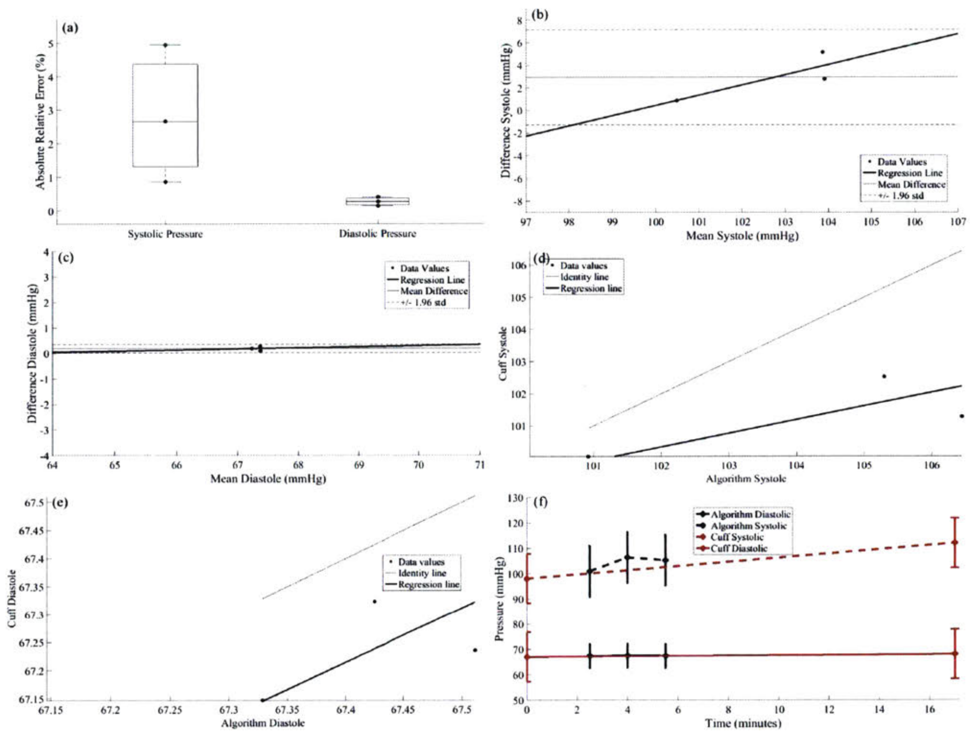

Figure 7-5: Algorithm results showing the variation of blood pressure readings on a hypotensive volunteer over the course of approximately 15 minutes. The results displayed here are the test set results after the k-fold cross-validation algorithm was applied. Plots (a) through (e) show the quantities discussed in Section 5.2; plot (f) shows the trend lines over approximately 15 minutes for both cuff and algorithm. Outliers were excluded from the plots.

Discussion

From the hypotensive longitudinal results above, it is clear that there is good agreement between the algorithm reported blood pressures and the cuff reported blood pressures. Further, the standard deviations reported by the algorithm over 15 minutes are comparable to the cuff variations discussed in Section 6.2. However, analysis is limited due to the fact that only two cuff measurements were acquired and data acquisition only occurred over 15 minutes.

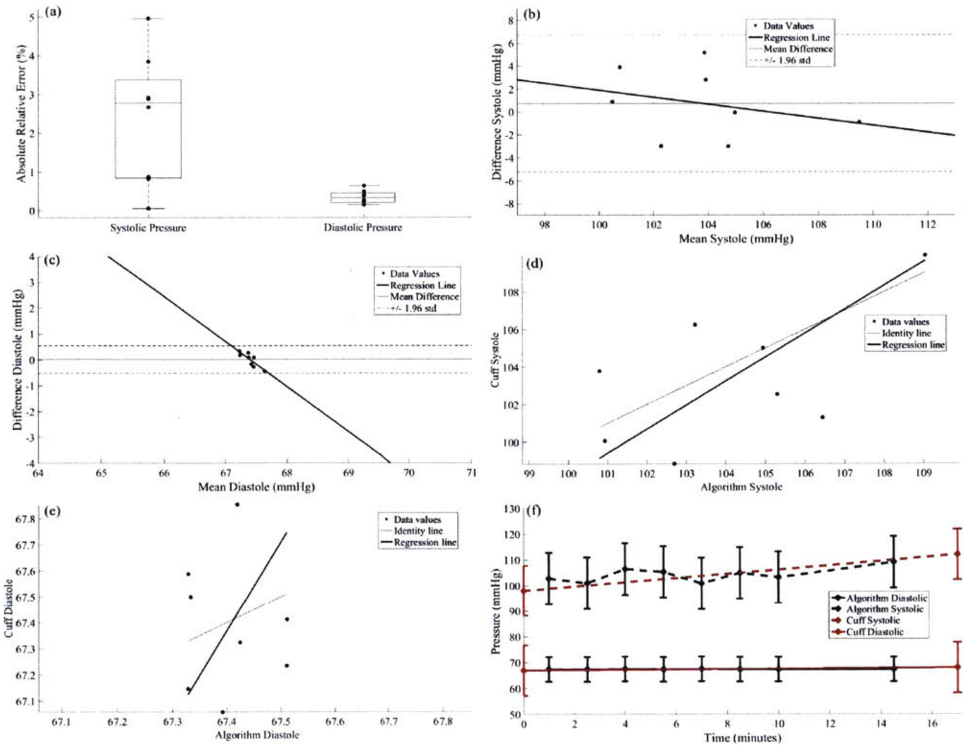

Figure 7-6: Algorithm results showing the variation of blood pressure readings over the course of approximately 15 minutes for the multi-visit hypotensive volunteer. The results shown here are the results of the algorithm after the k-fold cross-validation parameter set is applied to the entire set. Plots (a) through (e) show the quantities discussed in Section 5.2; plot (f) shows the trend lines over approximately 15 minutes for both cuff and algorithm. Outliers were excluded from the plots.

7.3 Variation of Cuff and Algorithm Over Days

7.3.1 Medicated Hypertensive Volunteer

Data Acquisition Specifics

The medicated hypertensive volunteer completed seven data acquisition sessions over the course of a month. Each session began with a resting period in order to stabilize blood pressure after walking to the testing site. After heart rate had decreased, the procedure described in Section 7.1 was completed; sweeps were administered by study personnel and were not self-administered.

Results

On seven non-consecutive days, data was taken on this medicated hypertensive volunteer and the raw algorithm results without k-fold cross-validation are shown in Figure 7-7. The results show that the systolic pressure is underestimated compared to the cuff and that the algorithm diastolic pressure closely tracks the cuff diastolic pressure; this is exactly as expected based on the physiology discussed in Section 1.1. Results also indicate directional agreement between the cuff and the algorithm. For the data displayed in the figure, the mean and median of the absolute relative error for systolic pressure are 13.46 % and 15.56 %, respectively, and for diastolic pressure are 7.09 % and 5.09 %, respectively. The precision and accuracy of the data for systolic and diastolic pressures are -14.86 mmHg ± 7.28 mmHg and -1.33 mmHg ± 6.97 mmHg, respectively.

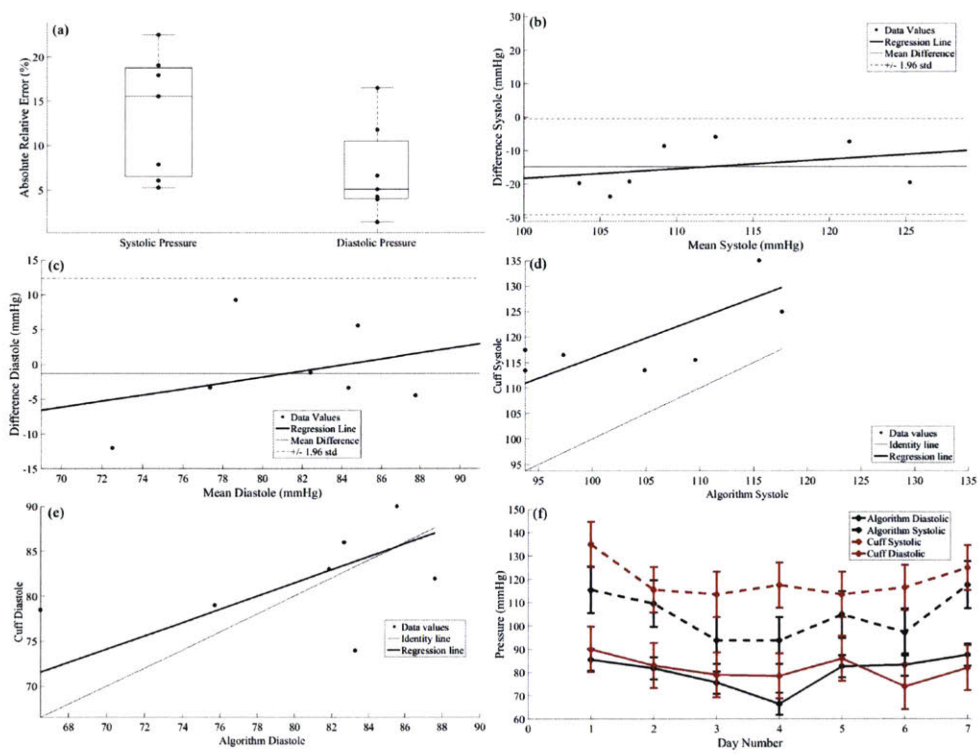

Figure 7-7: Algorithm results from the seven visits by a medicated hypertensive volunteer. The results shown here are the raw algorithm results. Plots (a) through (e) show the quantities discussed in Section 5.2; plot (f) shows the trend lines over the 7 days for both cuff and algorithm.

The k-fold cross-validation parameter set found in Section 7.2.1 is applied to the entire full set of seven points and the result is shown in Figure 7-8. This amounts to a patient-specific calibration. The results show that the algorithm and the cuff closely agree over the seven displayed points. For the data displayed in the figure, the mean and median of the absolute relative error for systolic pressure are 4.96 % and 5.92 %, respectively, and for diastolic pressure are 5.43 % and 5.99 %, respectively. The precision and accuracy of the data for systolic and diastolic pressure are 2.92 mmHg ± 6.73 mmHg and 1.57 mmHg ± 5.62 mmHg, respectively. This is important because it is the first result that verifies the algorithm's validity on a hypertensive volunteer.

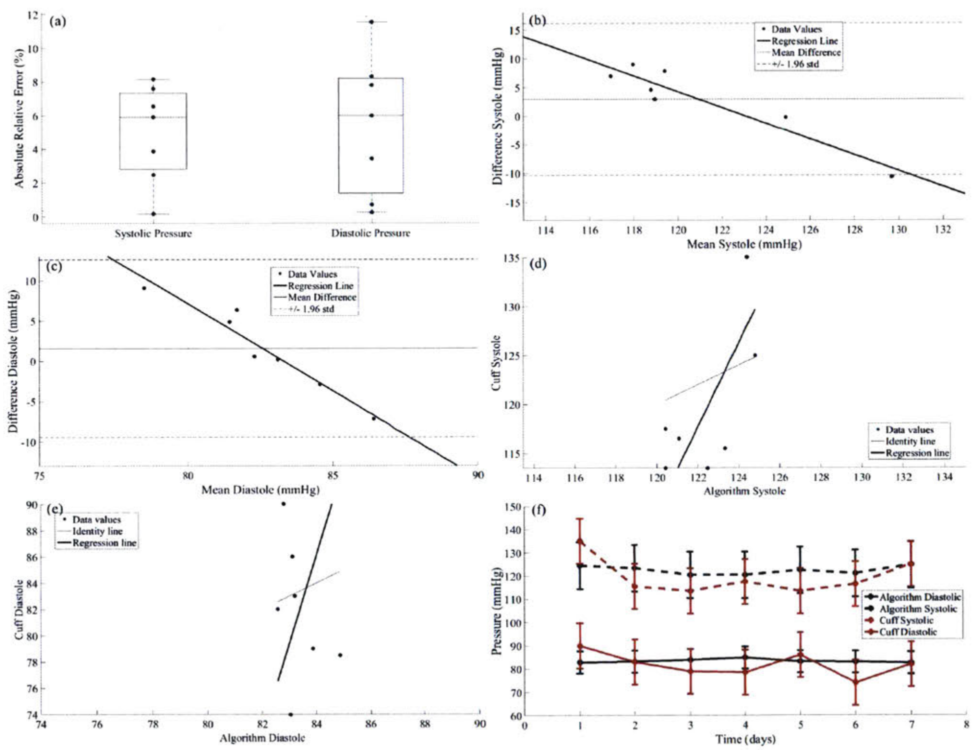

Figure 7-8: Algorithm results from the seven visits by a medicated hypertensive volunteer. The results shown here were obtained by applying the k-fold cross-validation results from Section 7.2.1 to the full set. Plots (a) through (e) show the quantities discussed in Section 5.2; plot (f) shows the trend lines over the 7 days for both cuff and algorithm.

Discussion

From Figure 7-7, we see that both the cuff and algorithm pressures first decrease then increase over the 7 days. This is as expected considering the periodicity of blood pressure due to the volunteer's medication regimen.

As mentioned in Section 6.3.3, the diastolic raw algorithm results agree more closely with the cuff than the systolic raw algorithm results. The correlation plots shown above in Figure 7-8 indicate significant variation from the one-to-one line, but the Bland-Altman plots show a mean and 1.96 standard deviation line that is as expected for a novel blood pressure measurement device.

7.3.2 Hypotensive Volunteer

Study Specifics

A hypotensive volunteer completed 14 data acquisition sessions over the course of a month. Each data acquisition session proceeded as described in Section 7.1 above, however the scans were self-administered by the seated hypotensive volunteer. During a typical data acquisition session, between three and six sweeps were completed.

Results

The raw algorithm results from the hypotensive volunteer are shown in Figure 7-9. Outliers are excluded from the figure. From the results in the figure, the mean and median of the absolute relative error in these plots are 7.61 % and 6.46 %, respectively, for systolic pressure and 11.57 % and 11.83 %, respectively, for diastolic pressure. The accuracy and precision displayed in the figure are -2.90 mmHg $\pm$ 8.78 mmHg for systolic pressure and -6.28 mmHg $\pm$ 6.40 mmHg for diastolic pressure.

The k-fold cross validation parameters found in Section 7.2.2 were applied to the full set from the hypotensive volunteer and the results are shown in Figure 7-10. Note that in this figure, outliers were *not* excluded. From the results in the figure, the mean and median of the absolute relative error results in the figure are 8.74 % and 9.04 %, respectively, for systolic pressure and 4.92 % and 3.79 %, respectively, for diastolic pressure. The precision and accuracy for systolic and diastolic pressures are -1.99 mmHg $\pm$ 11.11 mmHg and -2.12 mmHg $\pm$ 3.70 mmHg, respectively.

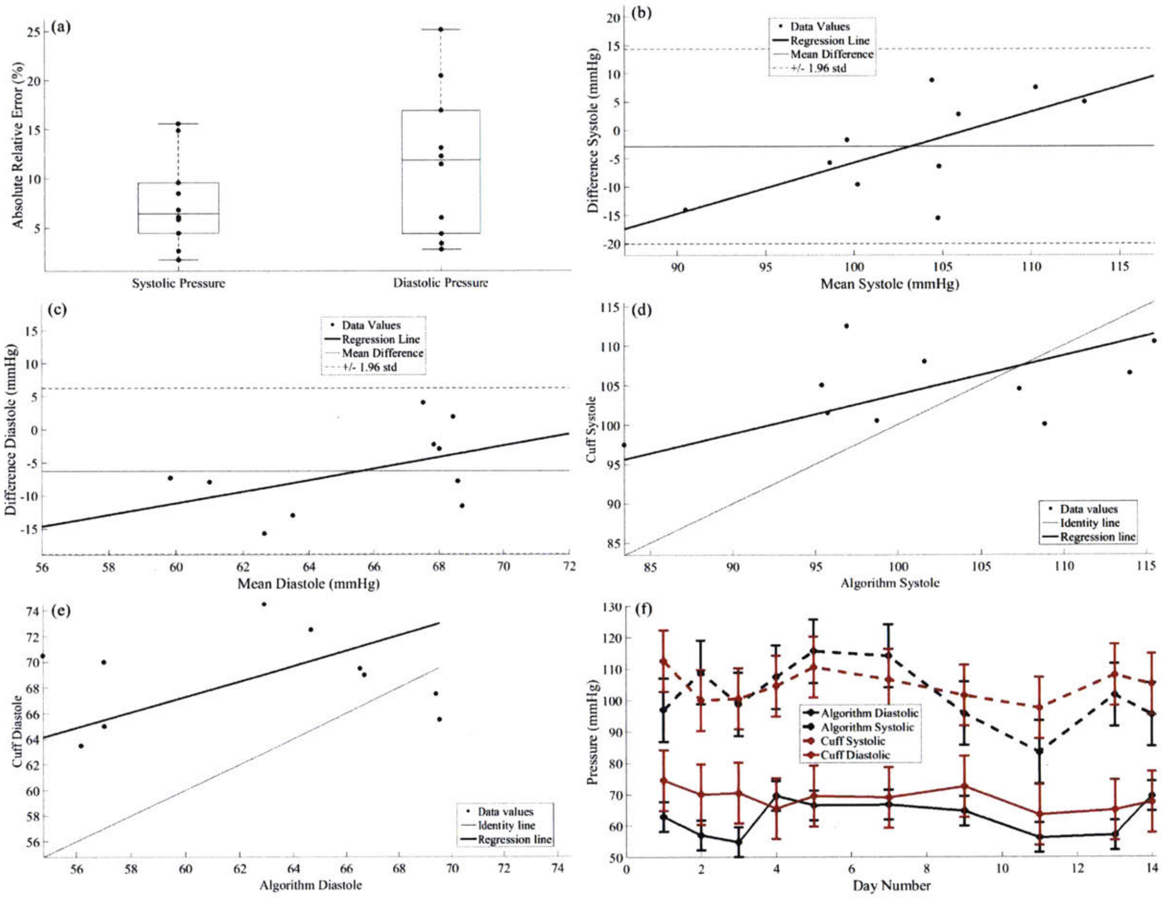

Figure 7-9: Algorithm results from the 14 visits by a hypotensive volunteer. The results shown here are the raw algorithm results. Plots (a) through (e) show the quantities discussed in Section 5.2; plot (f) shows the trend lines over the 14 days for both cuff and algorithm. Outliers were excluded from the plots.

Discussion

It is clear from the results in Figure 7-9 that the raw results of the algorithm closely track the cuff measurements (after excluding outliers). The accuracy and precision results for the raw data is excellent compared to results on healthy volunteers in Section 5.3 and compared to other results presented in this dissertation. The k-fold cross validation algorithm serves to smooth out the algorithm results; this smoothing reduces the accuracy and precision numbers even further. However, from the results, it is clear that the k-fold cross validation is not needed for this hypotensive volunteer.

Finally, it is important to note that there was significant difficulty using the cuff on this volunteer. Results from the cuff were frequently of poor quality (either very

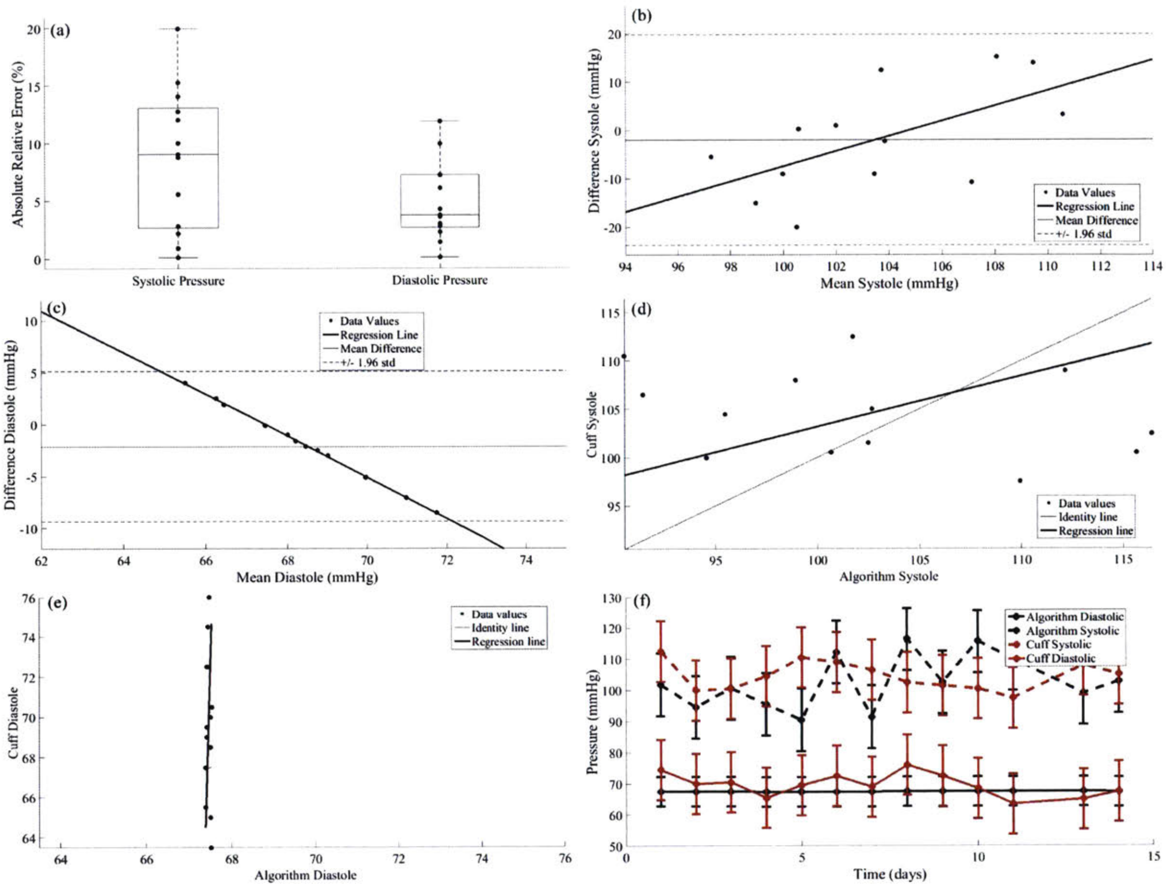

Figure 7-10: Algorithm results from the 14 visits by a hypotensive volunteer. The results shown here were obtained by applying the k-fold cross-validation results from Section 7.2.2 to the full set. Plots (a) through (e) show the quantities discussed in Section 5.2; plot (f) shows the trend lines over the 14 days for both cuff and algorithm. Outliers were not excluded from the plots.

high or very low, and inconsistent after repeated measurements). This is important when analyzing the results of this section.

7.4 Older Volunteers

7.4.1 Study Specifics

Four single-visit older volunteers (at least 30 years old) completed self-scans on their own carotid artery. During each data acquisition session, a total of five force sweeps were taken by the seated volunteer and the protocol in Section 6.1 was followed. Two of the patients took data with the GE Logiq E9 machine and the GE 9L-D linear probe; however, two of the patients took data on the Supersonics Image Aixplorer machine and linear probe discussed in Section 5.1. This difference in hardware used could lead to errors in the results.

7.4.2 Results

The raw algorithm results from the four older volunteers are displayed in Figure 7-11. From the results in the figure, the mean and median of the absolute relative error in these plots are 13.42 % and 13.47 %, respectively, for systolic pressure and 11.32 % and 9.57 %, respectively, for diastolic pressure. The accuracy and precision displayed in the figure are -13.21 mmHg $\pm$ 15.75 mmHg for systolic pressure and 5.09 mmHg $\pm$ 11.16 mmHg for diastolic pressure.

In Figure 7-12, results are shown such that k-fold cross validation parameters are applied to the raw data set. For the two volunteers that took data on the GE machine, the k-fold parameters from Section 6.4.2 are applied; for the two volunteers that took data on the Supersonics machine, the k-fold parameters from Section 5.3.2 are applied. From the results in the figure, the mean and median of the absolute relative error in these plots are 7.04 % and 7.62 %, respectively, for systolic pressure and 8.51 % and 7.71 %, respectively, for diastolic pressure. The accuracy and precision displayed in the figure are -5.36 mmHg $\pm$ 9.71 mmHg for systolic pressure and -3.94 mmHg $\pm$ 7.07 mmHg for diastolic pressure.

7.4.3 Discussion

From the results in Figure 7-11, it is clear that the raw algorithm results on the older volunteers have very poor accuracy when compared to the oscillometric cuff. This is made more complicated by the fact that the data was captured on two different machines.

However, after applying a k-fold parameter set corresponding to the machine that each volunteer used, the results look more promising. In particular, the accuracy and

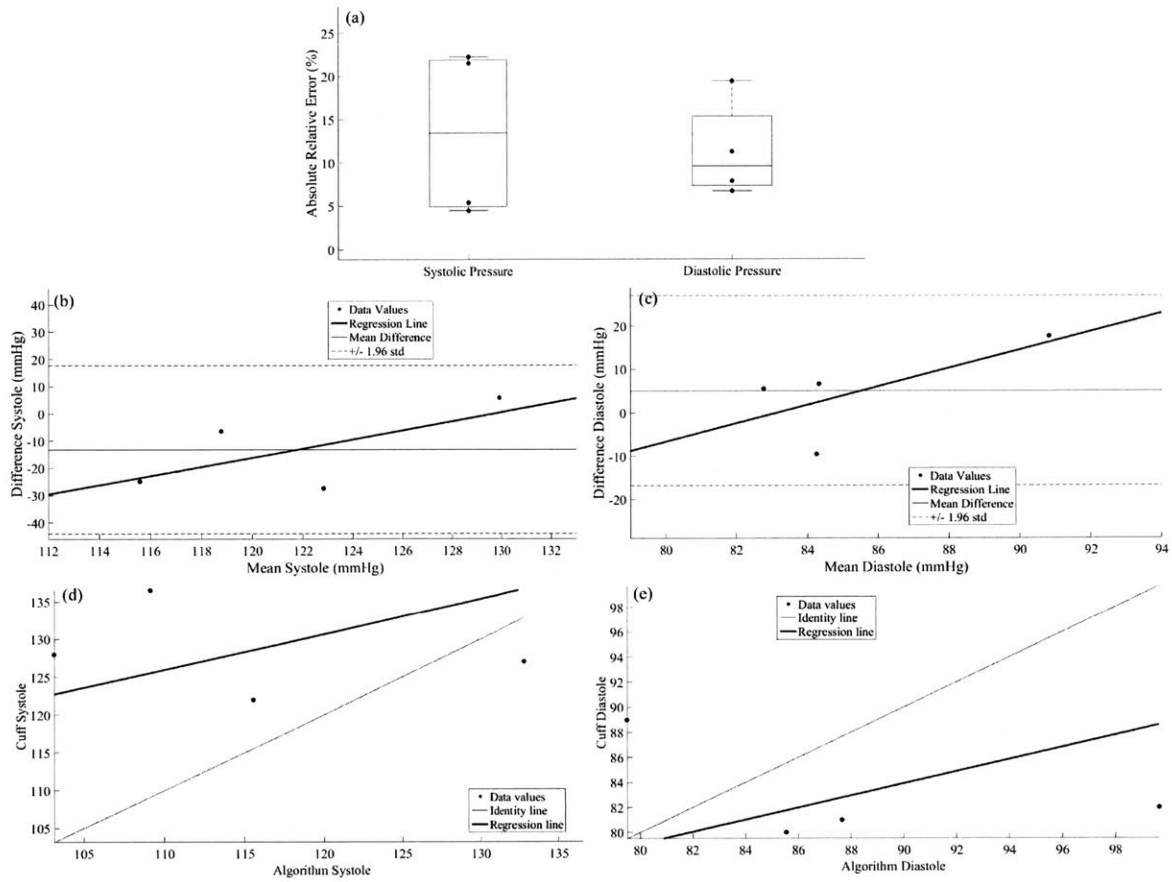

Figure 7-11: Results from four single-visit older volunteers. The results displayed here are the raw results of the algorithm, before any post-processing procedures were completed. The plots in the figure show the quantities discussed in Section 5.2.

precision numbers for the elderly patients after the k-fold parameter sets are applied are comparable to the results presented in Section 5.3.2.

More volunteers would be needed using consistent ultrasound machines in order to make more precise conclusions about the performance of the algorithm on older volunteers.

7.5 Arterial Stiffness Measurements

As discussed in Section 3.3.2, an arterial stiffness parameter is estimated during each run of the optimization. Stiffness parameters are limited to be integers between 1 and 19. Higher stiffness parameter estimates indicate a stiffer artery.

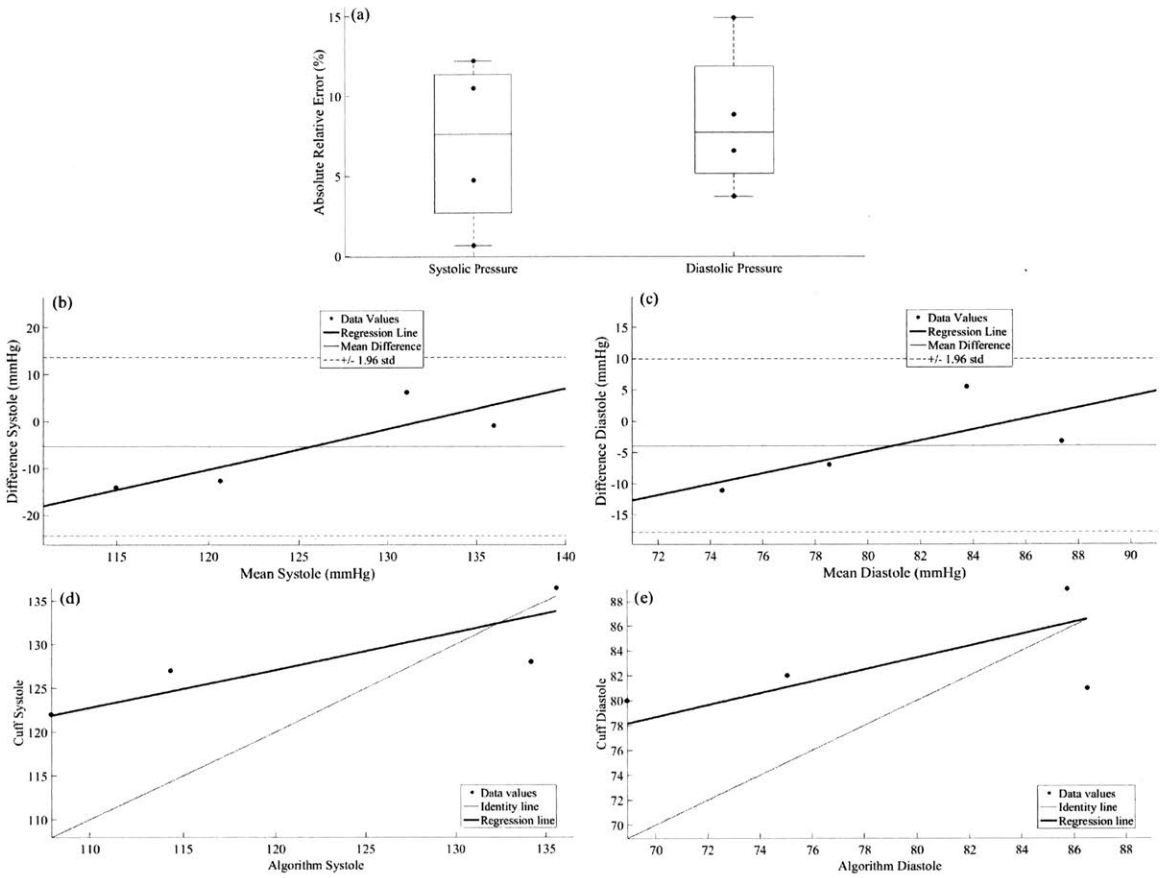

Figure 7-12: Results from four single-visit older volunteers. Recall that two of these volunteers took data on the GE system and two took data on the Supersonics system. The results displayed here are obtained by applying the k-fold parameter set from Section 6.4.2 on the two GE system volunteers and the parameter set from Section 5.3.2 on the two Supersonics volunteers. The plots in the figure show the quantities discussed in Section 5.2.

In order to validate the estimate of arterial stiffness, either phantoms or animal models would be ideally used. However, in this dissertation, a population-based comparison is completed. The average stiffness parameter for the 26 healthy volunteers, as described in Section 5.1, is 9.53. The average stiffness parameter for the 5 older volunteers (4 volunteers from Section 7.4 and one medicated hypertensive volunteer from Section 7.2.1) is 13.60.

Thus, the results indicate that, on a population basis, the healthy volunteers have a lower arterial stiffness than the older volunteers. This makes intuitive sense, as arteries are known to stiffen as a person ages.

7.6 Summary

In this chapter, algorithm performance on non-normotensive volunteers was examined. In particular, longitudinal studies on a medicated hypertensive volunteer and on a hypotensive volunteer were shown. The results indicated that, after the k-fold cross validation method is applied, the accuracy of the novel blood pressure measurement technique on non-normotensive patients is acceptable. In this chapter, the algorithm was also tested on older colunteers. Finally, stiffness measurements were compared, on a population basis, between nominally healthy young volunteers and older volunteers.

Chapter 8

Conclusions

The clinically available blood pressure measurement techniques include the arterial catheter, oscillometric cuff, and auscultatory cuff. These techniques are either inappropriate for continuous use or invasive. The technique described in this dissertation offers an improvement on the popular clinically-used devices because it is both non-invasive and non-occlusive. The dissertation described the technique in detail and validated the method on a number of different volunteers, including healthy, hypotensive, hypertensive, and elderly volunteers.

8.1 Advantages of the Technique

The method has a number of advantages that differentiate it from available techniques. First, the method is applicable to patients with hypertension and arthereosclerosis because the patient-specific artery stiffness is calculated by the algorithm each time that pressure is reported. Second, the pressure measurement is local and can be applied to any artery whose deformations are visible with ultrasound. Therefore, it is possible to obtain a pressure measurement on a patient at the carotid artery, femoral artery, and brachial artery and use these differences to diagnose cardiovascular problems. This advantage also allows pressure measurement to be obtained in the carotid artery, which is closer to the aortic arch and thus gives a pressure closer to the central blood pressure than the cuff around the brachial artery. Third, the method does not require any operator judgment (like the ausculatory cuff, which is subject to number picking preferences) as, after the force sweeps are acquired, the method proceeds without input. Fourth, the method is non-occlusive and non-invasive; this means that (with the future research described below in Section 8.4), a continuous non-invasive estimate of arterial pressure is possible. Fifth, the measurement is not ad hoc (like the oscillometric cuff) because it uses physical deformations and the governing partial differential equations (solved using finite elements) to find pressure.

8.2 Limitations of the Technique

There are important disadvantages that must be understood. First, the method requires ultrasound in order to image the artery deformations. Ultrasound is very expensive and bulky; while there is a push to reduce size and cost, the current state of ultrasound technology is a barrier to widespread use of this method. Second, the force-measurement attachment is needed to complete a blood pressure measurement; this attachment is cheap and is easily 3D printed for any existing ultrasound probe. Third, 10 second long force sweeps are needed for data acquisition; however, this time is less than the oscillometric and auscultatory cuffs. Fourth, the method requires more active thinking by the user than the oscillometric cuff method; while the training to use the method is brief and easy, the training is crucial for a non-professional to use the method.

8.3 Contributions

The contributions of this work are many-fold.

First, a technique has been developed to non-invasively and non-occlusively measure absolute blood pressure using ultrasound. The method developed for this dissertation is novel and addresses many of the disadvantages of current blood pressure measurement techniques, as described in Chapter 1.

The technique has been proven to be well-conditioned.

A real-time implementation of the technique is discussed and is feasible for the final medical device.

Next, the technique has been applied and accuracy validated in an IRB approved study where data was taken by trained sonographers on 24 nominally-healthy single-visit volunteers.

The technique has been validated in the use-case when volunteers are taking data on themselves.

The technique has been shown to give results that agree with short and long term trends in hypotensive, normotensive, and hypertensive volunteers.

The technique has been validated on two different ultrasound machines.

All of these main contributions are important steps to a final medical device that uses ultrasound to measure arterial blood pressure.

8.4 Suggestions for Future Work

8.4.1 Accuracy Improvement

In order to improve the accuracy of the technique, there are a number of next steps that could be completed. There is potential for more accuracy by increasing the fidelity of the computational model used and discussed in Chapter 2. Increased accuracy could be obtained by (1) using more accurate constitutive equations for the bulk material and, especially, the artery, (2) using a more representative model geometry, and (3) allowing for increased heterogeneity of the materials modeled. However, which such changes, there will be an increase in the number of variables that must be estimated by the optimization algorithm. It is obviously important to avoid having an under-determined system.

There is further potential for accuracy improvements by closely examining the force sweep and segmentation algorithm. More accuracy could be realized by making the force sweeps more stable. In other words, reducing the noise and making the force sweeps closer to a linear ramp would decrease error in the pre-processing steps.

Increasing the consistency and accuracy of the segmentation algorithm would allow for more repeatable algorithm results.

Finally, accuracy would be improved by obtaining more data on volunteers. In the post-processing calibration step, a parameter set is found based on the existing population set. If more data was to be gathered, the optimal parameter set would be more likely to be obtained.

8.4.2 Increase Clinical Feasibility

In order to make the process more clinically feasible, there are a number of next steps centering on data acquisition and ultrasound technology. In order to improve data acquisition and make the method clinically feasible, it would be important to have root access to the ultrasound machine used so that data doesn't need to be pulled off of the machine for processing; this might be able to be achieved by using a frame-grabber. The segmentation algorithm used in this research needs to be implemented in real-time, as has been done in the literature, and made completely automatic. Lower force sweep ranges need to be used to gather data, as this would allow quicker data acquisition and a more comfortable experience for patients. Finally, it would be beneficial to have an easier and quicker way to take data as opposed to force sweeps. All of these improvements together would allow blood pressure measurements to be obtained in real-time.

Other steps that could be taken to increase the clinical feasibility of the method revolve around improving the ultrasound technology. Changing the form factor of the ultrasound machine and the ultrasound probe would allow easier data acquisition and more practical use. Decreasing the cost of the ultrasound technology would mean that this method could be used in hospitals with small budgets. Exploring the application of this method to measurement of central venous blood pressure would increase the likelihood of technology adoption. Finally, increasing the visibility of the technology would make it more likely to be implemented in a hospital environment.

With the research described above, a medical device could take the form as shown in Figure 8-1. In this hand-held device, patients could take their own blood pressure measurement easily, quickly, and in their home.

Figure 8-1: Rendering of a proposed device that uses the technique described in this dissertation.

8.4.3 Validate Technique on Larger Population Sets

In order to further prove the validity of the method, more data could be collected. Additional data would also inform the post-processing calibration step, making it more accurate.

In particular, force sweep data from an operating room, with a patient who has an arterial line inserted, would be interesting to obtain. The results of the proposed technique could be compared to the ground-truth arterial line data. Such comparison would be instrumental in proving the importance of the proposed technique to clinicians.

Additional blood pressure measurement studies could compare the proposed technique to auscultatory cuff measurements. Through this comparison, the standards and guidelines outlined in Section 1.5 could be evaluated with respect to the proposed technique.

Obtaining additional data from patients with arterial diseases - such as atherosclerosis, hypotension, and hypertension - would be beneficial to extend the applicability of the algorithm.

Completing a study on pregnant women, children, and people with atrial fibrillation would strengthen the argument for adoption of this technology because the oscillometric cuff is known to be inaccurate on these patient populations [20].

Using the technique to measure brachial artery pressure, femoral artery pressure, and carotid artery pressure in one patient would be an interesting study because no clinically-used non-invasive technique can measure blood pressure in all of those locations.

8.4.4 Possible Applications of the Technique

As the algorithm described in this dissertation also estimates arterial elasticity (see Section 3.3.2), it would be interesting to compare the arterial elasticity estimated by the algorithm to real values. Such a study might be possible using phantoms or animal models. Accurate arterial stiffness estimates could help clinicians identify atherosclerosis and assess the cardiovascular age of a patient.

There is a range of applications based on the fact that the technique non-invasively measures fluid pressure based on deformations due to an applied external force. For example, it might be possible to use the technique to measure embryonic fluid pressure, which might be related to the health of a fetus. Interstitial fluid pressure is a quantity of interest to doctors for a number of reasons including compartment syndrome diagnosis; it might be possible to apply the algorithm to measure this pressure. Finally, pressure in veins might be able to be calculated using a modified version of the algorithm.

Bibliography

[1] Ary L Goldberger, Luis AN Amaral, Leon Glass, Jeffrey M Hausdorff, Plamen Ch Ivanov, Roger G Mark, Joseph E Mietus, George B Moody, Chung-Kang Peng, and H Eugene Stanley. Physiobank, physiotoolkit, and physionet. *Circulation*, 101(23):e215–e220, 2000.

[2] Ikaro Silva and George B Moody. An open-source toolbox for analysing and processing physionet databases in matlab and octave. *J Open Res Softw*, 2(1), 2014.

[3] W Zong, T Heldt, GB Moody, and RG Mark. An open-source algorithm to detect onset of arterial blood pressure pulses. In *Comput Cardiol, 2003*, pages 259–262. IEEE, 2003.

[4] Thomas G Pickering, John E Hall, Lawrence J Appel, Bonita E Falkner, John Graves, Martha N Hill, Daniel W Jones, Theodore Kurtz, Sheldon G Sheps, and Edward J Roccella. Recommendations for blood pressure measurement in humans and experimental animals part 1: blood pressure measurement in humans: a statement for professionals from the subcommittee of professional and public education of the american heart association council on high blood pressure research. *J Hypertens*, 45(1):142–161, 2005.

[5] Mohamad Forouzanfar, Hilmi R Dajani, Voicu Z Groza, Miodrag Bolic, Sreeraman Rajan, and Izmail Batkin. Oscillometric blood pressure estimation: past, present, and future. *IEEE Rev Biomed Eng*, 8:44–63, 2015.

[6] Dorothee Perloff, Carlene Grim, John Flack, Edward D Frohlich, Martha Hill, Mary McDonald, and Bruce Z Morgenstern. Human blood pressure determination by sphygmomanometry. *Circulation*, 88(5):2460–2470, 1993.

[7] Enrico Agabiti-Rosei, Giuseppe Mancia, Michael F OâĂŹRourke, Mary J Roman, Michel E Safar, Harold Smulyan, Ji-Guang Wang, Ian B Wilkinson, Bryan Williams, and Charalambos Vlachopoulos. Central blood pressure measurements and antihypertensive therapy. *Hypertension*, 50(1):154–160, 2007.

[8] Carmel M McEniery, John R Cockcroft, Mary J Roman, Stanley S Franklin, and Ian B Wilkinson. Central blood pressure: current evidence and clinical importance. *Eur Heart J*, 35(26):1719–1725, 2014.

[9] Edwin J Kroeker and Earl H Wood. Comparison of simultaneously recorded central and peripheral arterial pressure pulses during rest, exercise and tilted position in man. *Circ Res*, 3(6):623–632, 1955.

[10] S Hansen and M Staber. Oscillometric blood pressure measurement used for calibration of the arterial tonometry method contributes significantly to error. *Eur J Anaesthesiol*, 23(09):781–787, 2006.

[11] Bernd V Scheer, Azriel Perel, and Ulrich J Pfeiffer. Clinical review: complications and risk factors of peripheral arterial catheters used for haemodynamic monitoring in anaesthesia and intensive care medicine. *Crit Care*, 6(3):199, 2002.

[12] Ken Tegtmeyer, Glenn Brady, Susanna Lai, Richard Hodo, and Dana Braner. Placement of an arterial line. *N Engl J Med*, 354(15):e13, 2006.

[13] Thomas G Pickering. White coat hypertension. *Curr Opin Nephrol Hypertens*, 5(2):192–198, 1996.

[14] S Watson, RR Wenzel, C Di Matteo, B Meier, and TF Lüscher. Accuracy of a new wrist cuff oscillometric blood pressure device comparisons with intraarterial and mercury manometer measurements. *Am J Hypertens*, 11(12):1469–1474, 1998.

[15] William B White, Per Lund-Johansen, and Per Omvik. Assessment of four ambulatory blood pressure monitors and measurements by clinicians versus intraarterial blood pressure at rest and during exercise. *Am J Cardiol*, 65(1):60–66, 1990.

[16] D Mion and AMG Pierin. How accurate are sphygmomanometers? *J Hum Hypertens.*, 12(4):245–248, 1998.

[17] Yong Ma, Marinella Temprosa, Sarah Fowler, Ronald J Princas, Maria G Montez, Janet Brown-Friday, Mary L Carrion-Petersen, Tracy Whittington, Diabetes Prevention Program Research Group, et al. Evaluating the accuracy of an aneroid sphygmomanometer in a clinical trial setting. *Am J Hypertens*, 22(3):263, 2009.

[18] GS Stergiou, N Karpettas, A Kollias, A Destounis, and D Tzamouranis. A perfect replacement for the mercury sphygmomanometer: the case of the hybrid blood pressure monitor. *J Hum Hypertens.*, 26(4):220–227, 2012.

[19] George S Stergiou, Periklis P Giovas, Charilaos P Gkinos, and Dimitris G Tzamouranis. Validation of the a&d um-101 professional hybrid device for office blood pressure measurement according to the international protocol. *Blood Press Monit*, 13(1):37–42, 2008.

[20] A Benmira, A Perez-Martin, I Schuster, I Aichoun, S Coudray, F Bereksi-Reguig, and M Dauzat. From korotkoff and marey to automatic non-invasive oscillometric blood pressure measurement: does easiness come with reliability? *Expert Rev Med Devices*, 13(2):179–189, 2016.

[21] Andreas Bur, Michael M Hirschl, Harald Herkner, Elisabeth Oschatz, Julia Kofler, Christian Woisetschläger, and Anton N Laggner. Accuracy of oscillometric blood pressure measurement according to the relation between cuff size and upper-arm circumference in critically ill patients. *Crit Care Med*, 28(2):371–376, 2000.

[22] Jefferson M Sesler, Wendy P Munroe, and James M McKenney. Clinical evaluation of a finger oscillometric blood pressure device. *Ann. Pharmacother.*, 25(12):1310–1314, 1991.

[23] Matthew R Nelson, Jan Stepanek, Michael Cevette, Michael Covalciuc, R Todd Hurst, and A Jamil Tajik. Noninvasive measurement of central vascular pressures with arterial tonometry: clinical revival of the pulse pressure waveform? In *Mayo Clin Proc*, volume 85, pages 460–472. Elsevier, 2010.

[24] Koen Matthys and Pascal Verdonck. Development and modelling of arterial applanation tonometry: a review. *Technol Health Care*, 10(1):65–76, 2002.

[25] BM Weiss, DR Spahn, H Rahmig, R Rohling, and T Pasch. Radial artery tonometry: moderately accurate but unpredictable technique of continuous non-invasive arterial pressure measurement. *Br J Anaesth.*, 76(3):405–411, 1996.

[26] Gary M Drzewiecki, Julius Melbin, and Abraham Noordergraaf. Arterial tonometry: review and analysis. *J Biomech*, 16(2):141–152, 1983.

[27] Rohan Samria, Ridhi Jain, Ankita Jha, Sandeep Saini, and Shubhajit Roy Chowdhury. Noninvasive cuff'less estimation of blood pressure using photoplethysmography without electrocardiograph measurement. In *Region 10 Symposium, 2014 IEEE*, pages 254–257. IEEE, 2014.

[28] XF Teng and YT Zhang. Continuous and noninvasive estimation of arterial blood pressure using a photoplethysmographic approach. In *IEEE Eng Med Biol, 2003. Proc. 25th Annual Int Conf of the IEEE*, volume 4, pages 3153–3156. IEEE, 2003.

[29] J. SolÃă, M. ProenÃğa, F. Braun, E. MuntanÃľ-Calvo, C. Verjus, M. Lemay, M. Bertschi, P. Schoettker, and J. Krauss. Cuffless blood pressure monitoring: Experimental evidences of a beat-to-beat ppg technique. In *IEEE Eng Med Biol, 2016 Int Conf of the IEEE*. IEEE, 2016.

[30] Mohamad Kachuee, Mohammad Mahdi Kiani, Hoda Mohammadzade, and Mahdi Shabany. Cuff-less high-accuracy calibration-free blood pressure estimation using pulse transit time. In *2015 IEEE Int Symp Circuits Syst (ISCAS)*, pages 1006–1009. IEEE, 2015.

[31] Heiko Gesche, Detlef Grosskurth, Gert Küchler, and Andreas Patzak. Continuous blood pressure measurement by using the pulse transit time: comparison to a cuff-based method. *Eur J Appl Physiol*, 112(1):309–315, 2012.

[32] Parry Fung, Guy Dumont, Craig Ries, Chris Mott, and Mark Ansermino. Continuous noninvasive blood pressure measurement by pulse transit time. In *IEEE Eng Med Biol, 2004. IEMBS'04. 26th Annual Int Conf of the IEEE*, volume 1, pages 738–741. IEEE, 2004.

[33] Devin B McCombie, Andrew T Reisner, and H Harry Asada. Adaptive blood pressure estimation from wearable ppg sensors using peripheral artery pulse wave velocity measurements and multi-channel blind identification of local arterial dynamics. In *IEEE Eng Med Biol, 2006. EMBS'06. 28th Annual Int Conf of the IEEE*, pages 3521–3524. IEEE, 2006.

[34] Lysander WJ Bogert and Johannes J van Lieshout. Non-invasive pulsatile arterial pressure and stroke volume changes from the human finger. *Exp Physiol*, 90(4):437–446, 2005.

[35] J Penaz et al. Photoelectric measurement of blood pressure, volume and flow in the finger. In *Digest 10th Int Conf Med Biol Eng*, volume 104. International Federation for Medical and Biological Engineering, Publishers New York, 1973.

[36] Matthew S Ganio, R Matthew Brothers, Rebekah AI Lucas, Jeffrey L Hastings, and Craig G Crandall. Validity of auscultatory and penaz blood pressure measurements during profound heat stress alone and with an orthostatic challenge. *Am J Physiol Regul Integr Comp Physiol*, 301(5):R1510–R1516, 2011.

[37] Fei Li, Ling Wang, Yubo Fan, and Deyu Li. Simulation of noninvasive blood pressure estimation using ultrasound contrast agent microbubbles. *IEEE Trans Ultrason Ferroelectr Freq Control*, 59(4):715–726, 2012.

[38] Charles Tremblay-Darveau, Ross Williams, and Peter N Burns. Measuring absolute blood pressure using microbubbles. *Ultrasound Med Biol*, 40(4):775–787, 2014.

[39] Flemming Forsberg, Ji-Bin Liu, William T Shi, Junji Furuse, Masafumi Shimizu, and Barry B Goldberg. In vivo pressure estimation using subharmonic contrast microbubble signals: proof of concept. *IEEE Trans Ultrason Ferroelectr Freq Control*, 52(4):581–583, 2005.

[40] Alessandro Crimi, Maxim Makhinya, Ulrich Baumann, Christoph Thalhammer, Gabor Szekely, and Orcun Goksel. Automatic measurement of venous pressure using b-mode ultrasound. *IEEE Trans Biomed Eng*, 2015.

[41] Elena Chung, Guo Chen, Brenton Alexander, and Maxime Cannesson. Non-invasive continuous blood pressure monitoring: a review of current applications. *Front Med*, 7(1):91–101, 2013.

[42] H Pessenhofer. Single cuff comparison of two methods for indirect measurement of arterial blood pressure: standard auscultatory method versus automatic oscillometric method. *Basic Res Cardiol*, 81:101–109, 1986.

[43] NR Campbell, Arun Chockalingam, J George Fodor, and Donald W McKay. Accurate, reproducible measurement of blood pressure. *CMAJ*, 143(1):19, 1990.

[44] Richard H Epstein, Suzanne Huffnagle, and Richard R Bartkowski. Comparative accuracies of a finger blood pressure monitor and an oscillometric blood pressure monitor. *J Clin Monit*, 7(2):161–167, 1991.

[45] Christoph Schramm, Lisa Baat, and Konstanze Plaschke. Continuous noninvasive arterial pressure: assessment in older and high-risk patients under analgesic sedation. *Blood Press Monit*, 16(6):270–276, 2011.

[46] William M Fairbank Jr and Marlan O Scully. A new noninvasive technique for cardiac pressure measurement: resonant scattering of ultrasound from bubbles. *IEEE Trans Biomed Eng*, 24(2):107–110, 1977.

[47] Gert A Van Montfrans. Oscillometric blood pressure measurement: progress and problems. *Blood Press Monit*, 6(6):287–290, 2001.

[48] Alessandro Crimi, Maxim Makhinya, Ulrich Baumann, Christoph Thalhammer, Gabor Szekely, and Orcun Goksel. Automatic measurement of venous pressure using b-mode ultrasound. *IEEE Trans Biomed Eng*, 2015.

[49] Pierre D Mourad, Michel Kliot, Rex Patterson, and Alec Rooke. Systems and methods for determining blood pressure, October 19 2010. US Patent 7,815,574.

[50] Deborah C Gordon and Frank A Brunot. Method and apparatus for continuously and noninvasively measuring the blood pressure of a patient, November 17 1992. US Patent 5,163,438.

[51] Richard G Caro and Mark H Sher. Apparatus and method for measuring an induced perturbation to determine blood pressure, January 7 1997. US Patent 5,590,649.

[52] Ted W Russell. Apparatus and method for continuous non-invasive cardiovascular monitoring, June 2 1987. US Patent 4,669,485.

[53] Luya Li, Rakesh Kumar Sethi, Ming Sun, Alexander Yuk Sit, and Yong Liu. Continuous non-invasive blood pressure measurement apparatus and methods providing automatic recalibration, November 25 2008. US Patent 7,455,643.

[54] E O'Brien, R Asmar, L Beilin, Y Imai, JM Mallion, G Mancia, T Mengden, M Myers, P Padfield, P Palatini, et al. European society of hypertension working group on blood pressure monitoring european society of hypertension recommendations for conventional, ambulatory and home blood pressure measurement. *J Hypertens*, 21(821):48, 2003.

[55] Association for the Advancement of Medical Instrumentation et al. Non-invasive sphygmomanometers–part 2: clinical investigation of automated measurement type ansi/aami. Technical report, ISO 81060-2/ANSI-AAMI, 2013.

[56] Eoin O'brien, James Petrie, William Littler, Michael de Swiet, Paul L Padfield, Kevin O'malley, Michael Jamieson, Douglas Altman, Martin Bland, and Neil Atkins. The british hypertension society protocol for the evaluation of automated and semi-automated blood pressure measuring devices with special reference to ambulatory systems. *J Hypertens*, 8(7):607–619, 1990.

[57] KJ Parker, MM Doyley, and DJ Rubens. Imaging the elastic properties of tissue: the 20 year perspective. *Phys Med Biol*, 56(1):R1, 2011.

[58] A.M. Zakrzewski, SY Sun, MW Gilbertson, B Vannah, L Chai, J Ramos, and BW Anthony. Multi-scale compression-based quantitative elastography and its application to blood pressure estimation. In *International Tissue Elasticity Conference*, 2012.

[59] Aaron M Zakrzewski and Brian W Anthony. Quantitative elastography and its application to blood pressure estimation: Theoretical and experimental results. In *IEEE Eng Med Biol, 2013 Int Conf of the IEEE*, pages 1136–1139. IEEE, 2013.

[60] Aaron Michael Zakrzewski. Multi-scale quantitative elastography and its application to blood pressure estimation. Master's thesis, Massachusetts Institute of Technology, 2013.

[61] George Howard, A Richey Sharrett, Gerardo Heiss, Gregory W Evans, Lloyd E Chambless, Ward A Riley, and Gregory L Burke. Carotid artery intimal-medial thickness distribution in general populations as evaluated by b-mode ultrasound. aric investigators. *Stroke*, 24(9):1297–1304, 1993.

[62] Joachim O Arndt, Jürgen Klauske, and Frank Mersch. The diameter of the intact carotid artery in man and its change with pulse pressure. *Pflugers Arch.*, 301(3):230–240, 1968.

[63] Jonathan Ophir, S Kaisar Alam, Brian S Garra, Faouzi Kallel, Elisa E Konofagou, Thomas Krouskop, Christopher RB Merritt, Raffaella Righetti, Remi Souchon, Seshadri Srinivasan, et al. Elastography: imaging the elastic properties of soft tissues with ultrasound. *J Med Ultrason*, 29(4):155–171, 2002.

[64] Daniel Balzani, Simone Deparis, Simon Fausten, Davide Forti, Alexander Heinlein, Axel Klawonn, Alfio Quarteroni, Oliver Rheinbach, and Joerg Schröder. Numerical modeling of fluid–structure interaction in arteries with anisotropic polyconvex hyperelastic and anisotropic viscoelastic material models at finite strains. *Int J Numer Method Biomed Eng*, 2015.

[65] Kang Kim, WF Weitzel, JM Rubin, Hua Xie, Xunchang Chen, and M O'Donnell. Vascular intramural strain imaging using arterial pressure equalization. *Ultrasound Med Biol*, 30(6):761–771, 2004.

[66] Klaus-Jürgen Bathe. *Finite element procedures.* Klaus-Jurgen Bathe, 2006.

[67] Bruce R Simon, Albert S Kobayashi, D Eugene Strandness, and Curt A Wiederhielm. Reevaluation of arterial constitutive relations: A finite-deformation approach. *Circ Res*, 30(4):491–500, 1972.

[68] Donald T Reilly, Albert H Burstein, and Victor H Frankel. The elastic modulus for bone. *J Biomech*, 7(3):271IN9273–272IN12275, 1974.

[69] Athena Huang. May the force be with you: A medical ultrasound system with integrated force measurement. Master's thesis, Massachusetts Institute of Technology, 2017.

[70] Julian Guerrero, Septimiu E Salcudean, James A McEwen, Bassam A Masri, and Savvas Nicolaou. Real-time vessel segmentation and tracking for ultrasound imaging applications. *IEEE Trans Med Imaging*, 26(8):1079–1090, 2007.

[71] Jason M Nash, John N Carter, and Mark S Nixon. The velocity hough transform: a new technique for dynamic feature extraction. In *Image Process, 1997. Proc Int Conf on*, volume 2, pages 386–389. IEEE, 1997.

[72] Purang Abolmaesumi, Septimiu E Salcudean, Wen-Hong Zhu, Mohammad Reza Sirouspour, and Simon Peter DiMaio. Image-guided control of a robot for medical ultrasound. *IEEE Trans Robot Autom*, 18(1):11–23, 2002.

[73] Purang Abolmaesumi, Mohammad Reza Sirouspour, and SE Salcudean. Real-time extraction of carotid artery contours from ultrasound images. In *Proc IEEE Int Symp Biomed Imaging: Macro to Nano*, pages 181–186. IEEE, 2000.

[74] Fei Mao, Jeremy Gill, Donal Downey, and Aaron Fenster. Segmentation of carotid artery in ultrasound images: Method development and evaluation technique. *Med Phys*, 27(8):1961–1970, 2000.

[75] Chaoquan Chen, Tamie L Poepping, Jason J Beech-Brandt, Steven J Hammer, Richard Baldock, Bill Hill, Paul Allan, William J Easson, and Peter R Hoskins. Segmentation of arterial geometry from ultrasound images using balloon models. In *Biomed Imaging: Nano to Macro, 2004. IEEE Int Symp on*, pages 1319–1322. IEEE, 2004.

[76] William K Pratt. *Introduction to digital image processing*. CRC Press, 2013.

[77] Noah Friedland and Dan Adam. Automatic ventricular cavity boundary detection from sequential ultrasound images using simulated annealing. *IEEE Trans Med Imaging*, 8(4):344–353, 1989.

[78] Yaakov Bar-Shalom, Thomas E Fortmann, and Peter G Cable. *Tracking and data association*, volume 87. Acoustical Society of America, 1990.

[79] ML Raghavan, Baoshun Ma, and Mark F Fillinger. Non-invasive determination of zero-pressure geometry of arterial aneurysms. *Ann Biomed Eng*, 34(9):1414–1419, 2006.

[80] Jia Lu, Xianlian Zhou, and Madhavan L Raghavan. Inverse elastostatic stress analysis in pre-deformed biological structures: demonstration using abdominal aortic aneurysms. *J Biomech*, 40(3):693–696, 2007.

[81] Michael I Miga. A new approach to elastography using mutual information and finite elements. *Phys Med Biol*, 48(4):467, 2003.

[82] Michael Lampton. Damping–undamping strategies for the levenberg–marquardt nonlinear least-squares method. *Comput Phys*, 11(1):110–115, 1997.

[83] Manolis IA Lourakis. A brief description of the levenberg-marquardt algorithm implemented by levmar. *Foundation of Research and Technology*, 4(1), 2005.

[84] Ron Kohavi et al. A study of cross-validation and bootstrap for accuracy estimation and model selection. In *Ijcai*, volume 14, pages 1137–1145. Stanford, CA, 1995.

[85] MATLAB. *version 8.5.0.197613 (R2015a).* The MathWorks Inc., Natick, Massachusetts, 2015.

[86] Matthew Wright Gilbertson. Handheld force-controlled ultrasound probe. Master's thesis, Massachusetts Institute of Technology, 2010.

[87] Matthew W Gilbertson and Brian W Anthony. Ergonomic control strategies for a handheld force-controlled ultrasound probe. In *Intelligent Robots and Systems (IROS), 2012 IEEE/RSJ Int Conf on*, pages 1284–1291. IEEE, 2012.

[88] Matthew W Gilbertson and Brian W Anthony. Impedance-controlled ultrasound probe. In *SPIE Medical Imaging*, pages 796816–796816. International Society for Optics and Photonics, 2011.

[89] John Ludbrook. Statistical techniques for comparing measurers and methods of measurement: a critical review. *Clin Exp Pharmacol Physiol*, 29(7):527–536, 2002.

[90] MM Mukaka. A guide to appropriate use of correlation coefficient in medical research. *Malawi Medical Journal*, 24(3):69–71, 2012.

[91] James O Westgard and Marian R Hunt. Use and interpretation of common statistical tests in method-comparison studies. *Clin Chem*, 19(1):49–57, 1973.

[92] Emmanouil Karatzis, Theodore G Papaioannou, Konstantinos Aznaouridis, Kalliopi Karatzi, Kimon Stamatelopoulos, Antonios Zampelas, Christos Papamichael, John Lekakis, and Myron Mavrikakis. Acute effects of caffeine on blood pressure and wave reflections in healthy subjects: should we consider monitoring central blood pressure? *Int J Cardiol*, 98(3):425–430, 2005.

[93] Péter Studinger, Zsuzsanna Lénárd, Zsuzsanna Kováts, László Kocsis, and Mark Kollai. Static and dynamic changes in carotid artery diameter in humans during and after strenuous exercise. *J Physiol*, 550(2):575–583, 2003.

[94] Shahzad Mahmood Munir, Benyu Jiang, Antoine Guilcher, Sally Brett, Simon Redwood, Michael S Marber, and Phil Chowienczyk. Exercise reduces arterial pressure augmentation through vasodilation of muscular arteries in man. *Am J Physiol Heart Circ Physiol*, 294:H1645–H1650, 2008.